

Function of the Osteocyte Lacunocanalicular Network in Bone Mechanoresponsiveness

DISSERTATION

**zur Erlangung des akademischen Grades
doctor rerum naturalium (Dr. rer. nat.)
im Fach Physik**

**Spezialisierung: Theoretische Physik
eingereicht an der**

**Mathematisch-Naturwissenschaftlichen Fakultät I
der Humboldt-Universität zu Berlin**

von Herrn Alexander Franciscus van Tol

Präsident der Humboldt-Universität zu Berlin:
Prof. Dr.-Ing. Dr. Sabine Kunst

Gutachter:

1. Prof. Dr. Igor Sokolov
2. Prof. Dr. Dr.h.c. Peter Fratzl
3. Dr Enrico Dall'Ara

Tag der Verteidigung: 03.11.2020

KURZFASSUNG

Knochen ist ein lebendes Material, das seine Struktur an die mechanische Umgebung anpasst. Zur strukturellen Anpassung muss der Knochen die mechanische Belastung erfassen. Allerdings sind Knochen mechanisch so steif, dass die lokalen Verformungen zu klein sind um von den Knochenzellen direkt detektiert zu werden. Osteozyten sind Knochenzellen, die ein Zellnetzwerk in der mineralisierten Matrix bilden. Ihre Zellkörper sind in Lakunen untergebracht und ihre Zellprozesse in engen Kanälchen, den Canaliculi. Die Hypothese des Flüssigkeitsflusses besagt, dass der lastinduzierte Flüssigkeitsfluss durch dieses Lakunen-Canaliculi-Netzwerk (LCN) einen Verstärkungsmechanismus bereitstellt, der es den Osteozyten ermöglicht, die dynamische Belastung des Knochens zu erfassen. Wir stellen die Hypothese auf, dass die Architektur des LCN eine wesentliche Rolle in Bezug auf die Mechanosensitivität spielt, da sie den Flüssigkeitsfluss beeinflusst. Das zentrale Ziel dieser Arbeit ist es, diese Hypothese an realen LCN-Architekturen mit einem Modell des lastinduzierten Flüssigkeitsflusses zu testen und den resultierenden Fluss mit der Mechanoreaktion des Knochens zu vergleichen. Wir haben das LCN mithilfe konfokaler Laser-Scanning-Mikroskopie untersucht. Wir haben dann die auf den Kirchhoffschen Gesetzen basierende Schaltungstheorie verwendet, um die Geschwindigkeiten der Flüssigkeit in allen abgebildeten Canaliculi zu modellieren und darzustellen wie sich die verdrängte Flüssigkeit über das LCN verteilen würde. Basierend auf diesen Geschwindigkeiten wurde die Mechanoreaktion des Knochens vorhergesagt. In meiner Studie wurden die Knochen von Mäusen verwendet, wodurch kontrollierte *in vivo* Belastungsexperimente und die Messung der Mechanoreaktion in Bezug auf gebildeten bzw. resorbierten Knochen unter Verwendung von *in vivo* μ CT möglich waren. Die Flüssigkeitsströmungsmuster durch das LCN korrelierten mit der gemessenen Mechanoreaktion. Das heißt, Knochenbildung wurde in Bereichen nahe höherem Fluss beobachtet, während Knochenabbau in Bereichen nahe geringem Fluss beobachtet wurde. Die Vorhersage der Mechanoreaktion unter Berücksichtigung der Architektur des LCN war quantitativ besser als eine Vorhersage, die nur auf mechanischer Belastung basiert. Qualitativ haben wir festgestellt, dass Gefäßkanäle im Kortex als lokale Senken des Flüssigkeitsflusses fungieren und daher den Fluss an der nahegelegenen Knochenoberfläche reduzieren. Im Gegensatz dazu nahmen die Strömungsgeschwindigkeiten für konvergente Netzwerkstrukturen zu, bei denen die Zahl der Kanäle zur Knochenoberfläche hin abnimmt. In einem zweiten Projekt konzentrierten wir uns auf gesunden, menschlichen osteonalen Knochen. Osteone sind zylindrische Strukturen um Gefäßkanäle, die praktisch vom umgebenden Knochen abgeschottet sind. Wir analysierten acht gewöhnliche Osteone mit einem nahezu homogenen LCN und neun Osteon-in-Osteonen, die durch eine ringartige Zone mit geringer Netzwerkkonnektivität zwischen dem inneren und dem äußeren Teil dieser Osteone gekennzeichnet sind. In Canaliculi, die die beiden Teile des Osteons in Osteonen überbrücken, wurde ein wesentlich höherer lastinduzierter Flüssigkeitsfluss beobachtet als in anderen Canaliculi. Dies führte dazu, dass der durchschnittliche Fluss 2,3-mal höher war als bei normalen Osteonen. Es ist daher wahrscheinlich, dass Osteon-in-Osteon-Konstruktionen besonders zur Mechanosensitivität des kortikalen Knochens beitragen. Die Untersuchungen in dieser Doktorarbeit legen nahe, dass die LCN-Architektur neben der mechanischen Belastung als Schlüsselfaktor für die Knochenanpassung dient.

Knochen, Mechanoreaktion, Flüssigkeitsfluss, Lakunen-Canaliculi-Netzwerk, Osteozyten

ABSTRACT

Bone is a living material, which adapts its structure in response to the mechanical environment. For structural adaptation bone need to sense the mechanical loading. However, bone is so stiff that the local strains are too small to be directly sensed by bone cells. Osteocytes are bone cells that form a cell network located within the mineralized matrix. Their cell bodies are housed in lacunae and their cell processes in narrow canals, the canaliculi. According to the fluid flow hypothesis, load induced fluid flow through this lacunocanalicular network (LCN) provides an amplification mechanism which allows osteocytes to sense dynamic loading of the bone. We hypothesize that the network architecture of the LCN plays an essential role in bone's mechanosensitivity, as it influences the fluid flow. We aimed to test these hypotheses by using real LCN architectures in a model of load induced fluid flow, and compare the resulting flow with the mechanoreponse of bone. We imaged the LCN using confocal laser scanning microscopy (CLSM). Image processing was then used to describe the LCN as a mathematical network consisting of edges and nodes, representing the canaliculi and their connections respectively. We then employed circuit theory, based on Kirchhoff's laws, to model the velocities of the fluid in all the imaged canaliculi. Based on these velocities, the mechanoreponse of bone was predicted. Mice were used in my study, as this allowed a controlled *in vivo* loading and a measurement of the mechanoreponse in terms of formed/resorbed bone using *in vivo* μ CT. Fluid flow patterns through the LCN of mice correlated with the measured mechanoreponse, i.e., bone formation was observed near surfaces of higher flow, while resorption was observed near surfaces with low flow. The prediction of the mechanoreponse considering the architecture of the LCN was quantitatively better than a prediction based on strains only. Qualitatively, we identified that vascular canals in the cortex act as local sinks of fluid flow and, therefore, reduce the flow at the nearby bone surface. In contrast, flow velocities increased in convergent network structures, where the flow is channeled into fewer canaliculi nearby the surface. In a second project we focused on healthy human osteonal bone. Osteons are cylindrical structures around vascular canals, which are practically sealed off from the surrounding bone. We analyzed 8 ordinary osteons with a rather homogeneous LCN, and 9 osteon-in-osteons, which are characterized by a ring-like zone of low network connectivity between the inner and the outer parts of these osteons. A substantially higher load-induced fluid flow was observed in canaliculi that bridge the two parts of the osteon-in-osteons. This resulted in an average flow, which was 2.3 times higher compared to ordinary osteons. It is therefore likely that osteon-in-osteons particularly contribute to the mechanosensitivity of cortical bone. Based on both studies in this PhD thesis we conclude that LCN architecture should be considered as a key determinant of bone adaptation besides mechanical loading.

Bone, mechanoreponse, fluid flow, lacunocanalicular network, osteocytes

CONTENTS

Kurzfassung	3
Abstract	5
Contents	7
Motivation	1
Why do Physicists Study Mechanobiology?	1
1. Introduction	5
1.1 The Hierarchical Porosity in Cortical Bone	9
1.2 Multifunctionality of the Osteocyte Network	12
1.3 Load-Induced Fluid Flow in Bone	14
1.3.1 Models of Fluid Flow in Bone – What Questions Can Be Asked?	15
1.3.2 Strain and Fluid Flow Patterns at the Organ Level	15
1.3.3. Two Pore Networks – The LCN and Vascular Porosity	18
1.3.4. Fluid Flow in Human Osteons	21
1.3.5. Fluid Flow and the Ultrastructure of Lacunae and Canaliculi	24
2. Methods – Multiscale Characterization of Bone	29
2.1. <i>In vivo</i> Loading Combined with 3D Morphometry of the Mechanoresponse	29
2.2 Finite Element Modeling	30
2.3. Sample Preparation and Rhodamine Staining	31
2.4. Confocal Laser Scanning Microscopy	33
3. Model Development – Mechanosensing via Load-Induced Fluid Flow	37
3.1 Fluid Flow in Single Canaliculi	37
3.2 Fluid Flow Through Networks	39
3.3. Boundary Conditions in the Network Model	42

3.4. Prediction of the Bone Mechanoresponse	44
4. Results and Discussion	47
4.1. Results of the Mouse Tibia Study.....	47
4.1.1. The Measured Mechanoresponse of Mouse Tibiae.....	47
4.1.2. Structural Heterogeneity of the Pore Networks in Mouse Tibiae	49
4.1.3. Fluid Flow Induced by Controlled Loading of the Tibiae.....	51
4.1.4. Prediction Local Bone Mechanoresponses	53
4.1.5. Discussion of the Mouse Tibia Study.....	55
4.2. Results of the Human Osteonal Bone Study.....	61
4.2.1. The LCN Architecture of Human Osteonal Bone	61
4.2.2. Load Induced Fluid Flow in Human Osteons	64
4.2.3. Fluid Pressure in Human Osteons	67
4.2.4. Discussion of the Human Osteonal Bone Study	69
5. Conclusion and Outlook	75
5.1. Additional Projects During my PhD Time.....	80
6. References.....	83
7. Dedication.....	94
8. Acknowledgements	95
9. Selbstständigkeitserklärung	96

MOTIVATION

Why do Physicists Study Mechanobiology?

Bone is commonly known as a hard and dense skeletal connective tissue, which protects our vital organs, it provides us with posture and allows movement. The cortex of bones is rather dense, while the inside of most bones is porous or sponge-like. However, bone is not just a solid piece of a lifeless material, but it is a living organ that has a complex hierarchical structure, which can adapt and repair itself, and is a composite material at the nano-scale, where 50% of the volume of the cortex is actually organic material. This structure and composition give bones not only exceptional mechanical properties for its weight (i.e. hardness, elasticity, durability), but mechano-responsive cells in bone make it an active smart material that can self-repair and can adapt to changes in the mechanical environment (Fratzl and Weinkamer 2007). Linked porosity networks in cortical bone at multiple length scales, play a role in this adaptation process. A certain type of bone cells (osteocytes) live embedded in the bone matrix, in a vast complex network of lacunae and canaliculi, and are surrounded by a thin layer of fluid and organic matrix. This places bone mechanobiology right at the interface of biology and physics. It is intriguing how pure mechanical loads applied to our bones somehow travel through many length scales, to finally end up as a biochemical signal, which orchestrate the behavior of our cells (Fig. 1).

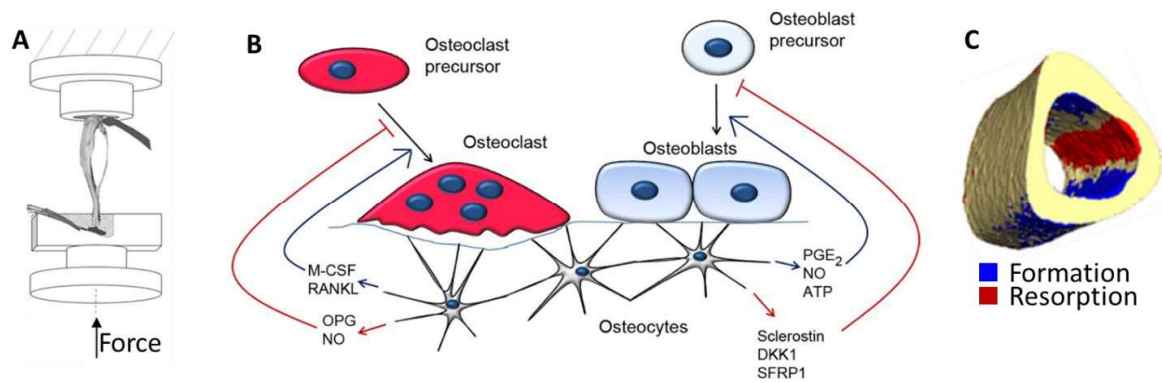


Fig. 1. A) A controlled loading experiment is an example of a changing mechanical environment, which is routinely used to study the mechanoreponse of long bones (e.g., tibiae) in living mice to an applied known force. B) The changes in mechanical load are indirectly sensed by the osteocytes, which signal the osteoclasts (bone resorbing cells) and the osteoblasts (bone forming cells) as illustrated in this schematic from Dallas, Prideaux et al. (2013). Due to vast amount of molecular biology and biochemical research, we understand most of the signaling pathways involved in the mechanoreponse of bone in both healthy and pathological conditions. Note that the diagram in (B) only shows a small fraction of what is known. C) Finally the mechanical stimulation (as illustrated in A) leads to adaptations of the bone by resorbing bone which is not needed and forming extra bone where needed. However, there are two open questions: 1) How are changes in the loading of the bone translated to local signals, which can be sensed by the bone cells? The mechanical strain is likely an order of magnitude too small to be directly sensed by bone cells, and therefore we expect strain amplification mechanisms between whole bone strain and strain at the cell level. 2) How are biochemical signals transported from the cells embedded in the bone, to the surface in order to

orchestrate bone formation and resorption? Note that small signaling molecules are very reactive, and that large molecules cannot easily travel through the narrow spaces in the bone matrix, which constrains the time and space where these molecules have an effect. We believe that the network architecture of the osteocyte network should be taken into account to answer both of these questions.

According to the fluid flow hypothesis, cyclic loading of the bone leads to fluid flow within the canaliculi, which can be sensed by molecules in the cell processes of the osteocytes. After the biological sensors notice changes in the mechanical environment, the biochemical processes in these cells perform signal processing to decide how the bone should be adapted or repaired. Then, the biological signals need to be somehow transported to the surfaces of our bones, in order to recruit the cells that do the formation and resorption work (Sims and Vrahnas 2014, Klein-Nulend and Bonewald 2020), while building materials need to be transported through the ‘solid’ cortical bone. The biochemical signals from the osteocytes to the cells at the bone surface also need to be transported via the canalicular network. Therefore, in my PhD study I investigated the architecture of the osteocyte lacunocanalicular network and, based on the fluid flow hypothesis, how this network could act as a distributed mechanical sensor network with built in amplification and signal processing capabilities.

The research strategy of this thesis work includes healthy adult mouse bones, which were pre-characterized by our collaboration partners. Mouse models are a powerful tool to study the mechanobiology of bone, due to the small size of the animals, which allows *in vivo* imaging of the microstructural changes in their bones as a result of controlled loading. Additionally their genetic background has been thoroughly characterized, which is important for a healthy skeleton (Verbruggen 2018).

Fully understanding the physics of the mechanical environment at the microarchitectural scale of healthy bone is equally important as understanding the molecular mechanisms (Teoh, Goh et al. 2019). A better understanding could contribute to the unanswered questions in the basic bone field, for example, why different bones react differently to applied mechanical loads. It could also help to answer clinical questions, such as if mechanotransduction plays a role in poorly healing fractures (McKibbin 1978, Xie, Zhang et al. 2019). A specific example of a study that would benefit from this thesis is a mouse model of premature aging (gerodermia osteodysplastica), which our collaborators together with us are currently investigating. In contrast to healthy mice, these mice do not adapt their bones when high loads are applied. It was observed that these mice have an abnormal osteocyte lacunocanalicular network (LCN) architecture. This raises the question if the LCN architecture plays a key role in this disease.

In this thesis, I combined experimental work, imaging of real lacunocanalicular networks, with computational work, modelling of the fluid flow through these networks. The mathematical model allows us to investigate the role of the LCN in the translation of the controlled loading to the

mechanoreponse in these mice. Several mathematical models of fluid flow and pressure have supported the fluid flow hypothesis (Cardoso, Fritton et al. 2013). However, currently in the literature investigations into the LCN architecture are limited (Hemmatian, Bakker et al. 2017). Consequently, the role of the network architecture in mechanosensing remains unclear, thus leaving a substantial gap in the line of argumentation in bone mechanobiology (Fig. 1). Due to missing information about the actual network architecture, several studies assumed a homogeneous and simplified LCN architecture. Only since very recently, the lacunocanalicular network of bone can be imaged in macroscopic bone volumes. This is essential when one wants to link the structural changes at the millimeter scale to the full network architecture with components at the sub micrometer scale. This is exactly in the range of full cross sections of human osteons. Osteons are fundamental structural units of bone, which are a few hundred micrometer in diameter. Also full cross sections of mouse tibiae, which have a diameter in the order of a millimeter, can now be imaged. With these recent developments, we aim to test the hypothesis that small strains in the rather stiff bone induce fluid displacements, which are physically amplified and processed while being forced through the architecture of this network (i.e. the fluid flow hypothesis). To test this we combine the following methods:

1. Controlled *in vivo* loading of mouse tibiae to induce a mechanoreponse in these bones,
2. Time-lapse *in vivo* microCT to follow the mechanoreponse (i.e. formation/resorption of bone) over time,
3. Laser scanning confocal microscopy (CLSM) of human and mouse bones to image different lacunocanalicular network architectures,
4. A model of load-induced fluid flow through the canaliculi of the measured networks, based on circuit theories and local strains in the bone.

This thesis is structured as follows: Chapter 1 introduces the structure of bone, from the macrostructure of the whole bone down to the ultrastructure of the lacunocanalicular network. This chapter also introduces models of fluid flow from the tissue level down to flow profiles inside single canaliculi. Chapter 1 closes with a detailed explanation of the research strategy of the thesis' projects. Chapter 2 will cover the experimental methods (methods 1 to 3 from the list above) used for the research in this thesis. Chapter 3 describes the theoretical part of this study (method 4), including model development and predictions of mechanosensitivity. In chapter 4.1 I first present the study on the mouse tibiae, since the actual remodeling history was measured in these bones. Chapter 4.2 follows with the investigation on human bone, where due to technical limitations and ethical constraints we do not know the remodeling history. In the human osteons we found striking differences between fluid flow patterns in different types of osteons. Based on the mouse model we can predict how these fluid flow patterns contribute to strong differences in the mechanosensitivity of different human osteons. Chapter 5 presents conclusions, before the thesis ends with an outlook on future research.

1. INTRODUCTION

In the 19th century Julius Wolff and Wilhelm Roux observed that bone has a hierarchical structure, which adapt its shape to meet its mechanical demands (i.e. mechanical protection, load bearing or locomotion) (Willie, Duda et al. 2013). From this observation, they concluded that mechanical forces are key factors in the morphogenic development of bones. The internal structures of bones are optimal to distribute the external stresses that bones are facing most commonly, in a similar way as the light weight truss constructions which are commonly used in, for example, bridges and ceilings (Fig. 1.1 A, B). In a cross section of a long bone like a femur (Fig. 1.1 C) two different types of bone can be distinguished: dense cortical bone and porous trabecular bone. Trabecular bone contains a network of bone beams and plates (trabeculae). The trabeculae are in the order of 100 μm thick, while the pore size can vary from hundreds of micrometers to several millimeters (Fig. 1.1 D). Most trabecular bone is near surfaces where the bone is loaded, such as joints and muscle attachments. The mid shaft of long bones, such as the femur, have very little trabecular bone. Instead, the mid shaft of long bones has a thick cortex (up to several centimeters) (Fig. 1.1 C, E), which offers resistance to bending and buckling. This lightweight truss design is comparable to that of the Glienicker Brücke (Fig. 1.1 A) and the Hall of Knights (Fig. 1.1 B), for example. The orientations of the beams in these constructions follow the direction of the most common stresses, and concentrate the stress to the heavy solid pillars and walls. The head of the hip bone is loaded from several directions. The trabecular bone reflects the direction of the stresses and transfer this load to the dense cortical bone of the femur (Fig. 1.1 C).

When we zoom in to the next hierarchical level of bone, we see that at a nanoscopic length scale bone is a composite material, consisting of mineral particles embedded in a fibrous collagen-rich organic matrix. The mineral in both cortical and trabecular bone is carbonated hydroxyapatite, which can be observed by transmission electron microscopy due to its high electron density (Fig. 1.1 E). It has been shown that the long axis of the hydroxyapatite crystals is strongly aligned with the preferred orientation of the collagen fibers (Fratzl, Gupta et al. 2004) to form a strong nanocomposite material which is somewhat comparable to concrete with rebar (Fig. 1.1. F, G) (Jager and Fratzl 2000, Fratzl, Gupta et al. 2004). Fig. 1.1. F shows that the mineralized collagen fibers are arranged in lamellae with spatial changes in the preferred orientation referred to as “twisted plywood structure”. However, bone is not always lamellar. During morphogenesis of bones and fracture healing, new bone is rapidly formed. This rapidly formed so-called woven bone is not as organized as lamellar bone, but shows randomly oriented collagen weaves (Shapiro and Wu 2019). In many vertebrates, this scaffold of woven bone is later removed or replaced with lamellar bone by the remodeling process. Additionally bone is deposited layer by layer on the surfaces of cortical bone, forming a lamellar-like bone on top of the woven bone with a dense, well-ordered canalicular network and regularly shaped osteocyte lacunae (Kerschnitzki, Wagermaier et al. 2011, Ip, Toth et al. 2016).

1. Introduction

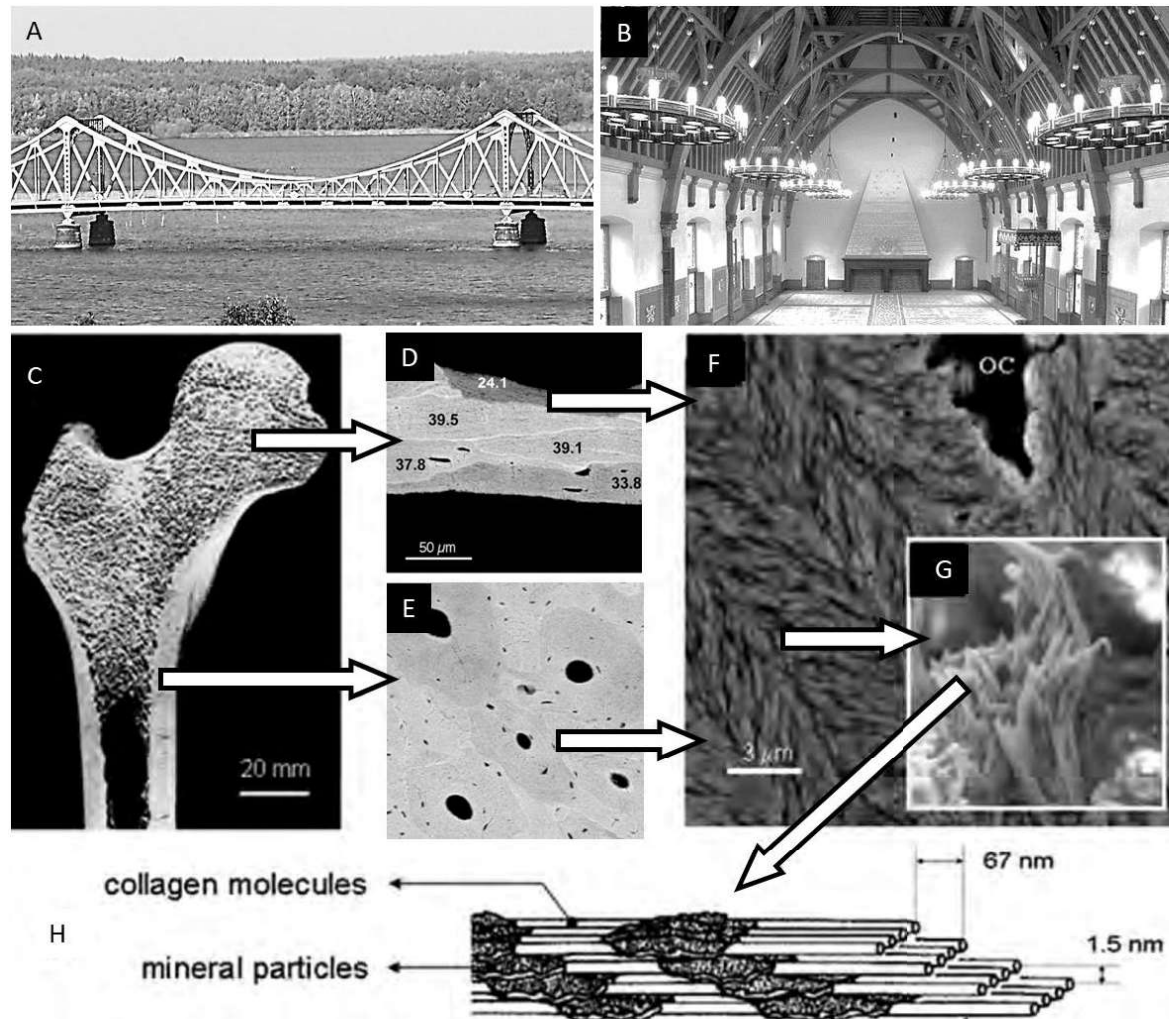


Fig. 1.1. The relationship between the hierarchical structure of bone and its function. The ‘design’ of bone follows principles which are similar to engineering. The Glienicker Brücke (A) and the Hall of Kings (B) have a lightweight truss structure to concentrate the forces in the solid pillars and walls. (C) This section through the human hip bone (femur) shows an internal porous structure (trabecular bone) in the proximal part of the femur (Fratzl, Gupta et al. 2004), which has a similar load distributing task as the truss structure of bridges (A). The structure of the trabecular bone near the mid shaft resembles the roof structure of typical medieval buildings, such as the Hall of Kings (B). The mid shaft of the femur has no internal structure, but only thick walls of cortical bone. (D) A magnification of the trabecular bone using quantitative backscattered electron imaging (qBEI) on one bone beam. Bone beams (trabeculae), which are in the order of 100 µm thick, form a lightweight bone network which distributes the loads within the bone (Fratzl, Gupta et al. 2004). The heterogeneity in degree of mineralization is clearly visible in these images as differences in intensity (white is highly mineralized). (E) A magnification of the thick cortical bone reveals that also is porous. The osteons with a diameter of a few hundred micrometer, comprising a haversian canal and its concentrically arranged lamellae, are visible as zones with different degrees of mineralization. (F) Further magnification shows that at the micron level mineral is well aligned, while orientation varies between different lamella (Fratzl and Weinkamer 2007). A fraction of the bone forming osteoblasts get trapped during formation of new bone, and these cells stay alive inside pores called lacunae (marked with OC). (G) A detailed image of a single collagen fiber bundle (Fratzl and Weinkamer 2007). The minerals are co-

aligned with collagen bundles, which are arranged in a plywood like structure in lamellar bone. H) A model of how mineral crystals in bone are aligned along the collagen molecules to form a strong composite material (Fratzl and Weinkamer 2007).

The shape and internal structure of bone are not static, as bone is a living material that can repair itself and adapt its structure. Electron microscopy images using back-scattered mode in Fig. 1.1 D, E reveal the heterogeneity in mineral content of both trabecular and cortical bone. This heterogeneity is a result of the constant remodeling of bone. Remodeling is the process which keeps our bones in good condition and resistant against fatigue by replacing old or damaged material. Osteoclasts are constantly removing older bone, which is higher mineralized, more brittle and often contains microdamage (Vaananen 1993). Osteoblasts then fill the cavities made by the osteoclasts with new unmineralized bone. This way osteoclasts and osteoblasts replace an equivalent of our full trabecular bone volume roughly every five years and our cortical bone volume roughly every ten years. During the remodeling process a fraction of the osteoblasts differentiate to osteocytes, which become embedded in the new bone (Fig. 1.2 A). Being initially unmineralized, bone is constantly incorporating mineral. As a consequence, bone with older tissue age appears brighter than newly formed bone in quantitative backscattered electron images (qBEI) (Ruffoni, Fratzl et al. 2007). Therefore, qBEI shows a history of the remodeling process, where remodeling of trabecular bone happens in patches (fig. 1.1 D), and remodeling of cortical bone creates osteons (Fig. 1.1 E, Fig. 1.2 B). Osteonal remodeling starts with the formation of a straight tube like structure, which is aligned parallel to the long axis of the bone (Fig. 1.2 B). After removal of the old bone, the lamella of the osteon are formed layer by layer (Fig 1.2. A, B).

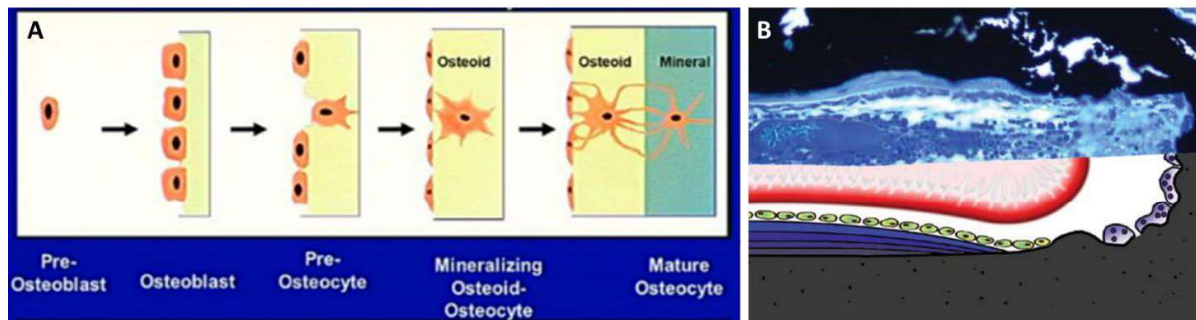


Fig. 1.2. Osteon formation. A) Schematic representation of new bone formation by osteoblasts from Bonewald (2011). The osteoblasts form unmineralized osteoid (yellow), which is an organic matrix consisting of mostly collagen. Osteoid then mineralizes to form bone. Some osteoblasts get embedded in the new bone after they differentiate to osteocytes. B) A microscopic image and an illustration of the formation of a new osteon (Robling, Castillo et al. 2006). Before osteons are formed, osteoclasts (drawn as larger purple cells) resorb the bone from left to right in the cutting cone (i.e. they resorb the leading surface of the new osteon). When resorption is completed the closing cone follows, where osteoblasts (green small cells) deposit lamellae of new bone (blue and black layers) to refill the tunnel excavated by the osteoclasts. Osteoid (visible as blue layers) eventually becomes mineralized bone (black).

1. Introduction

Remodeling is not only responsible for replacing old bone, but it also allows to some extent to adapt bone structure and shape to changing mechanical demands (Huiskes 2000, Rayfield 2019). A healthy vertebral body shows trabeculae, which are mostly oriented in the vertical orientation, i.e. the orientation of the most common loading direction in our spine (Fig. 1.3 A). Fig. 1.3 B demonstrates how a shift in mechanical load, resulting from a bony connection between vertebral bodies, causes a reorientation of the trabecular structure, as well as a thickening of certain trabeculae (Mosekilde, Ebbesen et al. 2000, Fratzl and Weinkamer 2007). These adaptations redistribute the load over the lower surface of the vertebral body. Fig. 1.3 C demonstrates how trabeculae thicken to build a stress bridge to account for osteoporotic bone loss and shape changes, which occur with aging (Mosekilde, Ebbesen et al. 2000, Fratzl and Weinkamer 2007).

The exact mechanism of how bone accomplishes this adaptation is studied in the field of mechanobiology. One of the proposed models in this field is referred to as mechanostat, an analogy with a thermostat (Rubin and Lanyon 1984, Frost 1987). The mechanostat regulates if bone should be formed or removed by comparing the locally measured mechanical load to pre-defined set points. During disuse the stress in large parts of the bone is below the resorption threshold, which initiates resorption of mineralized bone which is at the moment not needed. In contrast, extra bone is formed when the local stress is above the formation threshold, to compensate for increased load. This does not only explain how bone tissue is always experiencing a similar mechanical strain in animals of very different size (Rubin and Lanyon 1984, Frost 1987), but it can even explain how the bone potentially adapts its structure to changing loads (Fig. 1.3 D). In this simplified model I illustrate how stresses above the formation threshold (red) lead to formation at the nearby surfaces, while the stress below the resorption threshold (blue) is removed. The combination of formation and resorption cause the modeled trabeculum to align with the applied stress. Many studies working on bone adaptation problems at the macro-scale are based on the mechanostat hypothesis (Frost 2003). The specific set point(s) of the mechanostat are unknown until now, while the outcome of predictive models are very sensitive for this parameter (Skerry 2006, Iwaniec and Turner 2016, Weinkamer, Eberl et al. 2019, né Betts, Wehrle et al. 2020). Some bones are very sensitive for changes in load (for example, the bone loss in space or unloading due to a splint), while other bones seem to be immune for a lack of load, such as the skull. Moreover, Skerry (2006) suggests that there is a different local set point at each location in the skeleton, which nowadays still causes difficulties in predicting adaptive bone responses (Carriero, Pereira et al. 2018).

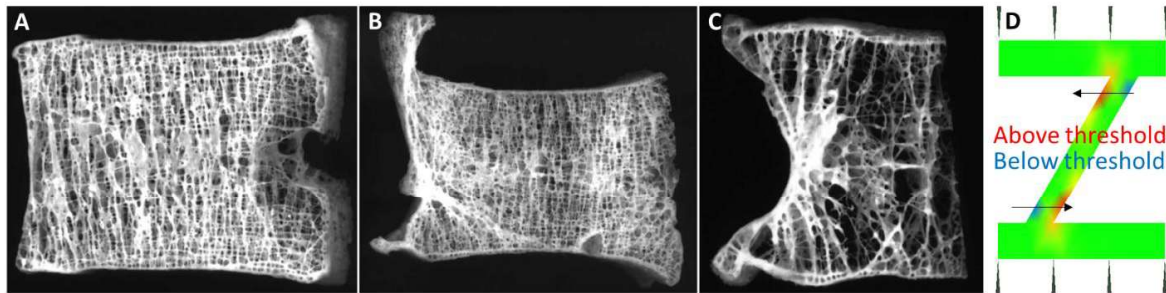


Fig. 1.3. A-C) The internal structure of vertebral bodies adapt to changing loading conditions (Mosekilde, Ebbesen et al. 2000). A) Physiological loading of our back mostly causes stresses along the direction of our spine. The healthy vertebral body shows an internal structure which is mostly aligned with this physiological stresses. Horizontal trabeculae resist the lateral stress due to expansion transversal to axial strain. B) The formation of a bony bridge between two vertebral bodies (top, to the left of the vertebra) alters the loading conditions, and causes an adaptation of the internal structure of the bone. C) The thickening of trabeculae compensates for bone loss (i.e. decreased number of trabeculae with age) D) Based on the stress distribution the mechanostat model predicts that this simulated trabecula rotates into the loading direction by placing extra bone where needed (red) and removing bone where not needed (blue).

1.1 The Hierarchical Porosity in Cortical Bone

To understand how the dense cortical bone senses mechanical loads, we approach bone not as a purely solid material, but as a porous fluid filled material. In this study, we consider three hierarchical levels of nested network-like porosity in bone, containing blood or interstitial fluid within cortical bone. The largest pores embedded in the cortex are the vascular canals (level 1). The first investigating these canals was Antoni van Leeuwenhoek using one of his newly invented light microscopes. The length scale of the vascular pore network ranges from several decimeters down to tens of micrometers (table 1.1.). Van Leeuwenhoek (1677) found that the apparently solid cortex of certain bones was made out of a large number of parallel tubular structures. Looking at cortical bone with a modern scanning electron microscopy, we can indeed see a large number of roundish structures (tube-like in three dimensions). These osteons, are visible due to a distinct mineral content of the bone compared to the environment, and a hole – the Haversian canal in its center (Fig. 1.4 B). The Haversian canals are aligned along the long axis of the long bones. The diameter of human osteons is in the order of 100 μm . The Haversian canals are tens of micrometers in diameter and are part of a large interconnected network throughout the whole cortex, in which we can find nerves and blood vessels (Herskovits, Singh et al. 1990, Cowin and Cardoso 2015). The Haversian canals are connected to each other via Volkmann canals, which are transverse vascular canals that are oriented perpendicular with respect to the Haversian canals (Fig. 1.4 B). The space in the Haversian canal, outside the blood vessels and nerves, is mostly filled with interstitial fluid. It is crucial that the blood pressure is higher than the pressure of the interstitial fluid outside of the blood vessels, as the very soft vessels and capillaries would otherwise easily

collapse. The transport of fluid over the blood vessel wall is balanced by the colloid osmotic pressure of the blood plasma, which allows controlled exchange of, for example, water, minerals, nutrients and waste products over the capillary vessel wall (Heyeraas and Berggreen 1999).

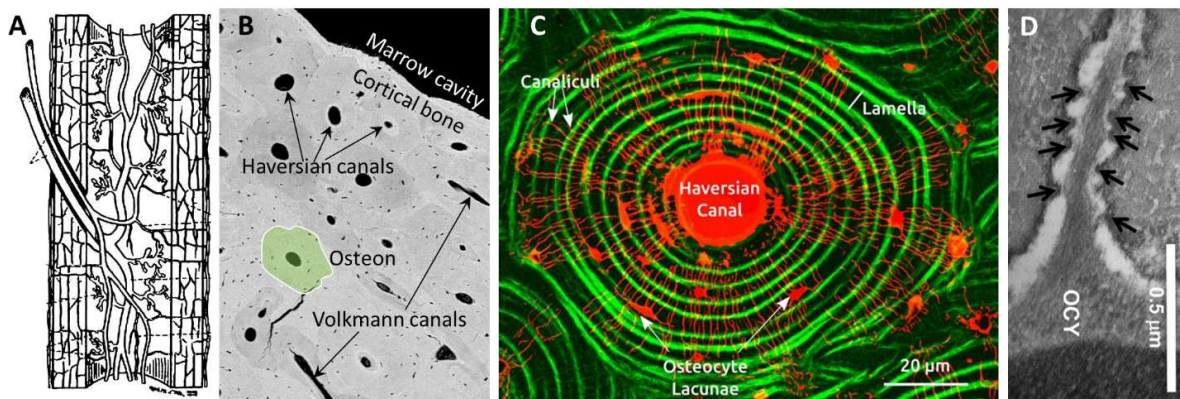


Fig. 1.4. An overview of the three levels of bone porosity within human cortical bone. A-B) Level 1: The vascular porosity. A) In long bones there is a vast capillary network in the cortical bone, as illustrated here in the drawing from Cowin and Cardoso (2015). B) Our qBEI image of a cross section of the human cortical bone (midshaft femur) clearly show the vascular canals, which are tens of micrometers in diameter, contain the capillaries and nerves. The canals which are oriented along the long axis of the bone are called Haversian canals, and are part of osteons (marked green). Volkmann canals connect the Haversian canals with each other and with the surfaces of the cortex. C) Level 2: The lacunocanalicular network (imaged using confocal laser scanning microscopy (CLSM) after rhodamine staining, a red fluorescent dye). This network extends over the scale of osteons, consisting of concentric rings of mineralized bone matrix (imaged with reflection, shown in green) around the Haversian canals. Level 3: A single canaliculus, housing the osteocyte cell process (tunneling electron microscopic photomicrograph, from Cabahug-Zuckerman, Stout et al. (2018)). The light zone around the cell process is the pericellular space. Arrows indicate narrowings in the canaliculus. The osteocyte cell body is marked by OCY.

When we zoom in further, we find that each osteon contains a lacunocanalicular network (LCN) (Fig. 1.4 C, level 2), consisting of lacunae, which are connected by sub-micrometer wide canaliculi (Fig. 1.4 C, D, level 3). The cell bodies of the bone cells (osteocytes) live inside the lacunae and use the canaliculi to connect to other osteocytes with their cell processes (Fig. 1.4 D). Canaliculi are funnel shaped where they connect to large pores, such as the lacunae (Fig. 1.4 D) and the Haversian canals (Fig. 1.4 C) (Lin and Xu 2011). At the outer boundary the osteons are mostly sealed off from the rest of the bone by a cement line (Milovanovic and Busse 2019), as only very few canaliculi are bridging the cement line. In contrast, the Haversian canals are well connected to the LCN through many canaliculi and most canaliculi in the osteon are radially oriented to the Haversian canal (Fig. 1.4. B) (Repp, Kollmannsberger et al. 2017). The remaining canaliculi are mostly perpendicular to the radial canaliculi and are associated with the osteocyte lacunae. The lamella (Fig. 1.4 C) of the osteon can be made visible due to the reflection of light by aligned

collagen fibers. The collagen orientation follows a distinct plywood structure, and lacunae and perpendicular canaliculi are co-aligned with the lamella (Kerschnitzki, Wagermaier et al. 2011, Lin and Xu 2011, Repp, Kollmannsberger et al. 2017). It should be noted that not all types of cortical bone have osteons. The cortex of the mouse tibia, for example, has a network of blood vessels and lacunocanalicular network, but is lacking secondary osteons. Roughly two types of bone, with each their own typical LCN architecture, can be found in the mouse tibia. 1) Woven bone, with very disordered network and irregularly shaped lacunae (Kerschnitzki, Wagermaier et al. 2011, Ip, Toth et al. 2016, Shapiro and Wu 2019). This bone is rapidly produced during the initial formation of the bone, and roughly defines the shape of the young bone (Kerschnitzki, Wagermaier et al. 2011, Ip, Toth et al. 2016, Shapiro and Wu 2019). 2) After that, bone is deposited layer by layer, forming lamellar-like bone top of the woven bone with very dense and well-ordered network and regularly shaped osteocytes (Kerschnitzki, Wagermaier et al. 2011, Ip, Toth et al. 2016).

Table 1.1. The length scales in the hierarchical structure of bone

1 m	Whole bone		Vascular network in bone	
10 ⁻¹ m				
10 ⁻² m	Trabecular network			
10 ⁻³ m	Trabeculae	Distance between osteons		Blood vessels
10 ⁻⁴ m	LCN	Osteons		
10 ⁻⁵ m	Lacunae	Osteocyte cell bodies		
10 ⁻⁶ m	Distance between canaliculi			
10 ⁻⁷ m	Canaliculi	Osteocyte cell processes		Pericellular space
10 ⁻⁸ m				
10 ⁻⁹ m	Proteoglycans	Integrins	Fiber spacing	Signaling molecules

Weinbaum, Cowin et al. (1994) proposed that the pericellular space in the canaliculi, situated between the osteocyte cell processes and the mineralized canalicular wall, is filled by a pericellular matrix (PCM) of cross-linked proteoglycans and an interstitial fluid (Fig. 1.5). The pericellular space has an open connection to the interstitial space in the vascular canals via the LCN. Advances in sample preparation enabled Weinbaum and colleagues a decade later to image the PCM in the bone of mice with SEM (**YOU, WEINBAUM ET AL. 2004**). The average diameter of the canaliculi in these mice was found to be 259 ± 129 nm. The large variation in this diameter can be explained by the fact that canaliculi are wider close to the lacunae (Fig. 1.4 C) and at junctions in

the LCN (**Wittig, Laugesen et al. 2019**). The average width of the annular pericellular space was found to be 78 ± 38 nm and symmetric around the long axis of the canaliculi (**YOU, WEINBAUM ET AL. 2004**). They concluded that the PCM is a fiber network that fills the pericellular space, and that tethering elements bridge between the osteocyte cell processes and the mineralized canalicular wall (Fig. 1.5). Although it is commonly assumed that the diameters of different canaliculi are similar, a number of studies showed that canaliculi have a rough surface. At random locations along the canaliculi there are “canalicular projections” (Fig. 1.4 D, black arrows), which are the focal adhesion points for integrins. It is suggested that integrins are mechanosensory molecules, responsible for measuring the fluid flow velocity through the pericellular space of canaliculi. Unfortunately, sample preparation procedures nowadays are still not perfect. Dehydration is causing partial destruction and deformation of the samples. With the high likelihood of lost and collapsed fibers in mind, it can be concluded that the PCM definitely exists, but that the reported 40 nm spacing between the bridging fibers is overestimated (**CARDOSO, FRITTON ET AL. 2013**). Therefore, the exact composition and structure of the PCM are still very uncertain.

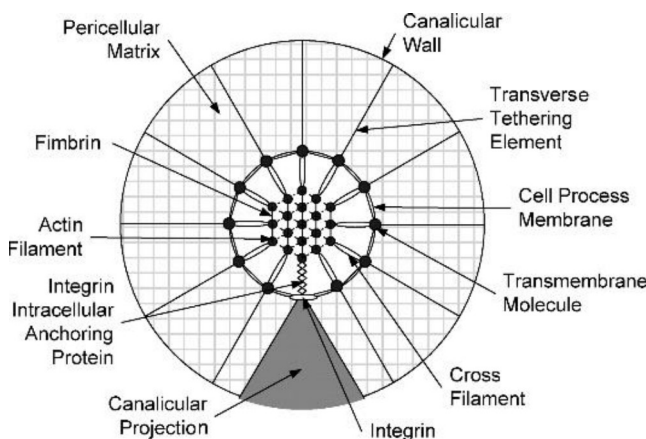


Fig. 1.5. Idealized cross section of a canaliculus with its osteocyte cell process and pericellular matrix (Wang, McNamara et al. 2007) (Copyright (2007) National Academy of Sciences). The grey triangle at the bottom illustrates how randomly situated projections of the canalicular wall probably form adhesion foci, where mechanosensitive integrins are situated between the cell membrane to the canalicular wall.

1.2 Multifunctionality of the Osteocyte Network

Although we focus on the role of the lacunocanalicular network (LCN) in mechanosensing, it is assumed that the LCN and the osteocyte network it houses are multifunctional. Very strictly regulated mineral homeostasis is essential for life, and bones store a large amount of mineral, in particular calcium and phosphate. If the calcium concentration is not kept in a very narrow window, then nerves and muscles (including the heart) would not function properly and a constant phosphate concentration is critical for energy metabolism and protein synthesis. The need of a vast transport network with direct access to a high density mineral storage is therefore critical. The LCN is a vast transport network with a 100 times larger surface area than the area that osteoclasts

and osteoblasts encounter at the surface of the bone (Marotti, Ferretti et al. 1995, Buenzli and Sims 2015). Therefore, the LCN has much better access to the bone mineral compared to the vascular network alone, giving it the potential to quickly regulate the calcium and phosphate concentrations in blood. Based on the strong heterogeneities in LCN architecture it could be expected that storage sites with higher transport potential and storage potential exist (Roschger, Roschger et al. 2019). The area around bone resorption contains high levels of the enzymes associated with osteoclastic activity. Some of these enzymes can also be expressed by osteocytes (Kogawa, Wijenayaka et al. 2013). Osteocyte perilacunar remodeling has been shown, and there is evidence of canalicular remodeling (Teti and Zallone 2009, Qing, Ardeshipour et al. 2012, Ormsby, Cantley et al. 2016). Therefore it is not surprising that we found that the local bone mineral properties correlate with the osteocyte network topology (Kerschnitzki, Kollmannsberger et al. 2013, Roschger, Roschger et al. 2019).

Most important for the current study is the osteocytes' ability to sense the mechanical loads the bone is placed under in order to orchestrate bone remodeling. Although there is no direct evidence for this due to substantial experimental challenges, the osteocyte is a promising candidate to be the mechanosensor of bone. If this is true, they form a distributed sensor network with roughly 70 km of canaliculi in each cubic centimeter of cortical bone (Repp, Kollmannsberger et al. 2017, Roschger, Roschger et al. 2019). However, there is a problem: Since the strains in bone ($<0.2\%$) do not overcome the strain threshold ($>10\%$) to which osteocytes respond in *in vitro* experiments. Two main hypotheses, which are not necessarily mutually exclusive, were therefore proposed to explain the mechanism of indirect biophysical stimulation of osteocytes. Microdamage can interrupt cell processes and lead to osteocyte apoptosis and subsequent triggering of bone remodeling (Burr et al. 1985; Verborgt et al. 2000). Alternatively, load-induced flow of interstitial bone fluid throughout the LCN and the resulting shear forces on the cell surface are regarded as mechanical stimulus that can be sensed by osteocytes (Weinbaum et al. 1994). The latter hypothesis is supported by *in vitro* studies which demonstrated that osteocytes are particularly sensitive to shear stresses in the range from 0.4 to 2 Pa (Jacobs et al. 2010; Klein-Nulend et al. 1995) and that their cell processes are more sensitive than the cell bodies (Adachi et al. 2009).

After detection of the mechanical loads via shear forces on the cell membrane, the osteocytes have to communicate with cells outside of the mineralized tissue to orchestrate the bone mechanoreponse. One of the possibilities is that osteocytes, based on the mechanical loads they experience, release a set of signaling molecules to control bone resorption by osteoclasts and bone formation by osteoblasts (Klein-Nulend and Bonewald 2020). The Wnt pathway, which is one of the most important biochemical signaling pathways for the mechanoreponse of bone, begins with transmembrane proteins that pass signals into the osteocyte. When there is no mechanical stimulation of the trans-membrane Wnt protein, osteocytes inhibit bone formation by releasing signaling molecules such as sclerostin and DKK1 (Winkler, Sutherland et al. 2003, Robling, Castillo et al. 2006). At the same time the Wnt pathway causes a release of RANKL, which recruits

bone resorbing osteoclasts. When osteocytes are mechanically stimulated they release nitric oxide (NO). NO inhibits resorption by osteoclasts and recruits osteoblasts for formation of new bone. NO is a reactive molecule, which converts into NO₂ when exposed to oxygen, and therefore has only a limited lifetime. Based on the complexity of the architecture we could also speculate that the osteocyte network could process and transport the sensory information in a similar way as part of our nervous system processes and transports data. Evidence for the distributed sensor network is that calcium spikes (i.e. bioelectrical signals) encode the magnitude and frequency of mechanical loading and that osteocytes communicate via mechanisms similar to the nervous system (Guo and Bonewald 2009, Lewis, Frikha-Benayed et al. 2017). It is well known that the architecture of neural circuits is a key factor for distributed processing, for example in vision, and that we learn by modifying the architecture of our neural networks (Katz and Shatz 1996). It is therefore very interesting to investigate if the LCN architecture plays a role in both mechanosensing and processing of the sensory data, especially since both the LCN and mechanoresponsiveness deteriorate with age (Tiede-Lewis and Dallas 2019).

The dense mineralized bone does not only form a barrier for the signaling molecules, but also for molecules that are essential for cell viability (i.e. nutrients, oxygen, waste products and minerals). Transport is therefore a function of the LCN which is essential for the viability of the osteocytes it houses. It has been experimentally shown that solutes diffuse through the pericellular space of the LCN in bone (Wang, Wang et al. 2005, Zhou, Novotny et al. 2008, Zhou, Novotny et al. 2009, Price, Zhou et al. 2011, Wang, Zhou et al. 2013, Wang 2018). However, due to the PCM, there is a size limit for molecules to be transported through the LCN. Molecules of 6 nm and smaller can be used to stain the entire LCN, while molecules of 10 nm do not enter the canaliculi of rat bone at all (Wang, Ciani et al. 2004). This indicates that the spacing between the fibers of the PCM is not much larger than 10 nm. It has been speculated that the one of the functions of the fine net-like structure PCM is filtering interstitial fluid by physically preventing large, biologically unnecessary molecules to enter the LCN (CARDOSO, FRITTON ET AL. 2013).

1.3 Load-Induced Fluid Flow in Bone

It has been suggested that load-induced fluid flow through the LCN is the amplification mechanism, which makes it possible for osteocytes to sense the small (<0.2%) strains, which do not overcome the strain threshold (>10%) where osteocytes respond to in *in vitro* experiments. Tracer experiments demonstrated that load-induced fluid flow of interstitial fluid enhances transport in bone. While the blood flow is driven by hydraulic pressure gradients, the interstitial fluid flow can be driven by three different forces, (i) the hydraulic pressure, (ii) osmotic pressure and (iii) electrostatic forces (Cowin and Cardoso 2015). This, in combination with the sensitivity of cells to fluid shear stresses at their surface, are evidence that fluid flow can act as the necessary strain amplification lever (Weinbaum, Cowin et al. 1994). To model interstitial fluid flow in

bone, the Darcy velocity (i.e. the average velocity through a porous medium), $V_D = -k_p \nabla P - k_c \nabla n - k_E \nabla \psi$, considers three mechanisms. Namely the hydraulic flow due to pressure gradient ∇P , the osmosis due to the saline concentration gradient ∇n and the electro-osmosis due to streaming potential $\nabla \psi$. The relevant macroscopic permeabilities k_p , k_c and k_E are typically obtained via a so called homogenization process (Smit, Huyghe et al. 2002), where cortical bone is modeled as a homogeneous, linear, isotropic, porous medium. Therefore, macroscopic permeability parameters integrate geometric effects of the pore network architectures at smaller length scales, such as pore geometry, pore network connectivity and the spatial arrangement of the pores. It is common practice in the field of mechanobiology to neglect the flow due to osmosis and electro-osmosis, since the fluid flow is dominated by the effect of pressure gradients (Cowin and Cardoso 2015). In this thesis the focus will also be exclusively on the hydraulic flow of interstitial fluid.

1.3.1 Models of Fluid Flow in Bone – What Questions Can Be Asked?

The strong local variation in the mechanosensitiveness of bone stresses the need to consider the hierarchical structure of bone in multiscale computational models. Mechanical finite element models (FEM) are used to estimate strain patterns within the bone, while models at the smallest scale are used to gain an understanding in how the bone cells and proteins sense the mechanical environment. This section explores what questions we can answer with models at different hierarchical levels, starting at the whole bone level and ending with the ultrastructure of canaliculi. The aim of this section is not to provide a complete overview over the existing modeling literature, but rather to explain different model approaches and the corresponding research questions, which are asked with them. A restricted number of representative examples and their obtained results are presented in more detail.

1.3.2 Strain and Fluid Flow Patterns at the Organ Level

Loads applied to the bone pressurize the extracellular fluid in the LCN. The gradient in pore pressure developed over the canalicular length forces fluid to flow through the canaliculi. Poroelasticity (Biot theory) is the most common technique used to model the behavior of bone as a fluid saturated porous medium. The Biot theory could not only model elastic effects, but also predicts patterns of pore fluid pressure and fluid flow velocity (Kameo, Adachi et al. 2008). The Biot effective stress coefficient is just one of the possible parameters which relates stress and strain in the solid material to pore fluid pressure. The compressibility of the fluid filled pore (i.e. the relationship between volume change and pressure) is quantified using the Skempton pressure coefficient. The work of Cowin (1999) uses both these parameters to define the relationship between the pore fluid content, pore fluid pressure and applied the stress. Poroelasticity (Wang, 2000) assumes that due to the small pore volume fraction Hooke's law governs the deformation of the matrix material and that Darcy's law governs the fluid flow in poroelastic materials. Poroelastic

models assume isotropic behavior at the macroscale in stress–strain relations and fluid flow in poroelastic materials (Smit, Huyghe et al. 2002). Loads within the bone are rarely uniformly distributed. Srinivasan and Gross (2000) used a poroelastic-like approach combined with a realistic strain pattern, i.e. the typical bending which is often seen in the cortex of a long bone. More specifically, they modeled the fluid flow through a 2D analytical poroelastic multiscale model of the avian ulnar mid-diaphysis. The strain surface waveform was measured experimentally and the spatiotemporal strain pattern throughout the whole model was estimated using beam theory. The resulting mechanical boundary conditions were applied to a previously developed model of a single osteon to compute the local pore pressure in their multi-scale model (Zeng, Cowin et al. 1994). Although this model is very simplified, the study answered the question what effect non-uniform loading could have on fluid flow through canaliculi. They concluded that not only time-varying load causes a flow, but that the complete spatio-temporal load patterns have to be considered for an accurate prediction of fluid flow. When bone is strongly compressed the fluid flows in the direction of the bone surface, and the flow direction reverses during relaxation. The spatial gradient in loading also causes a gradient in pressure. Since per definition strain around the neutral axis in a beam is minimal, the load gradient is the main determinant of fluid flow here. Thus, the flow direction here is from low to high pressure (i.e. from the compression side to the tension side) rather than from and to the bone surface. Although this study does not consider a realistic LCN architecture, it shows the importance to consider the placement of canaliculi.

Finite element modelling is an excellent and well-developed tool to study the fluid flow of more realistic geometries. Although the effect of geometry on mechanical behavior is relatively well known, it was not yet known what the effect of poroelastic parameters on the fluid flow and pressure patterns is. Finite difference modelling in combination with the Biot theory and beam theory was therefore used to model the load-induced fluid flow patterns in a mid-diaphyseal section of the rat tibia subjected to four-point-bending (Steck, Niederer et al. 2000). It was assumed that the surface of the bone was impermeable and that there are no vascular canals present, which constrained the fluid to flow only between lacunae. In this parametric study the absolute values of fluid flow velocity changed, while the fluid flow patterns did not significantly change for all parameters used (Steck, Niederer et al. 2000). The pattern showed that the highest velocities always occurred around the neutral axis, where strains are minimal. This is in contradiction to the fluid flow hypothesis, as the sites of low fluid flow velocity are the sites where most bone formation happens *in vivo*.

Tiwari, Prasad and co-workers made several attempts to predict load-induced bone formation from load (i.e. stress, strain etc.) and load-induced fluid flow (Tiwari and Prasad 2017, Tiwari and Kumar 2018, Tiwari, Kumar et al. 2018, Tiwari and Prasad 2018, Prasad and Goyal 2019). For simplicity a non-poroelastic fluid flow model is used in these studies, where the local pressure is calculated directly from the local stress. Full poroelastic models predict nearly no fluid flow velocity near the neutral axis of a bending bone, where strain is zero, while Tiwari and Prasad

(2017) observed load-induced bone formation here. The tibia was modeled as a linearly elastic, homogeneous, isotropic cantilever beam to calculate the pore fluid pressure due to a sinusoidal bending moment (Kameo, Adachi et al. 2009). After this, Darcy's law was applied to predict the fluid flow velocity from the earlier predicted pore pressure gradient. Drawbacks of this non-poroelastic approach is that the preservation of mass is not considered and that permeability has no impact of the pressure pattern. Therefore, I suspect that the fluid flow near the neutral axis is strongly overestimated. Moreover, this study took the equation from a simplified cantilever (Kameo, Adachi et al. 2009) and it is not clear how this relates to the hollow and somewhat rounded shape of the cortical bone. Nevertheless, all models by Tiwari et al. concluded that fluid shear fails to explain the site-specific bone formation at the inner endocortical surface (Fig. 1.3 B), even if more stimuli were considered to improve the computational prediction of new bone formation. The predicted amount of new bone formation was higher at the outer periosteal surface compared to the endocortical surface. Since this is not in line with what is experimentally observed, they assume the endocortical surface to be more mechano-responsive than the periosteal surface.

In order to predict the remodeling response, Carriero, Pereira et al. (2018) used a full poroelastic FE model of a long bone undergoing bending, in which the surfaces of the bone were modeled as open boundaries (i.e. pressure at the surface is zero) and where preservation of mass was accounted for. The model was based on an *in vivo* experiment, where the mouse tibia was loaded. During the experiment newly formed bone was labelled twice using a fluorochrome, so that the remodeling response to the applied load could be measured as bone between the two labels (Fig. 1.3. B, left). The probability of finding bone formation was then compared to a purely mechanical parameter, strain energy density (SED), and fluid flow velocity (FLVEL in Fig. 1.3. B, right). This study showed that changing boundary conditions completely changes the fluid flow patterns. Furthermore, considering fluid flow increased the predictive value of their model. However, when the actual amount of new bone was taken into account, the model predicts considerably more new bone formation at the periosteal surface compared to what was observed in their experiments.

In conclusion, models of fluid flow in bone with homogeneous poroelastic properties show how important it is to carefully consider the boundary conditions. Fluid flow patterns qualitatively change when changing boundary conditions, such as non-uniformity of the strain field and sealing the surfaces of the bone. In contrast, there is no qualitative change visible in fluid flow and pressure patterns if the poroelastic properties of the material change. Models at this scale fail to provide an accurate prediction about the variation in mechanoresponse on different surfaces of the bone.

1.3.3. Two Pore Networks – The LCN and Vascular Porosity

The models described before neglect the fact that bone contains two networks, the vascular network and the lacunocanalicular network, with very different hydrodynamic properties (Cowin 1999). The different levels of porosity are commonly treated independently, based on the assumption that the pressure relaxation times of the vessel pores and the lacunae differ by roughly four orders of magnitude (Table 1.2). From the perspective of the LCN, the fluid pressure in the vascular porosity is quasi static, while from the perspective of the vascular canals the bone with its LCN is behaving like a solid. In models of fluid flow in bone the vascular canals are therefore commonly treated as low pressure reservoirs (i.e. $P = 0$ kPa).

Table 1.2. Poroelastic properties for the two levels of bone porosity (Cowin 1999).

Parameter	LCN	Vascular
Porosity	2.4 – 5 %	1.5 – 4 %
Permeability	$10^{-25} - 10^{-19} \text{ m}^2$	$10^{-15} - 10^{-13} \text{ m}^2$
Pressure relaxation time	4.9 ms	0.0014 ms
Biot effective stress coefficient, α	0.151	0.120
Skempton pore pressure coefficient, β	0.344	0.367

Simplified models of load-induced fluid flow in osteonal bone (i.e. bone with Haversian vascular canals) have been developed to simulate a more realistic physiological environment compared to the homogeneous solid bone models. Wang, Fritton et al. (1999) used an analytical approach to study load-induced fluid flow in case of dynamic bending and demonstrated that the regularly spaced Haversian canals provide a space for pressure relaxation (Fig. 1.7 A). The coupling between different osteons had only minimal effect on the local pressure amplitudes. The pressure profile around the canals were cusp-shaped and amplitudes were directly proportional to the local stress and strain and could explain experimentally observed load-induced electric potentials across osteonal bone. The recent FEM approach of Yu, Wu et al. (2019) modeled idealized cortical bone, consisting of regularly shaped and spaced Haversian canals in a cylindrical shell (Fig. 1.7 B). The largest qualitative differences between the results from this study and the study of Wang, Fritton et al. (1999) were the fluid flow and pressure profiles near the surfaces of the bone. The open surface of Yu, Wu et al. (2019) caused a band of low pressure at the surfaces (Fig. 1.7 B, left), and the resulting pressure gradient caused a fluid flow through these surfaces of the bone (Fig. 1.7 B, right).

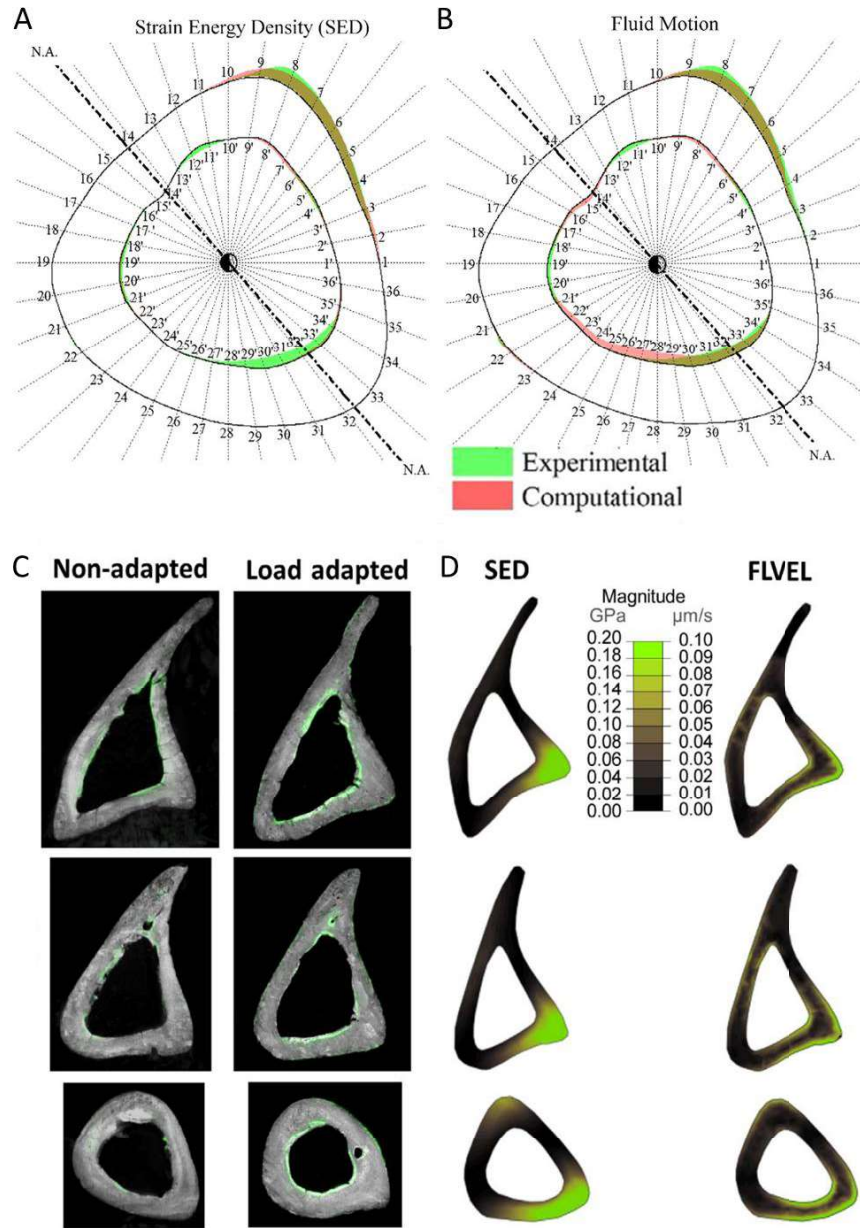


Fig. 1.6. Models of fluid flow in bone geometries reconstructed from μCT scans, used to predict the response of bone to mechanical loading. A) Predictions of load-induced bone formation based on strain energy density (SED) (Tiwari, Kumar et al. 2018). B) Prediction of load-induced bone formation based on the fluid flow hypothesis. This modelling approach calculates flow based on the stress gradient and neglects the preservation of mass and the location of the neutral axis is estimated by hand (Tiwari and Prasad 2017, Tiwari, Kumar et al. 2018). C) Comparison of remodeling of a non-loaded mouse bone compared to a loaded mouse bone (Carriero, Pereira et al. 2018). Newly forming bone was stained *in vivo* with a commonly used green fluorescent dye (calcein), which gets incorporated in mineralizing tissue after injection. D) Carriero, Pereira et al. (2018) compared the observed new bone formation to SED and a full poroelastic model, where preservation of mass and pore volume changes were taken into account. Note that this model leads to a completely different fluid flow pattern compared to the model in (A), where fluid flow

1. Introduction

velocities (FLVEL) are higher near the surfaces of the bone, and does not predict new bone formation near the neutral axis.

As becomes obvious from Fig. 1.4 B, the osteons are not regularly spaced and show a large variety in shape and size. Gatti, Azoulay et al. (2018) used μ CT scans of bones of a rat model, with and without osteoporosis, to study the effect of vascular canal size on load-induced fluid flow and pressure. The size of the vascular porosity in the osteoporotic rat bone is severely increased compared to healthy rat bone (Fig. 1.7 C). In addition, they did a parametric study to investigate the effect of LCN permeability, since the permeability of canaliculi is still unknown. This study showed that the increase of vascular porosity had a major effect on the fluid flow patterns and magnitudes, while changes in permeability had only a minimal effect. For permeabilities larger than 10^{-21} m^2 the average fluid flow velocity was directly proportional to strain rate. The fluid flow velocity near the surface of vascular canals was inversely proportional to the diameter of these canals. This can partly be explained by Gauss's law, as the same amount of fluid flows through a larger surface area. Based on this Gatti, Azoulay et al. (2018) concluded that osteoporotic bone is less mechanosensitive, and that there possibly is a positive feedback loop, which plays a role in the progression of osteoporosis in cortical bone.

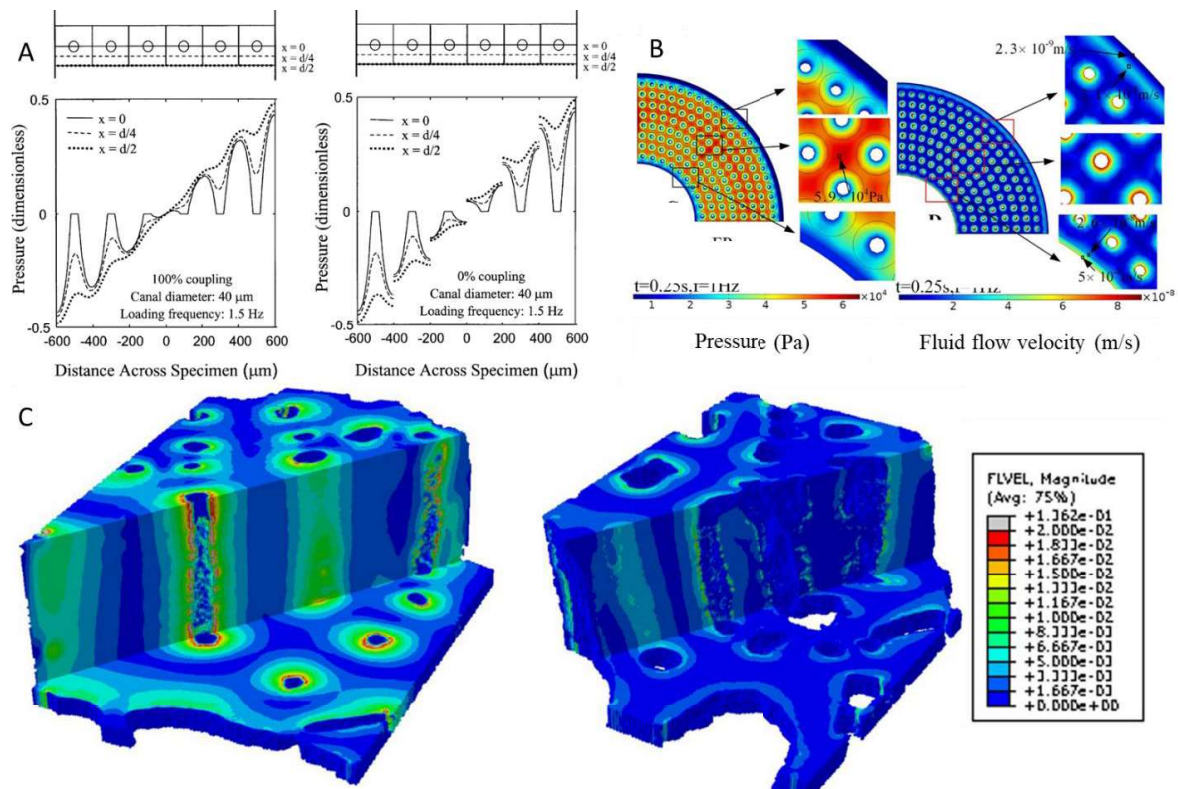


Fig. 1.7. Multiscale models of fluid flow in bone that include the vascular porosity. A) Idealized model osteons without interstitial bone, developed by Wang, Fritton et al. (1999), showed that the permeability of cement lines has only a minimal effect on fluid flow and pressure induced by dynamic bending. This indicates that the stress gradient over the bent bone only causes a minimal amount of fluid flow, and that the distribution of vascular canals within is dominant in determining pressure profiles of cortical bone. B)

A multiscale model of an idealized human cortex with osteons developed by Yu, Wu et al. (2019) shows that in general fluid flow in the bone between osteons (interstitial bone) is near zero, except for the interstitial bone near the surfaces of the bone, where fluid can leak out. Therefore, even in this idealized symmetric model under uniform load, the fluid flow patterns in osteons near the surface of the bone are heterogeneous. Over the whole cortex the fluid flow velocity strongly correlated to the time derivative of the von Mises stress (a scalar stress value calculated from the local stress tensor). C) A detailed poroelastic FE model, using μ CT scans of the rat cortex, compared healthy bone (left) with osteoporotic bone developed by Gatti, Azoulay et al. (2018). The fluid flow in the pathological case is lower, due to larger surface area of the pores over which the fluid is distributed, and therefore this study concluded that osteoporotic bone is probably less mechanosensitive.

From these multiscale models, we can learn how large the impact of vascular porosity on the load-induced fluid flow patterns in bone is. Additionally, these models indicate that flow in well vascularized bone is relatively local, as there is no bulk transport of fluid from the compressive side to the tensile side of the bending bone. This is in sharp contrast with the results of solid homogeneous cortical bone models (Srinivasan and Gross 2000, Tiwari and Prasad 2017). What is still missing from this modeling approach, though, is an explanation for local differences in the mechanoresponsiveness of bone.

1.3.4. Fluid Flow in Human Osteons

Several studies developed and extended mathematical analytical modeling of a single osteon to study the effect of different boundary conditions on the load-induced fluid flow (Pollack, Petrov et al. 1984, Weinbaum, Cowin et al. 1994, Zeng, Cowin et al. 1994, Wu and Chen 2013, Wu, Wang et al. 2016). Analytical models require a simple geometry and a homogeneous idealized LCN architecture (Fig. 1.8 A). Canaliculi were assumed to be straight and cover the whole distance from the Haversian canal to the cement line (roughly 100 μ m in length). Based on the two-pore level assumption pore pressure at the Haversian canal was assumed to be zero. Fluid flow velocity, and therefore, also pore pressure gradient (∇P), were assumed to be zero at the cement line. These models provide estimates of LCN permeability and fluid pressures, which could not be measured, and therefore have historically been very important for understanding of many aspects of LCN fluid flow. Although analytical models found that the exact time course of cyclic loading has an influence on fluid flow and the spatial-temporal pressure pattern (Kumar, Tiwari et al. 2019), the fluid flow velocities and resulting shear forces found in these studies were in the range where cells are responding to *in vitro*. Most studies concluded that both loading frequency and amplitude are directly proportional to osteonal fluid flow and pressure, and therefore the key loading parameter is strain rate (Zhang, Weinbaum et al. 1998, Zhang, Weinbaum et al. 1998, Wang, Cowin et al. 2000, Qin, Lin et al. 2002, Gururaja, Kim et al. 2005, Wu and Chen 2013). While permeability had little influence on the fluid velocity, it strongly affected the pressure patterns. This is due to the fast relaxation of flow in the LCN ($\sim 10^{-3}$ s, see table 1.2), which is a quantity that could be measured *in situ* (Tate, Niederer et al. 1997, Tate, Niederer et al. 1998, Wang, Wang et al. 2005) or indirectly assessed via streaming potentials (i.e. electrical potentials which are generated by the

1. Introduction

flow of ions) (Starkebaum, Pollack et al. 1979, Pollack, Petrov et al. 1984, Zeng, Cowin et al. 1994, Wang, Fritton et al. 1999, Qin, Lin et al. 2002).

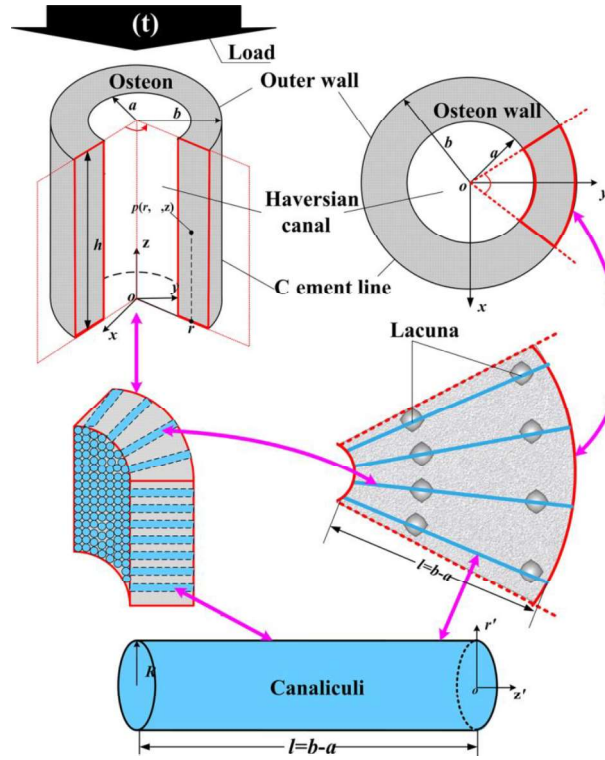


Fig. 1.8. A) Illustration of the hierarchical model of an idealized LCN within a human osteon by Wu, Wang et al. (2016). The model assumes a uniaxial load on a cylindrical hollow osteon and is based on the Weinbaum, Cowin et al. (1994) approach. The cement line is assumed to seal off the osteon, while the border to the Haversian canal is modeled as fully permeable. Canaliculi were modeled as straight radial connections between regularly spaced lacunae, without any other interconnection. The fluid flow and pressure patterns can be solved analytically in these models due to the homogeneous network and simple geometry.

The poroelastic properties of bone are not necessarily homogeneous and osteons are not regularly shaped. The flexibility of FE models can simulate geometrical irregularities more accurately. Consequently, FE approaches were used in a number of studies to investigate the effect of more complex scenarios, such as heterogeneous mechanical properties, heterogeneous permeability, presence of micro-cracks (Fig. 1.9) and lamellae (Tami, Nasser et al. 2002, Remond, Naili et al. 2008, Nguyen, Lemaire et al. 2010, Wu, Wang et al. 2014, Yu, Wu et al. 2019). These studies show that changes in the mechanical environment within the osteon strongly influence the local fluid flow and pressures, and, therefore, support the hypothesis that the bone can sense these changes indirectly by measuring the canalicular fluid flow.

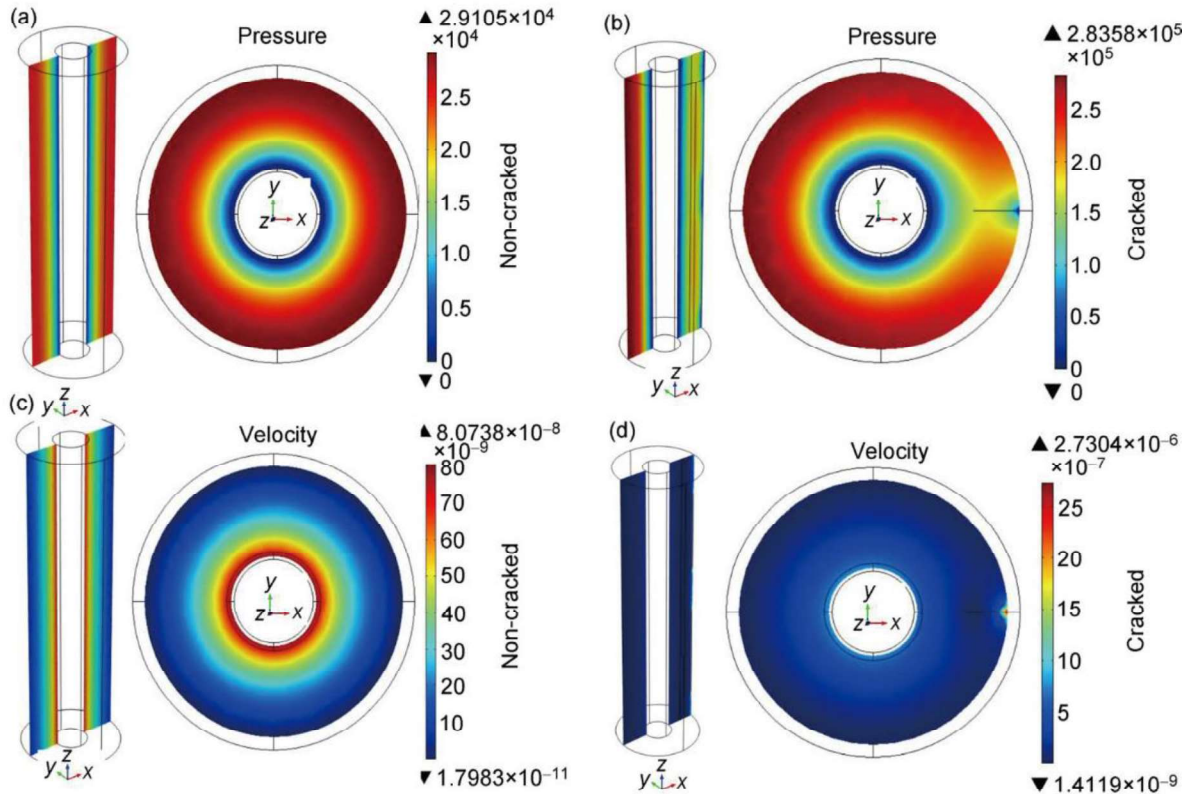


Fig. 1.9. An idealized poroelastic model of a human osteon (Wu, Wang et al. 2014). The pressure (a) and fluid flow velocity (c) in the ideal osteon show a smooth gradient, without any angular variation. The introduction of a crack in the model (black line in (b)) has a severe impact on the pressure (b) and fluid flow velocity (d) patterns.

Smit, Burger et al. (2002) and Burger, Klein-Nulend et al. (2003) exploited finite element modelling to explain the direction in which new osteons are formed (Fig. 1.10). Osteons are the result of intracortical bone remodeling. Osteoclasts dig a cylindrical canal through the bone, which is later filled by osteoblasts to form a new osteon. Based on the fluid flow hypothesis, Smit et al. predicted that due to the low fluid flow velocity in the cutting cone osteoclasts are recruited by the low-stimulated osteocytes to resorb bone in the loading direction. Due to the resorption fluid flow velocity increases in the walls of the pore, which lead to recruitment of osteoblasts to form the closing cone of the newly formed osteon. The fluid flow velocity in the closing cone was found to be 5 times higher than in the cutting cone. What cannot be explained by this model is how Volkmann canals are formed, since these canals are oriented perpendicularly to the loading direction.

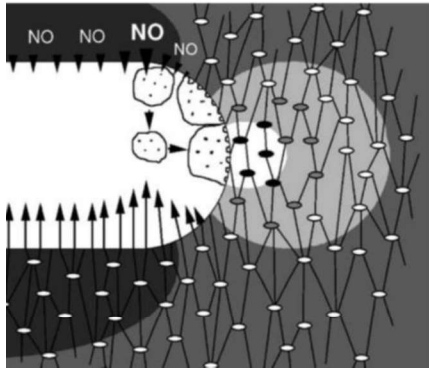


Fig. 1.10. An illustration of a model by Burger, Klein-Nulend et al. (2003) how fluid flow through the LCN could regulate osteoclast activity, and by doing so they could predict the orientation of new osteon formation. They proposed that osteocytes become apoptotic in the area of low fluid flow, which attracts osteoclasts in the cutting cone tip. Osteocytes behind the cutting cone experience higher fluid flow velocities than usual, and therefore release biochemical signals (like nitric oxide (NO)). NO signals the osteoclasts to withdraw from the bone surface in the closing cone, trapping the osteoclasts in the cutting cone. When the osteoclasts make space, a reversal zone is formed where osteoblasts form the lamella of the newly formed osteon.

These models showed that predicted fluid flow velocities, induced by physiological dynamic loading of bone, are high enough to be comparable to those which stimulate osteocytes *in vitro*. In these models fluid flow is the signal, which is measured by the osteocytes. However, there must be a translation from flow at the tissue level to biological signals, in a process called mechanotransduction.

1.3.5. Fluid Flow and the Ultrastructure of Lacunae and Canaliculi

In order to answer the question what fluid drag or shear forces the cells experience another level of hierarchy should be studied. Experiments indicate that the cell processes are the most sensitive parts of the osteocytes (Klein-Nulend and Bonewald 2020). Several modeling studies have investigated the role of realistic geometries on mechanosensation by the osteocytes and their cell processes (Anderson, Kaliyamoorthy et al. 2005, Anderson and Tate 2008, Tate, Steck et al. 2010, Kamioka, Kameo et al. 2012, Verbruggen, Vaughan et al. 2012, Verbruggen, Vaughan et al. 2014, Vaughan, Mullen et al. 2015). These studies indicate that the canaliculi experience the highest fluid flow velocities (Fig. 1.11 A) and that narrower parts of canaliculi experience higher fluid shear stresses at the cell membrane (Anderson and Tate 2008, Kamioka, Kameo et al. 2012) (Fig. 1.11 B). These rely on high resolution imaging, which limits the field of view to single lacunae and canaliculi. Therefore the architecture of the surrounding LCN is unknown. This makes the choice of boundary conditions at the end of the canaliculi challenging.

The hypothesis that cells sense stresses on their surface, which are directly caused by the fluid shear at the cell surface, was further refined and specified (Weinbaum, Cowin et al. 1994, Klein-Nulend, Vanderplas et al. 1995). Within this refinement it is assumed that the cells are stimulated via the drag force on the pericellular matrix (PCM) via integrin transmembrane receptors. It was found that the narrower gaps with tethering fibers in the canaliculi (marked with arrows in Fig. 1.4 D) are associated with locations of integrins (Cabahug-Zuckerman, Stout et al. 2018, Geoghegan, Hoey et al. 2019). Fluid (and small molecules) are not bound to the PCM, as mentioned in section 1.1, but it can freely flow through the PCM in the canaliculi. The PCM will cause drag though, which limits the flow through canaliculi in a similar way as electrical current is curbed by resistors.

Substantial pressure gradients are, therefore, needed to force flow through the canaliculi. The most commonly used model for fluid flow in canaliculi assumes that the drag by the PCM can be modeled as a homogeneous permeability, as illustrated in Fig. 1.12 (Weinbaum, Cowin et al. 1994). This model assumes that the canaliculi and cell processes are straight and cylindrical, with constant diameter. Consequently, fluid flow is described in a cylindrical coordinate system with z denoting the direction of the fluid flow (i.e., parallel to the canaliculus) and r the radial direction (i.e., perpendicular to the canaliculus).

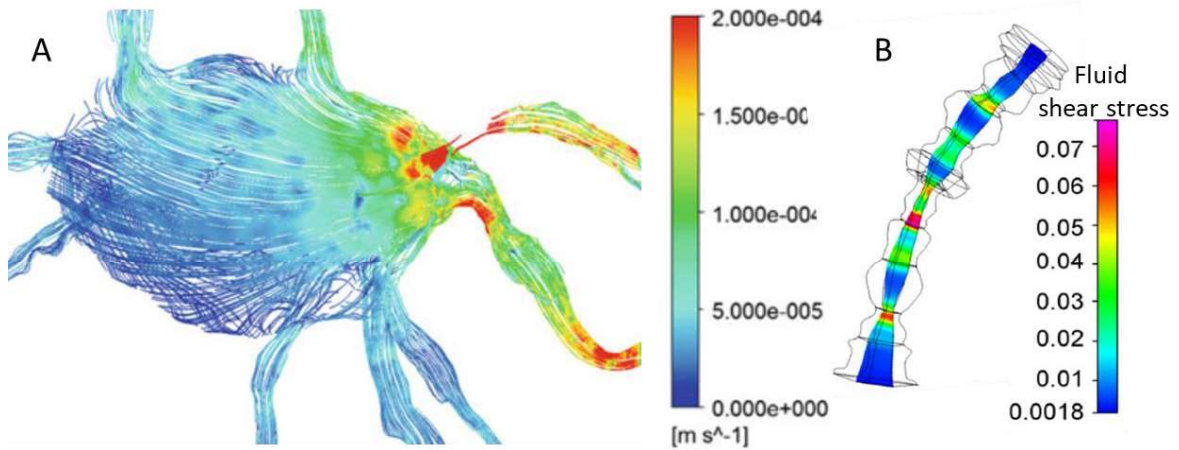


Fig. 1.11. A) Stream lines of modeled fluid flow through the pericellular space of an osteocyte (Verbruggen, Vaughan et al. 2014). The shape of the osteocyte lacuna is based on 3D confocal microscopy images. This study gives an indication of the heterogeneity of fluid flow velocities around the osteocyte. B) Simulated fluid shear stress on the membrane of the osteocyte cell process, in a model of fluid flow through a rough pericellular space geometry (Anderson and Tate 2008). Shear forces are particularly high in the narrower gaps of the canaliculus.

In the model the pressure gradient results from the drag of fluid flow through the PCM alone (i.e. far away from any surface), and can be calculated using Darcy's law:

$$\frac{dP}{dz} = -\mu \frac{v_{\infty}}{k_p}, \quad (1.1)$$

where dP/dz is the pressure gradient in the canaliculus, μ is the viscosity of the interstitial fluid, v_{∞} is the maximum fluid flow velocity (Darcy velocity) and k_p is the permeability of the PCM. For a purely viscous flow in an open pericellular space (i.e. without PCM, as illustrated left in Fig. 3) we can calculate the fluid shear stress as:

$$\tau = \mu \frac{dv}{dr} \quad (1.2)$$

1. Introduction

The Brinkman equation combines the effect of the drag caused by the PCM and fluid shear stress caused by the no slip boundary. Since we assume a quasi-static homogeneous pressure gradient (i.e. independent of time and position) in the direction of z , the Brinkman equation can be written as:

$$\frac{dP}{dz} = \mu \left(\frac{d\tau}{dr} - \frac{v}{k_p} \right) = \mu \left(\frac{d^2v}{dr^2} - \frac{v}{k_p} \right) \quad (1.3)$$

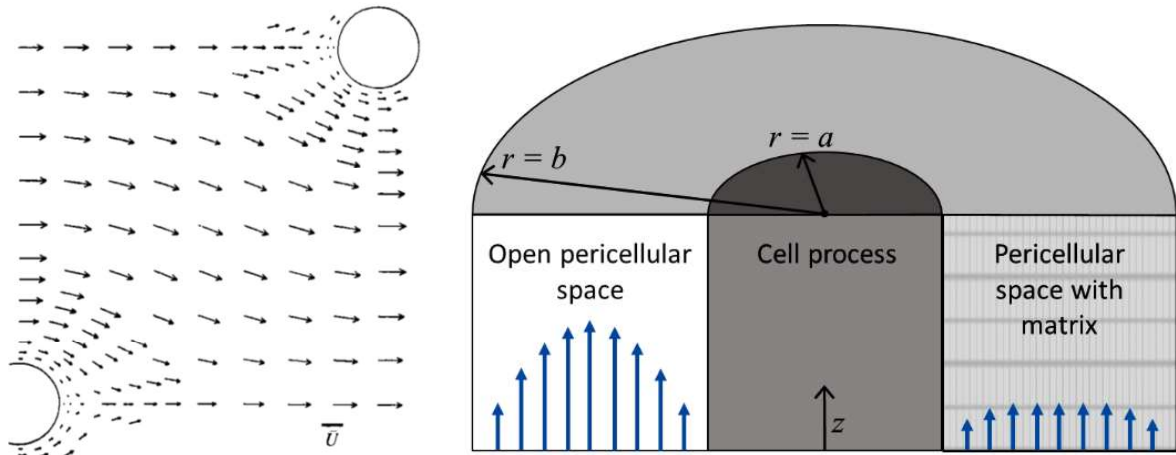


Fig. 1.12. A) An illustration of flow through an idealized homogeneous matrix of round fibers in the pericellular space of the canaliculus by Tsay and Weinbaum (1991). The fluid velocity field shows the viscous flow as it is forced around the fibers. This is causing drag, and therefore a lower effective permeability. B) An illustration of the strong effect that the drag from the pericellular matrix (PCM) has on the fluid flow profiles in canaliculi. The blue arrows in the left illustrate a fluid flow profile typical for an open pore (i.e., no matrix) and no-slip boundary conditions. The right velocity profile is flattened due to the drag from the PCM, which limits the maximum velocity. To increase the readability of this figure the relative diameter of the cell process is drawn out of scale, i.e. much smaller than in reality.

Note that at the surface of the canaliculi and the cell processes, where u is zero, or when the permeability k_p is infinite, this equation simplifies to the commonly used Stokes equation ($\nabla P = \mu \nabla^2 \mathbf{v}$). The solution of the Stokes equation follows a flow profile, which is close to a parabolic shape, while fluid flow velocity calculated by the Brinkman equation, shows a flattened flow profile when permeability k_p is low, as illustrated in Fig. 1.13 A. The flattening of the flow profile leads to an effective permeability, $k_{p,eff}$, which is lower than k_p .

$$k_{p,eff} = \frac{Q}{\pi(b^2 - a^2)} \cdot \mu \left(\frac{dP}{dz} \right)^{-1}, \quad (1.4)$$

where the average fluid flow velocity \bar{v} is equal to volumetric flow rate Q (i.e. the volume which flow through the cross section of the canaliculus per unit of time) divided by cross sectional area of the pericellular annulus (see Fig. 1.2. B for the definition of a and b),

$$\bar{v} = \frac{Q}{\pi(b^2 - a^2)} \quad (1.5)$$

The continuity equation in fluid dynamics assumes that Q is constant within a canaliculus, even if its geometry (i.e. a and b) vary over its length. Due to non-slip boundary conditions, the flow velocity is zero for $r=a$ and $r=b$. However, the flow profile in canaliculi levels out already close to the walls of the pericellular space, due to the very high drag from the PCM. Consequently, the ratio between effective permeability and PCM permeability is close to 1 for canaliculi (Weinbaum, Cowin et al. 1994, You, Weinbaum et al. 2004).

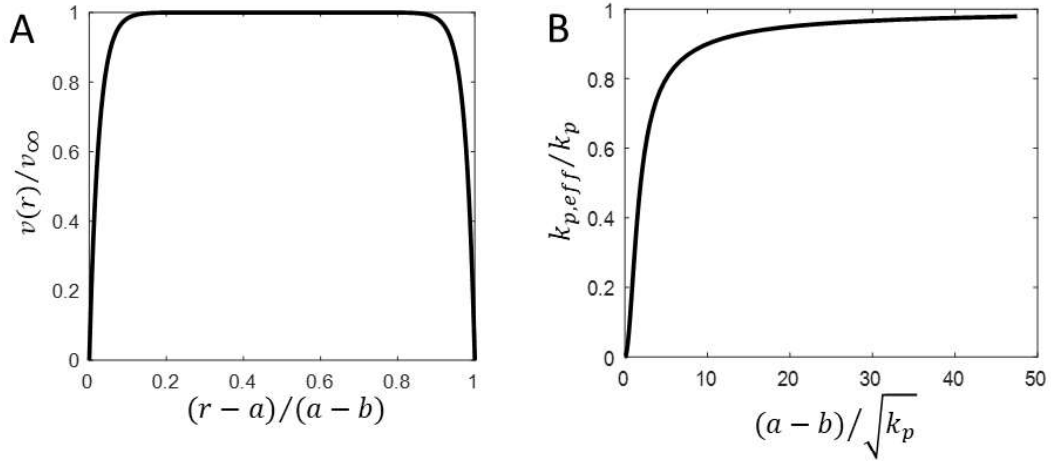


Fig. 1.13. A) A flow profile solution of the Brinkman equation, normalized by the Darcy velocity v_∞ . k_p is the permeability of the PCM only (Weinbaum, Cowin et al. 1994). The no-slip boundary condition force the fluid flow velocity to zero at the walls. Away from the walls the normalized velocity approaches 1, as according to eq. 1.1, the low permeability k_p of the PCM limits the fluid flow velocity here to a maximum of v_∞ . B) The ratio between the effective permeability and the permeability of the PCM $k_{p,eff}/k_p$, calculated using the Brinkman equation, varies with thickness of the pericellular annulus and PCM permeability (Weinbaum, Cowin et al. 1994). In our study the $k_{p,eff}/k_p$ ratio is roughly 0.9.

The effective permeability is relatively insensitive to variations in the diameter of canaliculi and the cell process, as demonstrated by the ratio between the effective permeability and the permeability of the PCM. Fig. 1.13 B shows how this ratio changes with the width of the pericellular annulus normalized by the square root of the permeability, i.e. $(b - a)/\sqrt{k_p}$.

The number of studies which focus on the interaction between the fibrous pericellular matrix and the interstitial fluid movement at the canaliculus scale is very limited (Beno, Yoon et al. 2006,

1. Introduction

Lemaire, Naili et al. 2008). Although all studies agree that the pericellular matrix reduces the permeability considerably, there is still an uncertainty in the actual value of the permeability of several orders of magnitude (Beno, Yoon et al. 2006). Estimating the permeability becomes even more challenging when the role of osmotic and electro-osmotic effects would be taken into account (Lemaire, Naili et al. 2008).

2. METHODS – MULTISCALE CHARACTERIZATION OF BONE

Fundamental for a successful execution of the thesis project, was a combination of experimental and computational methods is important. My contribution to the methodological part of the project was the development of a mathematical model to predict the impact of the osteocyte LCN architecture the fluid flow through the canaliculi, and consequently, on the remodeling response of bone to changing mechanical loads. Before I developed this model, I experimentally imaged the LCN of human and mouse bones to feed my model with real LCN architectures. This was done with the help of previously developed software TINA (Tool for Image and Network Analysis) (Kollmannsberger, Kerschnitzki et al. 2017, Repp, Kollmannsberger et al. 2017, Weinkamer, Kollmannsberger et al. 2019). This chapter focuses on the experimental part of my study and the following chapter presents the developed model.

2.1. *In vivo* Loading Combined with 3D Morphometry of the Mechanoreponse

The provided mouse tibiae by the group of Bettina Willie (McGill University, Montreal, Canada) were very valuable, because these bones underwent a well-established loading protocol and were thoroughly characterized. Non-invasive loading of bones in living animals is an excellent strategy to study the mechanoreponse of bones. In our project the mouse bones were loaded following a well-defined loading waveform (Willie, Birkhold et al. 2013, Birkhold, Razi et al. 2014). Previously, the controlled dynamic loading experiment was calibrated experimentally in similar mice (26 weeks old female C57Bl/6), using strain gauges *in vivo* on the medial surface of the left tibial midshaft. Based on this calibration a cyclic load with a peak force of 11 N was applied to the left tibia to reach a peak strain of +1200 $\mu\epsilon$ (Fig. 2.1 A) (Main, Lynch et al. 2010, Willie, Birkhold et al. 2013). Note that strain is positive at this site, as this is the stretching side of the bending bone. To control the strain rate in both loading and unloading a symmetric triangular waveform was applied, with a constant strain rate during the 0.075 second long loading and unloading ramps of the waveform. The left tibiae received 216 cycles at 4 Hz on each working day for two weeks, as shown in the schedule in Fig. 2.1. A. The developers of this method recently wrote a detailed review about different *in vivo* loading protocols, the key parameters and calibration (Main, Shefelbine et al. 2020).

In vivo μ CT scans of a little over 2 mm of the tibial midshaft (Fig. 2.1. B) were performed at an isotropic voxel size of 10.5 μm on day 0, 5, 10 and 15. These scans were then used to create a time-lapse of the bone (re)modelling process (Birkhold, Razi et al. 2014). Mice were anesthetized and fixed in a special holder to prevent motion artefacts and optimize the repeatability of the imaging location. The scans from different time points of the same mouse were then segmented and analyzed to quantify structural changes over the time between two images. In short, the

analysis protocol is done in three steps. Step 1) A time lapse of *in vivo* μ CT datasets from one mouse was registered using rigid transformations (i.e. only translation and rotation, no scaling). Raw gray scale images were used for the registration in ZIBAmira software (Zuse Institute, Berlin, Germany) with “normalized mutual information” as similarity criterium (Birkhold, Razi et al. 2014). Step 2) The coordinate systems of all scans were transformed to one single coordinate system using Lanczos interpolation, to give all datasets the same voxel size and coordinate system (Birkhold, Razi et al. 2014). I also transformed our own high resolution *ex vivo* μ CT scans into this same common coordinate system as the *in vivo* μ CT scans (Fig. 2.1 B). Step 3) The registered *in vivo* CT images were segmented, to define which voxels were part of the mineralized bone (0 = no bone, 1 = bone). Finally, the images were cut to 5% of the total tibial length to remove the parts where, due to variability in the placement of the animals in the μ CT scanner, the *in vivo* μ CT scans of the different time points did not overlap. Identification of voxels with newly formed, resorbed and quiescent bone was done by comparing the segmented images of the same tibia at the different time points: Newly formed bone = from 0 to 1 between the earlier and the later μ CT scan, resorbed bone = from 1 to 0, and quiescent bone = 1 in both time points (Birkhold, Razi et al. 2014). See Fig. 2.1 E for a 3D render of such a dataset.

2.2 Finite Element Modeling

Previously Willie, Birkhold et al. (2013) used a high resolution μ CT scan of one of the whole tibia from the calibration study for a finite element model (FEM) to estimate the stress and strain distributions. Boundary conditions of the model were set to mimic the experimental *in vivo* loading (Fig. 2.1 C). The load of 11 N was applied to the nodes of the proximal tibial plateau (i.e. the knee) while axial movement of reference nodes at the surface of the ankle were restrained. The elastic modulus of the elements was based on the tissue mineral density, since the mechanical properties of bone depend on the degree of mineralization (Taddei, Schileo et al. 2007, Willie, Birkhold et al. 2013). The simulated results were compared to the experimental strain measurements to calibrate the model. The mesh with the stress and strain tensors of each element from this study were then provided to us, from which we calculated the local dynamic mechanical load. Measured remodeling, in terms of formation and resorption, are correlated with the local surface strain in order to predict the mechanoreponse of the tibiae. In my study I also use the local strain to calculate the load induced fluid flow, which is then used to predict the remodeling (described later, in chapter 3).

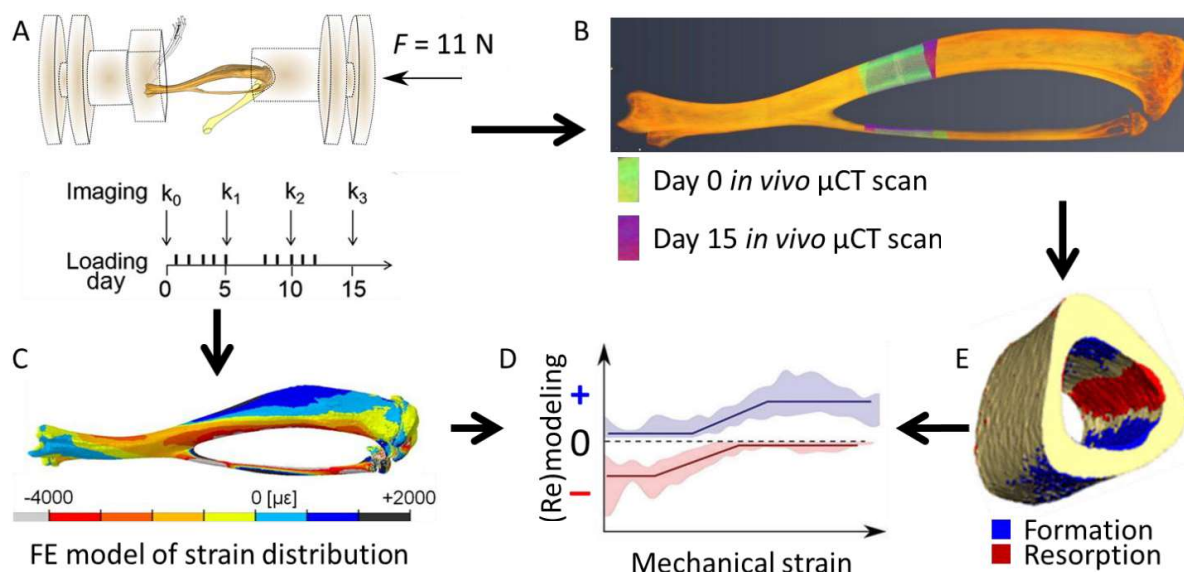


Fig. 2.1. Experimental mouse model to measure the mechanoreponse of bone to increased loading conditions. A) The setup which was used to dynamically load the hind limbs of the mice (tibiae) five times per week for two weeks, as indicated in the schedule. *In vivo* μ CT scans were taken on imaging days, indicated with k_0 to k_3 . B) An indication of the region where *in vivo* μ CT time-lapse scans were made. C) The strain distribution during the loading experiment, calculated with a previously developed and calibrated Finite Element (FE) model (Razi, Birkhold et al. 2015). E) The (re)modelling (i.e. bone formation and resorption history), which is calculated from the difference between the *in vivo* μ CT scans of day 0 and day 15. D) In a previous study this information was combined to quantify the mechanoreponse of a tibia (Razi, Birkhold et al. 2015). The probability to find formation (blue) at a given site on the bone surface increases with local strain at that site, while the probability to find resorption (red) decreases with strain.

2.3. Sample Preparation and Rhodamine Staining

In the mouse project, the joints of the mouse tibiae were removed to provide better access to the bone porosity for optimal rhodamine staining. For the human osteon study, a sample from a femur midshaft of a 57 year old woman without any known bone-related disease was provided by the Department of Forensic Medicine and the Department of Anatomy of the Medical University of Vienna. The human bone was stored at -20°C immediately after the necropsy. After unfreezing, the samples were cleaned from soft tissue and a 1 cm thick piece of the diaphysis was cut perpendicular to the long axis of the bone. The lateral part of the cortex was then provided for our study.

Rhodamine was used for the staining of the LCN of all bone samples, based on a well-established protocol (Kerschnitzki, Wagermaier et al. 2011). The ethanol dehydration series was performed with small steps (80 %, 90%, 95%, 100% 24h per step), to minimize the formation of cracks due

to shrinkage of the bone. Although we limited the rate of shrinkage, we were not able to fully prevent it. This is probably one of the reasons that some of the bones were damaged, which showed up as plane like structures in the 3D confocal images of the rhodamine stained bone. After dehydration the bone was not exposed to water anymore to prevent modification of the bone mineral and, therefore, we used a rhodamine-6G solution in 100% ethanol (0.02% wt) to stain the LCN. The samples were submerged twice in fresh rhodamine solution under constant motion for 24 hours. The staining solution was then replaced by methyl methacrylate (MMA) infiltration solution. The bone samples were placed in cylindrical acrylic sample holders filled with fluid MMA (Fig. 2.2 A), which was polymerized under high temperature.

Since a smooth surface is needed for high quality imaging of the LCN, the embedded samples were cut in sections with parallel surfaces followed by grinding with a succession of different grades of abrasive paper. Finally, the samples were polished using diamond powder (Kerschnitzki, Wagermaier et al. 2011). For the mouse tibiae, exceptional care was taken to expose a surface in exactly the same region as where the *in vivo* μ CT scans were taken (Fig. 2.1 B). A sub-millimeter precision is already needed to cut the 1.8 mm thick region of interest roughly in the middle. Not just the small size, but also the bending of the light due to the curvature of the cylindrical PMMA block, make it nearly impossible to eyeball the position of the cut. Therefore, we exploited augmented reality using a 3D model of the bone in the PMMA block. A photograph of all embedded bone samples was taken at a defined height to function as the ‘reality part’ of our augmented reality approach. In this photo the cylinders with the bone samples were placed upside-down, with the flat side facing the camera, in order to have minimal distortion (Fig. 2.2 B). The photograph was then calibrated using the known camera distance and the dimensions of the cylinders. The high resolution μ CT scans of the bones were placed in roughly the correct position in the same coordinate system as the photo, based on measurements with a ruler, for the augmented reality visualization in ZIBAmira (Zuse Institute, Berlin, Germany). Small adjustments (i.e. translations and rotations) were then done manually in Amira, until the μ CT scan and photographed tibiae overlapped as good as possible (Fig. 2.2 A). The high resolution μ CT scans were then replaced with the *in vivo* μ CT scans, to visualize the position of the regions of interest on the PMMA blocks. A fine marker was then used to draw the cutting plane on the PMMA block. The blocks were then cut with a 50 μ m thick diamond wire in a precision cutting machine equipped with a simple microscope (Fig. 2.2 C). Carpenters wax was used to stick the PMMA block to the flat surface of the sample holder (Fig. 2.2. C). The position of the block in the machine was precisely set up using one translational and three rotational micro-positioners. A second cut was made outside each side of the region of interest to create two blocks with parallel surfaces.

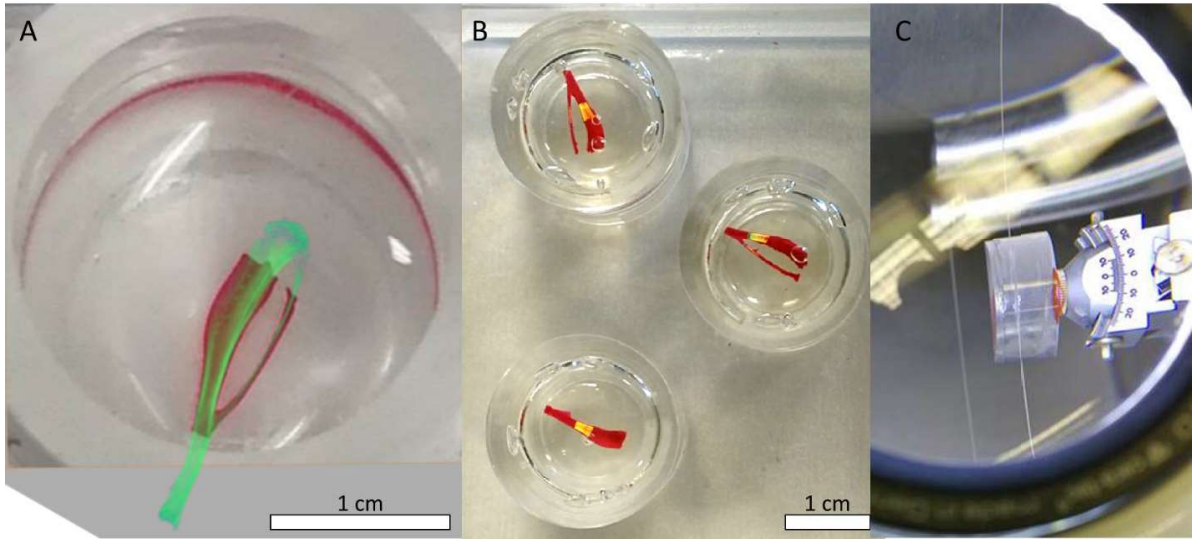


Fig. 2.2. Embedding and cutting of the bone samples. A) Augmented reality was used to combine μ CT scans of the tibiae (computer rendered in green) with photos of the tibiae (stained red) embedded in cylindrical PMMA blocks. The joints of the real bone were removed to allow faster penetration of the rhodamine. B) The *in vivo* μ CT time-lapse scans (yellow) rendered in 3D on the photographs of the samples within the blocks. These computer images were used to precisely plan the cuts in the middle of the regions of interest. C) A PMMA block in the precision cutting machine with a 50 μ m thick diamond coated wire saw, photographed through the simple microscope of the machine. The micro positioners (one translation axis and three axis of rotation) allow to accurately position the block in the machine. Red wax, used to mount the sample, is visible between the sample holder and the PMMA block.

2.4. Confocal Laser Scanning Microscopy

A Leica TCS SP5 Confocal laser scanning microscope (CLSM) (Wetzlar, Germany), equipped with a 40x oil-immersion lens with a numerical aperture $NA = 1.25$ (Leica, HCX PL APO 40x NA 1.25 OIL) was used to image the 3D LCN of the osteons, with an excitation wavelength of 543 nm (HeNe-laser). No glass cover slip was used, i.e. the lens was directly used on the PMMA block with Leica immersion oil. For the study on the LCN of the mouse tibiae, measurements were performed using a new microscope, the Leica TCS SP8 (Wetzlar, Germany), equipped with a 40x oil-immersion lens with a numerical aperture $NA = 1.3$ (Leica, HC PL APO CS2 40x/1.30 OIL) with an excitation wavelength of 514 nm (Argon laser). The fluorescence signal was measured between 553 and 700 nm with an Airy 1 pinhole size of 68 μ m. Since I observed that the new Leica lens oil caused cracks to form in the PMMA block, diethylene glycol between the PMMA block and the glass cover slip was used instead. Simply leaving the oil out would not work, as the function of this oil is to limit the differences in refractive index in the optical pathway between the lens and the sample. To not contaminate the lens, we used Leica immersion oil between the lens and the glass cover slip. Visual inspection did not reveal any differences in imaging quality between immersion oil and diethylene glycol.

In human bone the imaged volume of a single CLSM image stack was approximately $300 \times 300 \times 40 \mu\text{m}^3$ with an isotropic imaging resolution of 300 nm. This field of view can capture a whole cross section of an osteon. The lower value of the imaging depth is due to the limited transparency of mineralized bone. The optical properties of mouse bone are slightly better, which allowed for better imaging depth. For mouse bone a single CLSM image stack is roughly $390 \times 390 \times 50 \mu\text{m}^3$ with a resolution of $0.38 \times 0.38 \times 0.34 \mu\text{m}^3$. The image resolutions used for mouse and human bone do not allow resolving the actual diameter of the canaliculi. However, the detection of canaliculi was sufficient for an accurate representation of the network topology, since distances between canaliculi are larger than the resolution (Kerschnitzki, Wagermaier et al. 2011, Milovanovic, Zimmermann et al. 2013). An advantage of the lower resolution used for the mouse bone is that the field of view is larger. With this field of view the full cross section of all the mouse tibiae, which is roughly up to $1200 \mu\text{m}$ wide, could be covered with 16 images, in a 4×4 grid (Fig. 2.3 A). Imaging of the whole cross section takes between 2 to 3 hours. A 10% overlap was not only introduced to allow stitching of the canaliculi (Fig. 2.3 B, C), but it also allows for some movement of the sample. One should note that the sample is not fixed rigidly, but is floating on immersion fluid. Additionally, drift within the positioning system is common during these long imaging times. For the same reason extra images were taken above and below the sample, to allow for positioning errors in the depth axis (z-axis). These extra images were removed after stitching.

The images were not well-stitched by the LAS X software of the microscope (Leica Application Suite X, Leica Microsystems). Connecting corresponding canaliculi between overlapping image stacks is essential for the fluid flow calculations. Therefore the images were carefully stitched using BigStitcher in ImageJ (Hörl, Rusak et al. 2018). Bone surfaces, vascular canals and bone marrow dominate the stitching procedure due to the large volumes and bright intensity of these features. Stitching using these features helps to make a good initial alignment, but further refinement is needed as corresponding canaliculi do not match up yet (Fig. 2.3 B). Therefore, images only containing segmented canaliculi were produced by using the difference of gaussians method (see details in the image processing section). A first refinement step with only rigid transformations increased the alignment of canaliculi considerably. A final refinement step was made by allowing a 1% deformation in an affine transformation (Fig. 2.3 C). The affine transformation matrices resulting from the segmented canaliculi were then used to stitch the raw confocal microscopy stacks. The confocal microscopy measurements of mouse #2 and #3 were redone, since image deformations much larger than 1% had to be used in order to connect the canaliculi of different stacks. This shows that care should be taken to minimize the amount of movement around the microscope during long measurements.

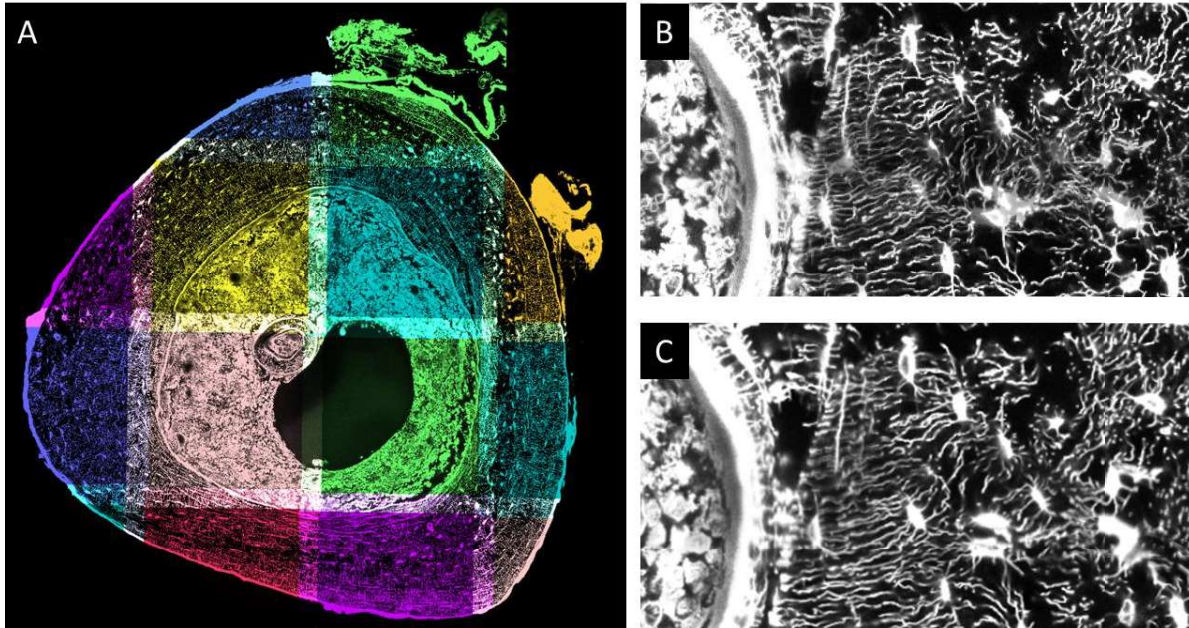


Fig. 2.3. A) Several 3D image stacks are stitched to cover the full tibia cross section, since the field of view ($\sim 350\ \mu\text{m}$) is smaller than the cross sectional diameter of the mouse tibiae ($> 1\ \text{mm}$). A random coloring of the images demonstrates the 4 by 4 grid with 10% overlapping area at the borders. B) An illustration of the first step of registration, where the raw intensities were used to line up the image stacks. The overall shape of the cortex seems well aligned. The small canaliculi, and even lacunae, are not easy to align, due to image artefacts caused by the common small movements that happen during the hours long measurements. In the middle of the image, from left to right, a band with misaligned LCN is visible. C) The same region as in (B) after several refining steps of the registration. Processed images with only canaliculi were used for the latest refinements and therefore connectivity of the canaliculi could mostly be reestablished. Note that the connectivity of the network is important in this study, as it strongly influences the calculated fluid flow patterns.

Although the study started with six individual mice, we ended up only three usable samples. Three of the loaded tibiae were excluded as they showed plane like structures in the 3D CLSM images, which are probably due to cracks that formed during sample preparation. These cracks were also visible in some of the right tibiae (Fig. 2.4 A) and therefore, are not due to the *in vivo* loading. Two of the CLSM images were taken again due to later discovered sample motion during the first measurement. Large movement results in artefacts as illustrated in Fig. 2.4 B, while small movements lead to disconnected canaliculi in the stitched images. Due to the large volumes of interest, the CLSM imaging takes several hours per sample. Since the sample is not rigidly fixed during imaging, but floats on a thin layer of oil, the sample can easily move. An important part of the experimental methods is therefore to limit movement around the microscope.

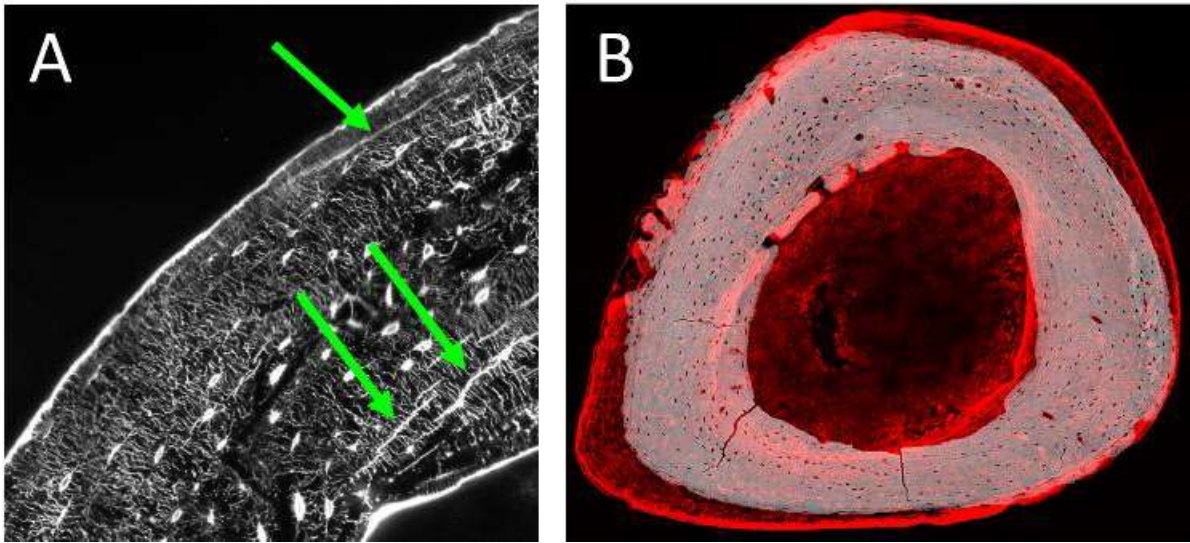


Fig. 2.4. Sample preparation and imaging artefacts. A) One 2D slice from a CLSM image, showing plane like structures (marked with arrows) which are likely cracks which formed during sample preparation. B) A CLSM image (shown in red) overlaid on an electron microscope image (shown in grey) of the same surface. The difference in shape could be due to sample movement during microscopy.

3. MODEL DEVELOPMENT – MECHANOSENSING VIA LOAD-INDUCED FLUID FLOW

As of now, the understanding of how mechanical signals are translated to biological signals is limited. No model can explain the experimental results, which show a wide local variation in how strongly bone responds to mechanical stimulation. I assumed that we require three pieces of information to predict how mechanical loads at the bone scale are translated via load-induced fluid flow to mechanical stimuli at the cellular scale:

- 1) How easy is it for the fluid to flow through single canaliculi, i.e., what is the relationship between flow and pressure gradient within a canaliculus.
- 2) How the canaliculi are connected to each other, the lacunae, the vascular canals and the bone surface.
- 3) Where the fluid is coming from and where it is flowing to. This includes coupling between the mechanical environment and the LCN pore volume.

The first three sections of this chapter will cover these three points. The last section of this chapter covers the actual biological response, i.e. the (re)modeling response of the bone.

3.1 Fluid Flow in Single Canaliculi

The relationship between fluid flow and pressure gradient can be modeled using Darcy's law:

$$q_j = -\frac{k_{p,eff}}{\mu} \cdot \nabla_j P \cdot A, \quad (3.1)$$

Where q_j denotes the volumetric fluid flow through canaliculus j , i.e. the volume of fluid transported through the canaliculus per unit of time. $\nabla_j P$ denotes the pressure gradient in the axial direction of the canaliculus and μ denotes viscosity of the interstitial bone fluid. The estimation of the cross-sectional area A has to consider that the bone fluid can flow only in the annulus between the cell processes of the osteocytes and the canalicular wall. The osteocytes probably sense shear forces on the surfaces of their cell processes, rather than volumetric fluid flow rates through their canaliculi or fluid pressures. The average velocity of the fluid in the canaliculus, \bar{v}_j , is therefore calculated:

$$\bar{v}_j = \frac{q_j}{A} = -\frac{k_{p,eff}}{\mu} \frac{\Delta P}{l_j}. \quad (3.2)$$

3. Model Development – Mechanosensing via Load-Induced Fluid Flow

Assuming a no-slip boundary condition, the shear stress, τ , on the cell process membrane can be obtained from the velocity gradient at the cell membrane as given by (Weinbaum, Cowin et al. 1994, You, Cowin et al. 2001),

$$\tau = \mu \left. \frac{\partial v(r)}{\partial r} \right|_{r=CP,Rd} = \mu \cdot K \cdot \bar{v}, \quad (3.3)$$

where $v(r)$ denotes the cylindrically symmetric velocity profile in the annulus region between cell process and canaliculus wall. This region is not an empty space, but a fiber matrix exists within the annular region between the osteocyte process and the canaliculus wall consisting predominantly of proteoglycans which strongly influence the permeability of canaliculi (Tsay and Weinbaum 1991, Thompson, Modla et al. 2011, Sansalone, Kaiser et al. 2013, Cowin and Cardoso 2015, Wijeratne, Martinez et al. 2016). To estimate the effective permeability, $k_{p,eff}$, we follow the approach by Weinbaum and co-workers (1994) in taking into account the pericellular matrix (see also section 1.3.5). Assuming a two-dimensional square array of fibers an expression can be obtained which includes only the fiber radius and the fiber spacing as geometric parameters (Tsay and Weinbaum 1991). Secondly, homogenization results in a Brinkman equation, which is solved with no-slip boundary conditions at the canaliculus wall and the surface of the osteocyte process. The resulting numerical value for $k_{p,eff}$ and all other model parameters are summarized in Table 3.1.

Table 3.1. Numerical values of model parameters

<i>Parameter</i>	<i>Value</i>	<i>Description</i>
μ	$1.06 \cdot 10^{-3} \text{ Pa} \cdot \text{s}$	viscosity of the bone fluid (Cardoso, Fritton et al. 2013)
Ca, Rd	157.5 nm	radius of the canaliculus (Varga, Hesse et al. 2015)
CP, Rd	73 nm	radius of the osteocyte process (Buenzli and Sims 2015)
A	$0.061 \text{ } \mu\text{m}^2$	annular cross section between canaliculus and osteocyte process calculated as: $A = (Ca, Rd^2 - CP, Rd^2)\pi$
$k_{p,eff}$	$1.53 \cdot 10^{-17} \text{ m}^2$	permeability of a canaliculus (Weinbaum, Cowin et al. 1994)
K	$465 \text{ } \mu\text{m}^{-1}$	shear stress constant (Weinbaum, Cowin et al. 1994)
$\dot{\epsilon}$	0.015 s^{-1}	volumetric strain rate value corresponds to peak strain rate during exercise (Lanyon, Hampson et al. 1975, Milgrom, Finestone et al. 2002, Al Nazer, Lanovaz et al. 2012)
V_i^{lacuna}	$350 \text{ } \mu\text{m}^3$	lacunar volume (Carter, Thomas et al. 2013, Dong, Hauptert et al. 2014)

3.2 Fluid Flow Through Networks

In this section we cover point 2; the connectivity of the LCN, the vascular canals and the bone surface. The advantage of using a network description (often referred to as graphs by mathematicians) is that linear algebra can be applied to the matrices that describe the network (Grady and Polimeni 2010). We can for example show which node is connected to which other nodes in the commonly used adjacency matrix \mathbf{M} , where the value of M_{ij} is 1 if node i connects to node j and 0 otherwise. The big disadvantage of \mathbf{M} is that it cannot describe parallel edges between the same node pair, which are common in the LCN. The incidence matrix \mathbf{A} , is one of the methods to store the relations between all the edges and nodes in a network, including parallel edges. The value of A_{ij} is 1 if edge j points to node i , -1 if edge j points away from node i , and is zero otherwise.

$$A_{ji} = \begin{cases} 1 & \text{if edge } j \text{ points towards node } i \\ -1 & \text{if edge } j \text{ points away from node } i, \\ 0 & \text{if edge } j \text{ is not connected to node } i \end{cases} \quad (3.4)$$

This matrix can be used to calculate the pressure difference over an edge and the volumetric flow through this edge:

$$\mathbf{A}^T \mathbf{P} = -\Delta \mathbf{P}, \quad (3.5)$$

The pressure gradient can then be combined with the pressure-flow relationship from the previous section by introducing a conductivity matrix \mathbf{C} . The elements in the diagonal conductivity matrix \mathbf{C} are obtained by assessing the fluid flow within a single canaliculus, corresponding to Darcy's law (Eq. 3.1):

$$C_{jj} = \frac{q_j}{-\Delta P_j} = \frac{k_{p,\text{eff}} A}{\mu l_j}, \quad (3.6)$$

with $k_{p,\text{eff}}$ the effective permeability, A the cross sectional area of the annulus of the canaliculus, μ the viscosity of the interstitial fluid and l_j the length of the canaliculus.

$$\mathbf{q} = -\mathbf{C} \Delta \mathbf{P} = \mathbf{C} \mathbf{A}^T \mathbf{P} \quad (3.7)$$

The example network of Fig. 3.1 B consisting only of four nodes and five edges is used to illustrate how this incidence matrix can be used in combination with linear algebra, to calculate the fluid pressure and flow patterns in the LCN. The 4×5 incidence matrix of the example network (Fig. 3.1 A) is given by:

$$\mathbf{A} = \begin{bmatrix} -1 & -1 & 0 & 0 & 0 \\ 0 & 1 & -1 & 0 & -1 \\ 1 & 0 & 1 & -1 & 0 \\ 0 & 0 & 0 & 1 & 1 \end{bmatrix}$$

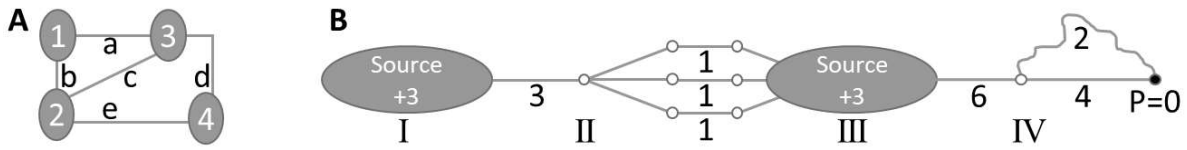


Fig. 3.1. Illustration of preservation of mass assumption in fluid filled networks. A) The preservation of mass is the basis of Kirchhoff's second law, which is used to calculate the flow and pressure in each edge and node, respectively. To demonstrate how Kirchhoff's law can be used with linear algebra we introduced an example of a simple network with edges indicated by letters and nodes indicated by numbers. B) In our model the amount of fluid per unit of time which is pushed out of the LCN during compression of the bone has to travel through the canaliculi and is therefore strongly affected by LCN architecture. (I) For demonstration only, we assume that compression of the first lacuna generates a flow of 3 in this simplified network, and we assume that the compression of canaliculi doesn't contribute to the fluid displacement. (II) The flow of 3 is divided when the first single canaliculus splits into three canaliculi downstream, resulting in 3 times a flow of 1. This is in agreement with the preservation of mass, as inflow minus outflow is equal to zero. (III) The total inflow in this lacuna is 3, the contribution of the lacuna is +3, therefore, the outflow is 6, which is again in agreement with the preservation of mass (i.e. the sum is zero). (IV) Not all canaliculi have the same permeability though, and fluid flow mostly takes the path of least resistance (i.e. highest permeability). Most of the flow goes therefore via the shorter canaliculus, as shorter canaliculi have a higher permeability. In this example the longer canaliculus is double the length of the shorter one. Therefore permeability and fluid flow velocity in the long canaliculus are half compared to in the short canaliculus. Finally, the fluid is drained into the low pressure reservoir ($P = 0$).

With the incidence matrix of our example Eq. 3.5 evaluates to:

$$-\Delta \mathbf{P} = \mathbf{A}^T \mathbf{P} = [P_3 - P_1, \quad P_2 - P_1, \quad P_3 - P_2, \quad P_4 - P_3, \quad P_4 - P_2]^T$$

When we check for example edge a, then we see indeed that the pressure difference over this edge is the pressure in node 3 minus the pressure in node 1 ($P_3 - P_1$). Note that the sign of ΔP_j depends on the direction of edge j . We can use another matrix multiplication to calculate the volumetric fluid flow (i.e. volume of fluid passing through the edge per unit of time) from the pressure differences and the conductivity of the edges:

$$\mathbf{q} = -\mathbf{C} \Delta \mathbf{P} = [C_a(P_3 - P_1), \quad C_b(P_2 - P_1), \quad C_c(P_3 - P_2), \quad C_d(P_4 - P_3), \quad C_e(P_4 - P_2)]^T$$

We see indeed that the flow through edge b is the pressure difference over edge b times the conductivity of edge b . However, the values of \mathbf{P} are unknown, and need to be solved using Kirchhoff's current law. Based on the preservation of mass, we define the sum of flows in one node should be zero. We can again use the definition of the incidence matrix \mathbf{A} , to or from which nodes the edges are pointing, to calculate the sum of volumetric in and out flow per node:

$$\mathbf{ACA}^T \mathbf{P} + \mathbf{f} = -\mathbf{LP} + \mathbf{f} = 0, \quad (3.8)$$

where the vector \mathbf{f} describes the load-induced volume change rates of all the nodes (point 3, see next section). To solve \mathbf{P} we simplified the equation using the following definition of the weighted Laplacian matrix \mathbf{L} , which is a commonly used matrix in circuit theory (Grady and Polimeni 2010).

$$\mathbf{L} = -\mathbf{ACA}^T \quad (3.9)$$

Since we now know \mathbf{L} and \mathbf{f} , it seems that we can calculate the node pressures \mathbf{P} by solving equation 3.8. In our example network we would have to solve the following set of linear equations:

$$\mathbf{ACA}^T \mathbf{P} = -\mathbf{LP} = \begin{bmatrix} (C_a + C_b)P_1 - C_bP_2 - C_aP_3 \\ (C_b + C_c + C_e)P_2 - C_bP_1 - C_cP_3 - C_eP_4 \\ (C_a + C_c + C_d)P_3 - C_aP_1 - C_cP_2 - C_dP_4 \\ (C_d + C_e)P_4 - C_eP_2 - C_dP_3 \end{bmatrix} + \mathbf{f} = 0$$

However, due to the symmetry of \mathbf{L} a problem arises, resulting in a singular matrix. Singular matrices cannot be inverted. When having a closer look at the example we see that the absolute pressures cannot be solved, as only pressure differences are needed to calculate the fluid flow through each edge. This problem can be solved by assigning a reference node i . For electrical networks it is common practice to set this reference as 0 (i.e. defining a 'ground' node). We therefore define a new nonsymmetric reduced Laplacian matrix \mathbf{L}_0 as \mathbf{L} with the i -th row and i -th edge removed. Equation 3.8 can be solved via the inverse of \mathbf{L}_0 (Grady and Polimeni 2010, Newman 2010), however, this is not recommended as this results in a full matrix with $N \times N$ elements, where N is the number of nodes. Instead, we can make use of sparse matrices, if we define a reduced load-induced flow vector \mathbf{f}_0 by removing the i -th element from \mathbf{f} . The use of sparse matrices proves advantageous in equation solving, as it is fast and not as memory expensive. Pressures can then be calculated by solving the following reduced equation:

$$\mathbf{L}_0 \mathbf{P}_0 = \mathbf{f}_0 \quad (3.10)$$

Finally, the reference pressure ($P_i = 0$) and the reduced pressure vector \mathbf{P}_0 are combined to get the full pressure vector \mathbf{P} .

In our study all circuit theory calculations were performed using Scipy 0.15.1 and Numpy 1.17.4 in Python 3.7 (<http://python.org>). The matrices **A** and **L** were constructed from the TINA networks using NetworkX 1.11. Employing the SciPy 1.3.2 sparse matrix methods, in combination with rearranging the node indices with the reverse Cuthill-McKee algorithm (Cuthill and McKee 1969), allowed the calculation of the pressure patterns within a whole osteon with 40 μm thickness within a couple of seconds. The original version of TINA (<https://bitbucket.org/refelix/tina/>) was running in Python 2.7 and was using 32 bit software. Due to the limited 32 bit memory address space this version could not be used with the very large CLSM datasets of the mouse tibiae. Therefore, I updated TINA to work in Python 3.7, which could deal with the over 200 GB of memory which was needed to run the analysis. TINA was not speed optimized, hence the analysis took over 12 hours per dataset. Python code runs slowly, as it is not compiled. This limitation of Python was overcome by strategically compiling parts of the code using a Just-In-Time compiler library (NUMBA 0.45, <http://numba.pydata.org>). I took special care to preserve the core functionality of TINA. Therefore, results do not depend on the used version of TINA.

3.3. Boundary Conditions in the Network Model

The information of point 3 is used to define the boundary conditions of our model: Where is the fluid coming from and where does it flow to? To calculate this, we use the Laplacian matrix **L**, which combines the information of permeability (section 3.1) and the measured network architecture (section 3.2). Fig. 3.1 B illustrates how all three pieces of information (i.e. permeability of canaliculi, connectivity and boundary conditions) are combined in the developed network model. We assume that under compression a fraction of the fluid is forced out from each component of the LCN, due to the decrease in pore volume. This fluid is going to the low pressure reservoirs: the Haversian canal in osteons or the surfaces of the bone and vascular canals in the mouse tibiae. We defined a reference node which links all the places where fluid flows to. The role of the reference node (Eq. 3.10) was taken over by a special node of the network i_0 . During loading cycles, the pressure in the vascular porosity will remain constant. For simplicity we defined the reference pressure as 0 kPa. In the case of tension, the flow reverses, as fluid has to flow from the reference node into the LCN due to the increase in pore volume.

Strain rate is likely the main contributor to fluid flow velocity in the LCN (Remond, Naili et al. 2008, Goulet, Coombe et al. 2009, Wu, Wang et al. 2016). Under dynamic loading the bone – and with the bone the LCN – is deformed at a certain strain rate. The deformation is assumed to be homogeneous throughout the bone and its LCN porosity. The pericellular space between osteocyte and ECM is assumed to be filled with incompressible fluid. Therefore, the reduction of the porosity volume squeezes the fluid towards the openings of low pressure, i.e. towards node i_0 . Both lacunae

and canaliculi have fluid-filled pore volumes, which contribute to the load-induced fluid flow. In the language of the used model each node in the network acts as a source of fluid, where the value of \mathbf{f} depends on the volumetric strain rate $\dot{\epsilon}$ and the volume of the node. A canaliculus is always shared between two nodes, thus the node volume is calculated as half the volume of the canaliculi connecting to the node. In case the node represents an osteocyte lacuna a constant lacunar volume V_i^{lacuna} is added.

For the simulations presented in the following, the osteon and its LCN are viewed as a sealed off building block of cortical bone due to the virtually impermeable cement line, while the mouse tibiae have open endocortical and periosteal surfaces. Canaliculi stop at the cement line and thus, constitute a dead end for the fluid flow in our model.

$$\mathbf{f} = \begin{cases} -\dot{V}^{OLCN} & \text{For reference node } i_0 \\ +\dot{\epsilon}_i \cdot \left(\frac{deg_i}{2} \cdot A + V_i^{lacuna} \right) & \text{for all lacunae} \\ +\dot{\epsilon}_i \cdot \frac{deg_i}{2} \cdot A & \text{for all other nodes} \end{cases} \quad (3.11)$$

where deg_i is the weighted node degree, i.e. the sum over the length of all canaliculi connecting to node i (Schult and Swart 2008). The bone fluid volume that is squeezed into the reference node per unit of time, \dot{V}^{OLCN} , is given by the condition that the sum over \mathbf{f} has to be zero to comply with the preservation of fluid mass.

For human osteons the value for the strain rate $\dot{\epsilon}$ was chosen following experiments with strain gauges on the surface of the human tibia (Al Nazer, Lanovaz et al. 2012). Peak strain rates that occur during intensive exercise were chosen, as intensive exercise most likely causes a mechanoreponse of the bone. For the mouse model Razi, Birkhold et al. (2015) developed a Finite Element Model (FEM), based on a high resolution ex vivo μ CT scan and the experimental in vivo loading conditions, to calculate the strain distributions of the whole mouse tibiae. The full peak strain tensors from this model (ϵ), combined with the dynamic loading waveform, were used to calculate the local volumetric strain rates in each element:

$$\dot{\epsilon}^{element} = \frac{d}{dt} \frac{\Delta V^{element}}{V_0^{element}} \approx \pm \frac{\epsilon_{xx}^{element} + \epsilon_{yy}^{element} + \epsilon_{zz}^{element}}{\Delta t},$$

where $\Delta V^{element}$ is the volume change of the finite element, and $V_0^{element}$ is the resting volume of the finite element. Since the waveform of the applied load was triangular, we can assume that the strain rate is constant during the time Δt the load is increasing. The sign is positive during compression and negative during relaxation, causing the fluid to flow back and forward in the canaliculi. Since the tibia undergoes bending, the anterior part is under tension (positive strain), while the posterior part gets compressed. Coordinate systems of the FEM mesh and the LCN were

matched by registering the FEM mesh with the *in vivo* μ CT data of day 0. An initial guess of the correct position was made by hand, after which the rigid transformation used for this registration was fine-tuned by minimization of the sum of distances between the surface nodes of the FEM mesh and the segmented surface of the *in vivo* μ CT (Fig. 2.1). Nearest neighbor interpolation was then used to assign the node strains ($\dot{\epsilon}_i$).

Finally, we investigated the impact of our idealized model by testing the robustness of our model using the networks of two different human osteons. The assumption that the cement line is an impermeable boundary neglects the small number of canaliculi which penetrate the cement line. To study the sensitivity of the model to a leaking cement line, a total leakage flow was added to the volumetric fluid flow sources \mathbf{f}_{leak} (i.e. adapting eq. 3.11) of only the cement line nodes:

$$f_{\text{leak},i} = f_i + \frac{\text{total cement line leakage}}{\text{number of cement line nodes}} \quad (3.12)$$

The second tested assumption is the combination of incompressibility of the fluid and the uniform local volumetric strain. To consider compressibility, the volumetric fluid flow sources of the osteons were limited by utilizing Norton's equivalent circuit of a non-ideal current source (Johnson 2003). In the fluid flow equivalent of a Norton source the fluid flow is limited as the pressure reaches a defined saturation pressure P_{max} . This simulates that fluid under high pressure the fluid is compressed, which limits the flow. Limiting conductors with conductivity C_{lim} were introduced in the networks, parallel to the ideal fluid flow sources (f_i in eq. 3.11).

$$C_{\text{lim},i} = \frac{f_i}{P_{\text{max}}}. \quad (3.13)$$

When the fluid pressure p_i reaches p_{max} there is exclusively compression of the fluid, i.e. the limited volumetric fluid flow goes to zero.

$$f_{\text{lim},i} = f_i - P_i * C_{\text{lim},i} = f_i \left(1 - \frac{P_i}{P_{\text{max}}}\right) \quad (3.14)$$

3.4. Prediction of the Bone Mechanoresponse

It has been experimentally shown that osteocytes are very sensitive to the shear force on their cell membrane, which is linearly related to average fluid flow velocity through the canaliculi (Weinbaum, Cowin et al. 1994). Therefore, the final step remaining in this study is “to integrate” the fluid flow information to obtain a predictor for the mechanoresponse at the bone surfaces. Firstly, both the endocortical and periosteal surface were discretized in 180 arc-shaped elements each covering an angle of 2° . For each element a weighted mean of the fluid flow velocity, which is calculated using the canaliculi located in the “wedge” of 2° opening angle. The weighting follows the idea introduced by Mullender and Huiskes (1995) that contributions closer to the

surface are more important than farther away from it. Using an exponential weighting, the quantity that should predict the mechanoreponse of loaded bone in an element of the endocortical or periosteal surface was defined as

$$\left(\sum_j l_j\right)^{-1} \sum_j v_j l_j \exp\left[\left(\frac{r_j}{R}\right)\right], \quad (3.15)$$

with l_j the length of the canaliculus j and r_j the distance from the bone surface to canaliculus j . Weighted averaging is executed over all canaliculi within the wedge of 2° opening angle. Since the value of R is unknown, a parameter study was performed. After this, a triangular moving average (TMA) with a window size of 30° was used to take the range of influence at the surface into account.

3. Model Development – Mechanosensing via Load-Induced Fluid Flow

4. RESULTS AND DISCUSSION

4.1. Results of the Mouse Tibia Study

The aim of this PhD thesis is to test the fluid flow hypothesis by taking into account the architecture of the lacunocanalicular network (LCN) and to predict where bone is formed or resorbed after mechanical stimulation. For the first project of my PhD study our collaborators provided us with well characterized mouse bones. In these mice the response to controlled *in vivo* mechanical loading was imaged by Bettina Willie and Isabela Vitienes (McGill University, Montreal, Canada) following their well-established *in vivo* μ CT time-lapse protocol (Birkhold, Razi et al. 2015). I then imaged the LCN in bone volumes covering the whole cross-sections of these tibiae. Next, I used circuit theory to calculate the load-induced fluid flow through the LCN. I used the displacement data from an existing finite element model of one tibia, in order to define the local volumetric strain. I then used this local strain in combination with the volume of the imaged LCN to calculate the amount of load-induced fluid displacement. This integration of mathematical modeling with experimental techniques allows us to perform a direct spatial correlation between the measured mechanoreponse and my predicted mechanoreponse based on fluid flow patterns in the actual LCN architecture. Finally, I demonstrated how this approach allowed me to predict how common changes in LCN architecture can lead to strong increases in the mechanosensitivity of healthy human bone.

4.1.1. The Measured Mechanoreponse of Mouse Tibiae

In order to image the mechanoreponse of the mouse tibiae, the mid shaft was imaged using *in vivo* μ CT on day 0 (before loading) and day 15 (after two weeks of controlled loading). Registration of the two *in vivo* μ CT images provides information about where and how much bone was formed or resorbed on the endocortical and periosteal surfaces between day 1 to 5, day 1 to 10 and day 1 to 15. After 15 days most bone formation is found at posterior sites (Fig. 4.1, blue voxels), and significantly less bone is formed in the anterior direction. The endocortical surface shows more new bone at day 10 and 15 compared to the periosteal surface, especially in the anterior direction. Hardly any new bone is formed along the medial and lateral axis, while these are the location where resorption can occur (Fig. 4.1, red voxels). A quantitative evaluation of the mechanoreponse of the individual mice are shown later in this section (Fig. 4.5).

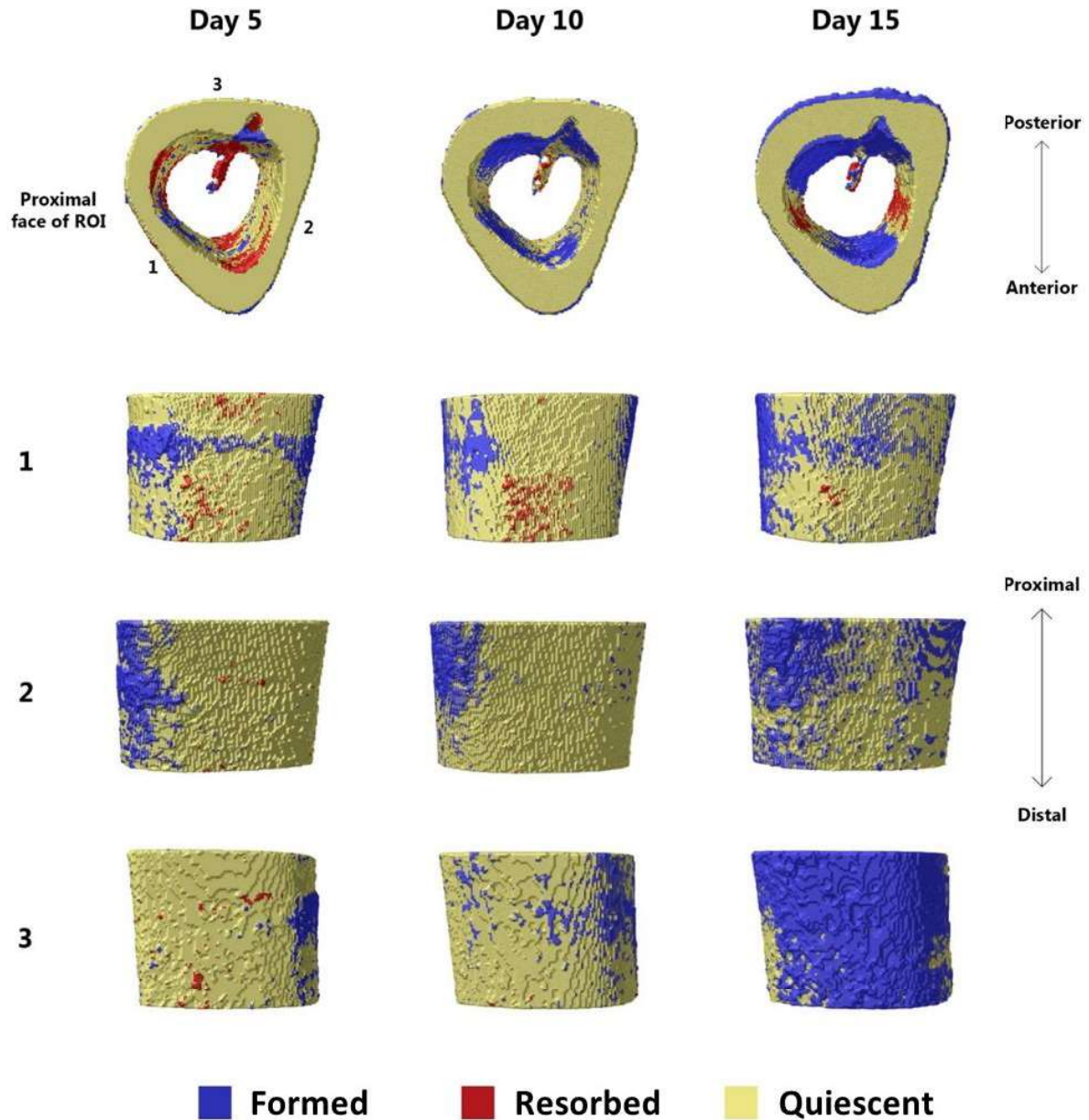


Fig. 4.1. 3D renderings showing the time-lapse of remodeling based on of the *in vivo* μ CT imaging of the diaphyseal region of the tibia of mouse 1. The anterior, lateral and posterior faces of the bone are indicated by the numbers 1 to 3, respectively. Blue denotes newly formed bone, red resorbed bone, and yellow quiescent bone. The amount of remodeling is calculated from the differences between the μ CT scans of day 1 to 5, day 1 to 10 and day 1 to 15, respectively.

4.1.2. Structural Heterogeneity of the Pore Networks in Mouse Tibiae

High resolution *ex vivo* μ CT scans showed vascular porosity within the cortical bone (Fig. 4.2 A-C). There is a strong heterogeneity in the distribution of the vascular canals. Most horizontally aligned vessels are clustered in the frontal side of the tibia mid shaft and are tens of μm in diameter (Fig. 4.2 A, B). All tibiae have one large vascular canal vertically on the posterior side of the bone, which is visible in the top of Fig. 4.2 C. The lower resolution of *in vivo* CT scans, which were made to image the remodeling history, were not able to resolve the small vascular canals (Fig. 4.2 D, E).

The CLSM images of the whole rhodamine stained tibia cross sections show the LCN (Fig. 4.2 G, I, J), as well as the vascular porosity (Fig. 4.2 I). Newly formed bone as a response to mechanical stimulation (to the right) is highly stained and, therefore, appears bright white. The 3D structure revealed a heterogeneity of the LCN with regions of looser (Fig. 4.2 I) and denser network (Fig. 4.2 J). A quantitative analysis of the network density in terms of canalicular density, Ca.Dn, (i.e., total length of canaliculi per unit volume) resulted in an average value of $0.27 \mu\text{m}/\mu\text{m}^3$. The frequency histogram (Fig. 4.3) shows a broad bell-shaped distribution with a standard deviation of $0.12 \mu\text{m}/\mu\text{m}^3$. The maps of the spatial distributions of Ca.Dn (Fig. 4.4 A) reveals that bands of low network density can be found in a ring-line structure, which runs eccentrically in the cortex in all three mice. Regions with a roughly ten-fold difference in network density can be found adjacent to each other. Evaluation of the pore volume fraction (i.e., contribution of only lacunae and vascular canals to the porosity) demonstrate that regions of high porosity spatially correlate with low network density woven bone regions (Fig. 4.4 B).

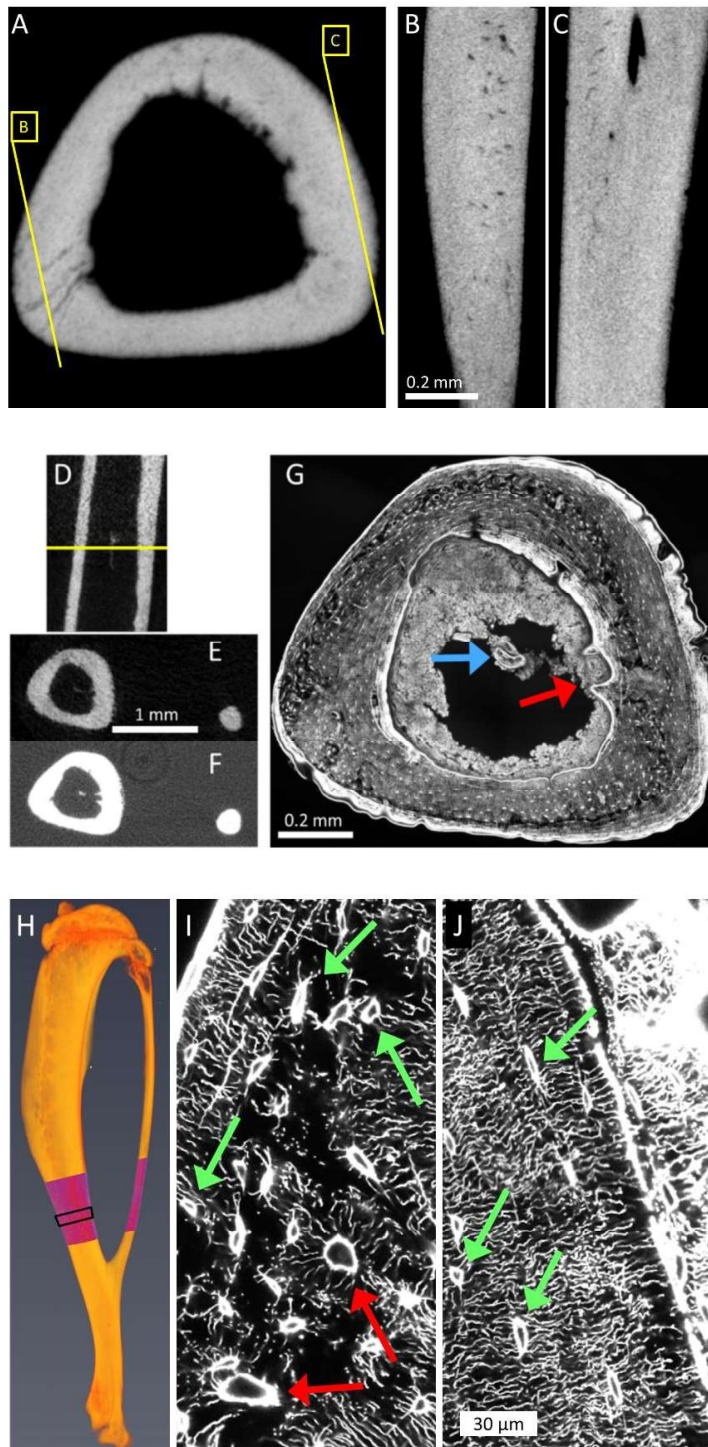


Fig. 4.2. Two techniques, μ CT and laser scanning confocal microscopy (CLSM) were used to image the levels of porosity in bone. High resolution *ex vivo* μ CT scans of the tibia were made to image features such as pores, trabeculae and vascular canals (A-C). Vascular canals, which cross the cortex, are clearly visible in minimum intensity projections (i.e. the lowest intensity) in 100 μ m thick sections of the high resolution μ CT scans (A). Single longitudinal sections from this μ CT scan (B-C) show that the small vascular canals (the black pores of tens of μ m in diameter) are clustered within bands over the longitudinal direction of the tibiae. These features cannot be clearly imaged with *in vivo* μ CT (D-E). The shape of the bone was used to register the *in vivo* μ CT scans (E), which cover only part of the bone, with the high resolution μ CT scans (F), which cover the complete bone. Tibiae were cut in the middle of the volume in the same region as the the *in vivo* μ CT scans to image the rhodamine stained LCN using CLSM (G). The exact location of the cut could be verified by matching features which are visible in both CLSM and high resolution μ CT scans (F-G). For example, one large vascular canal crosses the cortex of all the tibiae diagonally. The periosteal entrance of this canal is visible in F and G (red arrow). A trabecula (blue arrow) is also visible in both images. The black rectangle in (H) shows where the volume imaged with CLSM was located in the left tibia of mouse 1. CLSM revealed different network architectures within the same bone (I-J). Lacunae are marked with green arrows. The canaliculi are the white lines that form the network. The two vascular canals marked with red arrows (I) are too small to be seen in the high resolution μ CT scans (A). New bone was strongly stained due to the partial mineralization of the new tissue.

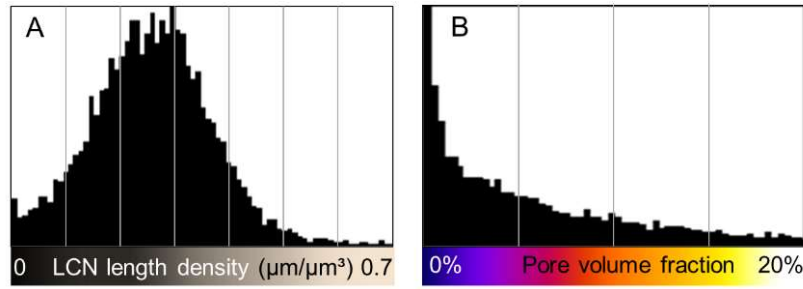


Fig. 4.3. A) Frequency distribution of canalicular length density (Ca.Dn, μm of canaliculi per μm^3 of bone volume). B) Frequency distribution of pore volume fraction (% of pore volume per unit of bone volume). The volumes of both lacunae and vascular pores are included.

4.1.3. Fluid Flow Induced by Controlled Loading of the Tibiae

We used a finite element mesh based on a high-resolution *ex vivo* μCT scan of a non-loaded mouse. This mesh was used in a Finite Element Model (FEM) by Hajar Razi before, to calculate the mechanical stress and strain distributions in the whole tibia (Razi, Birkhold et al. 2015). From the stress and strain patterns at the organ level we observed that the tibia undergoes bending, as the anterior region is under tension (i.e. positive strain), while the posterior region is compressed. This is due to the shape of the mouse tibiae, which are bend already in unloaded condition (Fig. 4.2 H). The highest strains are found close to the outer, periosteal surface with compressive strains larger than tensile strains (Fig. 4.5 B).

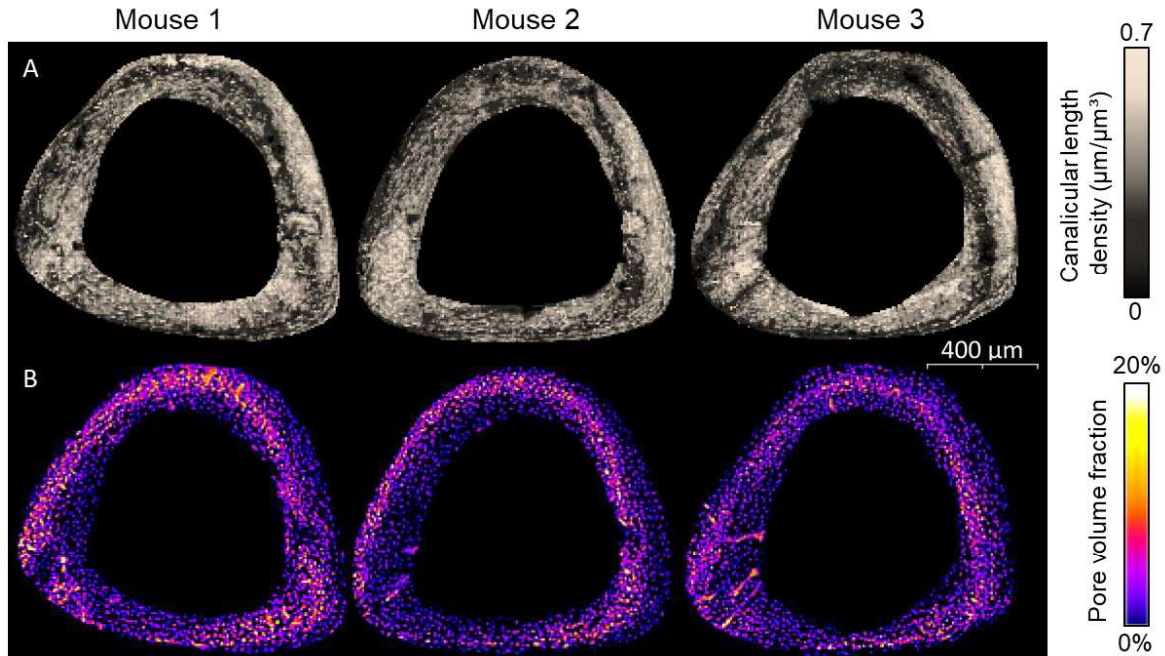


Fig. 4.4. Structural heterogeneity of the porosity within the tibial cross sections averaged over the imaging depth of 50 μm . A) Maps of canalicular densities Ca.Dn. B) Maps of pore volume fractions (i.e., volume of both lacunae and vascular canals per unit volume).

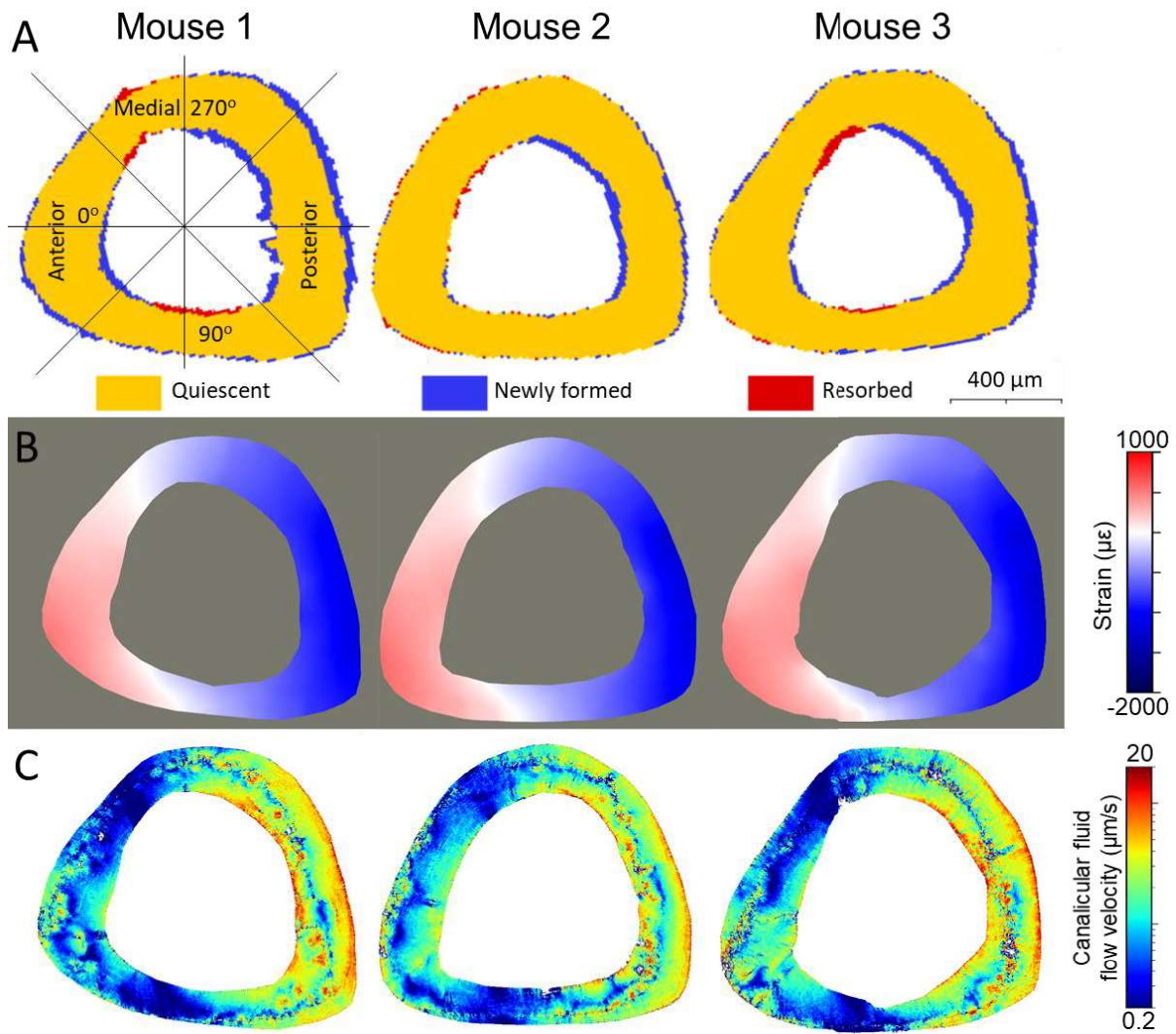


Fig. 4.5. A) Outcome of the *in vivo* μ CT experiment showing where in the diaphyseal region of the tibiae, bone was formed or resorbed in response to mechanical loading (blue denotes newly formed bone, red resorbed bone, and yellow quiescent bone; 2D cross-section of an imaged 3D volume). B) Spatial distributions of the strains induced by the maximum load during the *in vivo* loading experiment, calculated using finite element modeling. Red colors correspond to tensile, blue to compressive strains. The figure also introduces the angular coordinate system used to indicate locations at the endocortical and periosteal surfaces. The anterior direction is at 15° and angles increase counterclockwise. C) Patterns of fluid flow velocities through the LCN. Based on the loading conditions from B) and the 3D network architecture of Fig. 1A, the fluid flow velocity is calculated in each canaliculus using circuit theory. The fluid flow velocity information of all the canaliculi was rendered in a 3D image stack. For reasons of presentation this 3D image is averaged over the imaging depth to obtain the shown flow pattern.

We combined the local strain rates from the FEM model with the imaged 3D network architecture, to calculate the fluid flow velocity through each individual canaliculus employing circuit theory (see section 3.2 for model details). The resulting fluid flow patterns have an interesting “hybrid” character and show a striking spatial heterogeneity (Fig. 4.5 C), especially when compared to the smooth strain patterns (Fig. 4.5 B). The strain patterns reflect features of the typical strain distribution due to bending. A region of low fluid flow is located around the mechanically neutral medial-lateral direction in all three mice. However, some important features cannot be explained by strains and, therefore, have to be attributed to the LCN architecture: examples are the high fluid flow velocities close to the endocortical surface at the posterior side or regions of low fluid flow at the anterior side of the tibiae. The region of low network density is also spatially associated with on average low flow velocities. The fluid flow patterns show a wide variation between the three tibiae (Fig. 4.5 C), compared to strain patterns, which are very similar for all mice (Fig. 4.5 B). The posterior surfaces of mice 1 and 3 show a higher fluid flow velocity compared to mouse 2.

4.1.4. Prediction Local Bone Mechanoresponses

The result of the *in vivo* μ CT experiments measuring the amount of bone formed or resorbed averaged over the three investigated mice is shown in Fig. 4.6 (black line). The chart represents a transverse section through the mid-shaft of the mouse tibia. The amount of formed bone and resorbed bone (Fig. 4.6, black line entering the yellow ring) is not depicted to scale for reasons of clarity. The measured mechanoresponse is compared with the predictions from strain alone (pink line) and from load-induced fluid flow (green line). At the periosteal surface the prediction from strain is overestimating the mechanoresponse at the posterior side. Quantification of the difference between prediction and measurement as a root mean square error (RMSE) gives a value of 19 μ m for using strain as predictor and at the endocortical surface the error is 13 μ m.

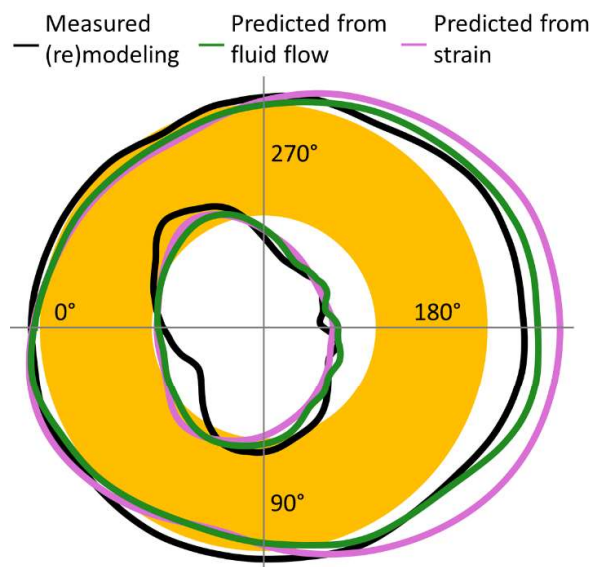


Fig. 4.6. Result of *in vivo* μ CT measurements in terms of bone formation and resorption after two weeks of controlled loading of the tibia. The tibial cross-section is represented schematically as a circular annulus (yellow). The black line denotes the amount of resorbed bone (line entering yellow cortex) and formed bone (depiction not to scale). The pink line denotes the prediction of the mechanoresponse based on strain only, the green line is the prediction based on load-induced fluid flow, which considers not only the loading condition but also the architecture of the LCN. Strain rate and fluid flow velocity were integrated over regions close to the surface (see section 3.4) to obtain a single value.

4. Results and Discussion

Since the LCN exhibits architectural differences for the individual animals, the prediction quality has to be assessed on the basis of the specific animals. Fig. 4.7 summarizes the outcome of the in vivo μ CT experiment (Fig. 4.7 B) and the predictions of the mechanoresponse for strain (Fig. 4.7 A) and fluid flow (Fig. 4.7 C) for all three investigated mice. The angle on the x-axis specifies the position at the surface (see Fig. 4.5). The two lines in all plots refer to the endocortical and the periosteal surface, respectively. In Fig. 4.7 B the value on the y-axis denotes the thickness of the formed/resorbed bone, where a binning angle of 2° was used followed by 30° triangular moving average. This thickness is defined as the total formed/resorbed volume divided by the surface area and is positive/negative for predominant formation/resorption. The sine wave-like curves show that formation is strongest around 190° (posterior direction) with a second smaller maximum at about 10° (anterior direction) and small minima (corresponding to resorption) in between (i.e., at bone's neutral axes). Two observations can be made: (i) the mechanoresponse is similar on both surfaces with a trend to higher values at the endocortical surface; (ii) the mechanoresponse in the three mice is substantially different with mouse 1 showing the strongest response, followed by mouse 3 and mouse 2. Fig. 4.7 C shows the evaluation of the fluid flow velocity through the LCN close to the surface (see section 3.4 for details), plotted similarly as the (re)modeling response. Also, the average flow velocities show the rough sine wave curves with maxima and minima at positions similar to the (re)modeling response with the strongest maximum again at roughly 190° . The flow velocities are similar for both surfaces, but different for different animals: mouse 1 displays the largest values for the fluid flow velocities, while mouse 2 has markedly the slowest fluid flow. It is important to contrast these results for the fluid flow with results for the local absolute strain rate close to the surface (Fig. 4.7 A, see section 3.4 for details). Since the shape of the tibia and the region of evaluation was very similar, the resulting curves for the strains at the endocortical and periosteal surfaces are almost identical for the three animals. In all mice the maximum strain rate was higher at the periosteal surface by about 35% compared to the endocortical surface.

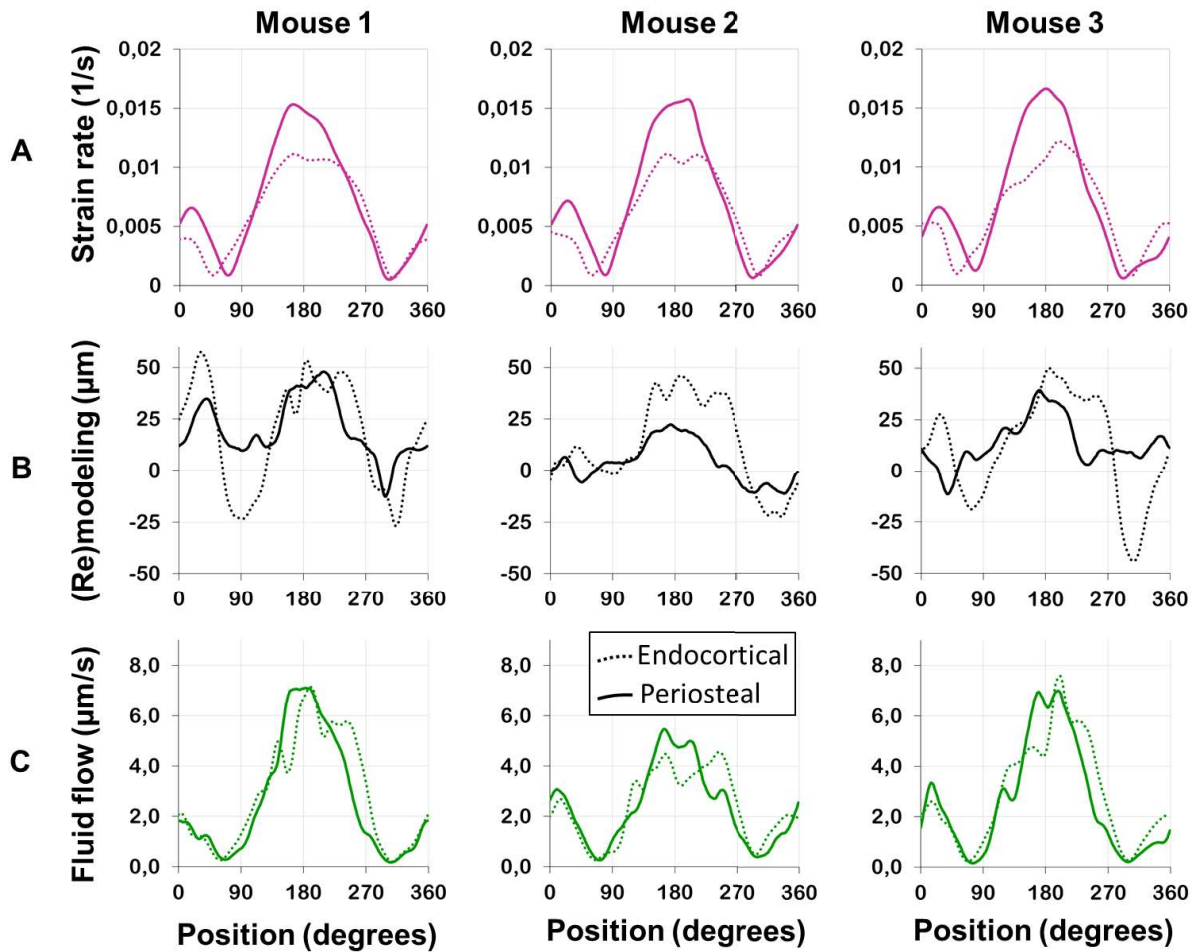


Fig. 4.7. Evaluation of absolute surface strain rate (A), (re)modeling thickness (B, defined as new bone thickness minus resorption cavity depth) and surface fluid flow velocity (C) for all three investigated mice (see Fig. 3B for definition of angles). Strain rate and fluid flow velocity were integrated over regions close to the surface (see methods, section 3.4) to obtain a single value. A) Strain rates at the endocortical surface (dotted line) are lower compared to the periosteal surface (solid line) and the spatial distribution and peak values are very similar between mice. B) The mechanoreponse shows individual differences in bone (re)modeling, with mouse 2 showing less (re)modeling compared to the two other mice. C) Also surface fluid velocity was found to be lower in mouse 2, while for all animals the flow velocities show similar distributions on the endocortical and periosteal surfaces.

4.1.5. Discussion of the Mouse Tibia Study

To study the effect of the osteocyte LCN on the mechanoreponse of mouse tibiae we first measured the mechanoreponse to the controlled loading of the mouse tibiae. After sacrificing the mice the architecture of the lacunocanicular network was measured in exactly the same region of these tibiae. Then the network information was used for a functional interpretation by calculating the fluid flow through the LCN and by predicting the bone's mechanoreponse. Noteworthy is the strong spatial heterogeneity of the network with an intracortical band of loose

network (Kerschnitzki, Wagermaier et al. 2011, Genthial, Gerbaix et al. 2019, Shapiro and Wu 2019) and high porosity within the tibial cross-section. This band correlates spatially with the woven bone found in murine bone and islands of calcified cartilage, which are thought to be a remnant of early life (Kerschnitzki, Wagermaier et al. 2011, Ip, Toth et al. 2016). Additionally, this woven bone is associated with a higher density of vascular canals compared to lamellar bone. This heterogeneity implies a caveat when reporting changes in the network architecture of mice due to disease or treatment. Only a 3D mapping of large bone volumes ($> (50 \mu\text{m})^3$) yields reliable values for parameters characterizing the LCN architecture.

Therefore, the porosity of the LCN acts not only as transport network for the fluid in this approach, but also as source of fluid that has to be drained via the network. Such a poroelastic description of bone is the preferred model approach of most researchers studying load-induced fluid flow in the LCN (Weinbaum, Cowin et al. 1994, Smit, Burger et al. 2002, Nguyen, Lemaire et al. 2010, Cardoso, Fritton et al. 2013). The network architecture crucially influences the fluid flow through the LCN and, consequently, the mechanical stimulation of the osteocytes. Consideration of the LCN architecture leads to qualitatively different results than considering strain alone. We found that fluid flow through the LCN allows one to predict the sites of bone formation correctly in individual animals and on different bone surfaces (endocortical vs periosteal). Moreover, our analysis allows one to identify mechanisms of how the local network architecture modulates the velocity of the local fluid flow. We identified a mechanism to locally cause a high flow velocity close to surfaces, which is associated with a strong mechanoresponse. Here, when approaching the bone surface, the network converges, with the fluid flow being “funneled” into fewer canaliculi (Fig. 4.2 J). The (practical) incompressibility of the fluid causes an acceleration of the fluid, once a reduced number of canaliculi are available. A very different mechanism is responsible for the reduction in the fluid flow, namely the structural incorporation of vascular canals (Fig. 4.2 I). The fluid flow patterns (Fig. 4.2 C) demonstrate how vascular canals can act as additional sinks/sources, and thereby shield the nearby bone surface from fluid flow. Although this shielding effect of vascular canals was already hypothesized based on continuous FE modeling (Gatti, Azoulay et al. 2018), our data confirms how the exact position of the vascular canals and the interplay with the LCN architecture affects bone (re)modeling. The interpretation of fluid flow through networks is based on the principle that fluid flows predominantly through the path of least resistance among a set of alternative paths within networks. Since vascular canals are located especially near regions with a less dense and less connected LCN (and, therefore, of high flow resistance) (Fig. 4.2 I), the path towards these vascular canals is the preferred flow path, thereby reinforcing their “shielding effect”.

The intricacy of the lacunocanalicular network architecture make model assumptions necessary. Although the vascular network shows to be important for our study, we did not investigate the vascular network architecture at the scale of the whole tibia. Instead we adapted the widely accepted assumption that the vascular pressure has a negligible impact on fluid flow in the LCN,

as it acts as a constant low pressure reservoir due to the fast relaxation times in the order of 1ms (Cowin and Cardoso 2015). Additionally, the quality of the imaged vascular network was inadequate for analysis, due to technical limitations. The *ex vivo* μ CT scans reveal only the larger pores of the vascular network. Thinner vascular canals appeared non-continuous and the diameter of the vascular canals could not be assessed. This is a drawback of measuring porosity using μ CT (i.e. absorption techniques), as the absolute decrease in intensity due to pores is relatively miniscule compared to the high intensity background. This leads to differences in intensity which are hardly distinguishable from the noise. In contrast, the same absolute increase in intensity in fluorescence is very strong compared to the black background. Therefore, we see a near perfect signal to noise ratio in our confocal microscopy images of the LCN, even if the canaliculi are thinner than the optical resolution of roughly 300 nm (Fig. 4.2 G, I, J). Consequently, the annulus region, where fluid can flow within the canaliculi, was assumed to have a cross sectional area of $0.045 \mu\text{m}^2$ for all canaliculi. The fluid does not flow freely through this annular space, but is substantially impeded by its fibrous filling. As a consequence, the fluid flow velocity does not depend as strongly on the dimensions of the annular space, as in a completely open canal (Weinbaum, Cowin et al. 1994).

It is possible to image the LCN with higher resolution with state-of-the-art techniques, such as a scanning electron microscope (SEM) equipped with a focused ion beam (FIB) to mill the surface specimen with high precision. In collaboration with another PhD student, Mahdi Ayoubi, we imaged the same region of bone with both CLSM and the FIB/SEM instrument (Fig. 4.8). All canaliculi which were visible in FIB/SEM images of mineralized bone were also visible in the CLSM images. The resolution of FIB/SEM is high enough to resolve the diameter of canaliculi, however, the field of view was by far too limited to image the whole cross section of the mouse bone. The value of this larger field of view to study networks can be explained by using a road network, and the traffic flows on it, as an analogy. Imagine a highway, where you can see how fast cars can drive based on the quality and curvature of the road. It is still challenging to predict what the traffic flow is on the single highway segment, without knowing what happens elsewhere in the road network. Moreover, local fluid flow patterns have already been investigated in models with single lacunae (Verbruggen, Vaughan et al. 2014, Vaughan, Mullen et al. 2015) and within single canaliculi (Anderson and Tate 2008, Kamioka, Kameo et al. 2012). Using the high-resolution FIB/SEM images in our study would therefore not significantly contribute to the current knowledge of fluid flow patterns in the LCN. In contrast the network topology of the LCN at the scale of the whole mouse tibia cross section is largely unexplored. Therefore, analysis of the 3D images of the LCN in whole cross sections of the mouse tibiae (Fig. 4.2 G) is an optimal compromise between resolution and field of view, which made the analysis in our study possible. The imaged volume of the mouse tibia contains approximately 4.5 million canaliculi. The large number of canaliculi also restricts the accuracy of the fluid flow calculations compared to previous works which analyzed the fluid flow through single lacunae with their adjacent canaliculi (Verbruggen, Vaughan et al. 2014, Vaughan, Mullen et al. 2015) or within single canaliculi

(Anderson and Tate 2008, Kamioka, Kameo et al. 2012). In particular, our model does not consider any interplay between the fluid flow and the shape of osteocyte bodies.

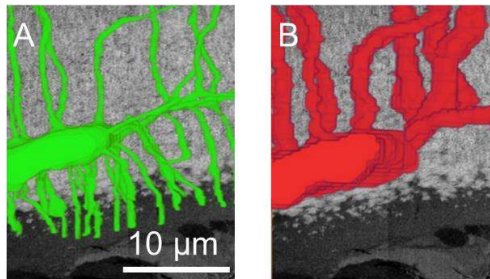


Fig.4.8. The same region of human osteonal bone was imaged in 3D with both FIB/SEM and CLSM. A) With 4 nm resolution the FIB/SEM can resolve the diameter of the canaliculi, however the field of view is limited to roughly hundred micrometer. B) Due to the ~300 nm resolution of CLSM the diameter of the canaliculi cannot be resolved, however, it can be used to image the topology of the canaliculi in much larger fields of view.

Newly formed unmineralized bone is overstained with rhodamine in our mice (Fig. 4.2 J). In collaboration with Mahdi Ayoubi we showed that canaliculi already form before the newly formed bone mineralizes (Fig. 4.8 A). We observed in the FIB/SEM data that canaliculi connected to the surfaces of the bone (including vascular canals), even in newly formed unmineralized bone. Thus, we can assume that liquid can be easily drained to the low pressure reservoirs at the surface, even if there is new bone formed. Therefore, we predicted fluid flow based on the LCN architecture before the mechanoresponse and excluded new bone formation and resorption from analysis. In reality, the adaptation process is more dynamic, so that the first bone (re)modeling would already have an influence on the fluid flow pattern. Additionally, osteocytes may be even able to actively manipulate the permeability of certain canaliculi, for example by obstructing the fluid flow with their cell processes. Such an active control of the fluid flow would allow indirect communication between osteocytes (Weinkamer, Kollmannsberger et al. 2019). In addition, it has been shown that adaptation has a noticeable impact on the strain distribution (Sztefek, Vanleene et al. 2010). Our approach can be justified by the observation that there was a time delay between mechanosensing and actuation in terms of bone formation and resorption. A strong mechanoresponse was only observed at day 15. Therefore, the modeled strain and fluid flow patterns would be correct for the majority of the experiment. Moreover, the mechanoresponse to the altered fluid flow pattern in the last few days of the experiment would not be visible yet on day 15. Consequently, to predict bone's mechanoresponse, one should analyze the mechanical stimulation in its recent past. For this reason, we used a finite element mesh based on a high resolution *ex vivo* μ CT scan of a non-loaded mouse.

The time-consuming analysis was limited to three mouse tibiae only. While repeating similar studies is desirable, probably more progress in our understanding of bone's mechanobiology can be made by extending the analysis to different bones in the mouse, to larger bone volumes (Javaheri, Razi et al. 2020) and to different small animals. The strength of our model approach is that an assessment of fluid flow in the whole network can be performed, although the large number of canaliculi poses a challenge to computational resources available nowadays. The result of the

analysis are patterns of fluid flow velocity with a striking spatial heterogeneity (Fig. 4.5 B), especially when compared to the smooth strain patterns (Fig. 4.5 C).

A topic which has been largely neglected by bone researchers, because it is so hard to address, is the problem of signal integration: how are the biological signals, which are produced by various osteocytes as a response to fluid flow, then added up and transported to the surface of the bone to orchestrate the behavior of osteoblasts and osteoclasts after mechanotransduction? In the scope of our model we therefore asked, how should the averaging over the fluid flow velocities in the LCN be performed to obtain a good predictor for bone's mechanoreponse? Our analysis also allows us to speculate on this point. In our fluid flow analysis, the predictive power of the bone's mechanoreponse is best, when the weighted average of the flow velocity (see Methods section) is restricted to canaliculi only tens of micrometers away from the bone surface. If the mechanosensitivity is largely restricted to network contributions close to the surface, this would have important implications for bone adaptation. The continuous bone apposition at the periosteal surface in mice and humans (Ruff and Hayes 1988) could be used for a continuous adaptation of the network architecture to modulate the flow through it. A feedback mechanism has been hypothesized based on the experimental finding that the osteocyte density correlates with bone apposition rate (Qiu, Rao et al. 2002, Buenzli 2015). Also the strong heterogeneity in LCN architecture in mice can be associated with differences in bone formation rate (Hernandez, Majeska et al. 2004). For example, this could explain why some surfaces have a more sensitive 'funneling LCN architecture' (Fig. 4.2 J).

While fluid flow is an excellent predictor of bone formation, this holds much less for resorption. A valid prediction is that no resorption was found when the average fluid flow velocity at the surface is above 5 $\mu\text{m/s}$. However, the resorption at the periosteal surfaces was noticeably less compared to the endocortical surfaces, despite the surfaces having very similar fluid velocities. We want to provide four possible reasons for shortcomings of model predictions: (i) especially for the case of resorption, it has been proposed that microdamage in the bone could act to trigger the process (Burr, Martin et al. 1985, Noble and Reeve 2000, Verborgt, Gibson et al. 2000); (ii) since similar endocortical bone resorption is also observed at the non-loaded limb (Birkhold, Razi et al. 2014), this could be a response uncoupled to mechanics and related to shape changes of the whole tibia (Javaheri, Razi et al. 2020); (iii) to understand details of mechanotransduction, a more microscopic viewpoint than taken here is necessary, to consider the role of integrins (Wang, McNamara et al. 2007) and the glycocalyx (Thompson, Modla et al. 2011, Sansalone, Kaiser et al. 2013, Cowin and Cardoso 2015, Wijeratne, Martinez et al. 2016); (iv) although this study focuses on biomechanical aspects of bone adaptation, we do not want to give the wrong impression that molecular and cell biological aspects should take a back seat. In the end, cells must be available and they have to comprehend and execute instructions that are provided by mechanical stimulation. Metaphorically speaking, our point of view for bone's mechanosensitivity is that the LCN is the hardware, on which the biological software can play.

4. Results and Discussion

4.2. RESULTS OF THE HUMAN OSTEONAL BONE STUDY

The second project of my PhD work focused on the lacunocanalicular network (LCN) of human osteonal bone. The assessment of bone's mechanosensitivity is crucial for understanding human bone health. With age the bone was shown to lose its mechanoresponsiveness (Razi, Birkhold et al. 2015). This loss of responsiveness is more pronounced in females after menopause. Changes in the responsiveness of bone are very often addressed on the cellular and subcellular level by elucidating signaling pathways from the cell membrane to the nucleus and back (Chen, Liu et al. 2010, Jacobs, Temiyasathit et al. 2010). However, our mouse study suggests that we should not focus exclusively on osteocytes and their interaction with each other, but also to consider the flow of the interstitial fluid through the LCN. Therefore I aimed to investigate how changes in the human LCN could influence the mechanoresponsiveness of bone at the onset of menopause. In this investigation, I combined three experimental and computational methods: (1) I used staining and laser confocal microscopy to image the three-dimensional LCN, (2) I performed image analysis to transfer the image into a mathematical network structure, (3) I used the circuit theory based on Kirchhoff's circuit laws to calculate the fluid velocity in the individual canaliculi of the imaged networks, to predict local differences in the mechanoresponse to increased mechanical loading.

4.2.1. The LCN Architecture of Human Osteonal Bone

As a first step we selected human osteons with different LCN topology to investigate the effect of LCN architecture on the fluid flow patterns in these osteons. Fluid flow was studied in both ordinary osteons with a rather homogeneous LCN as well as a frequent subtype of osteons—so-called osteon-in-osteons—which are characterized by a ring-like zone of low network connectivity between the inner and the outer parts of these osteons. Fig. 4.9. shows a low resolution 2D overview image of part of a cross section from the femur midshaft of a 57 year old woman without any known bone-related disease. The bone section was provided to us by Boltzmann Institute of Osteology, Vienna, Austria. We found that roughly 10% of the osteons in this cross section were osteon-in-osteons. Both types of osteons were found throughout the whole cortex (i.e. covering the whole distance between the endosteal to periosteal surface). On the overview we selected 12 osteons and an additional 12 ordinary osteons (yellow and purple, respectively, in Fig. 4.9).

An example of a 3D high-resolution image of an ordinary osteon (#14) is shown in Fig. 4.10 A. An osteon-in-osteon with a very clear ring of low connectivity was selected as a representative osteon-in-osteon (Fig. 4.10 B, osteon #10). With the reflection signal (i.e. the observed light with the same wavelength as the excitation laser) we could image the lamella of all osteons, which lay concentric around the Haversian canal. Most canaliculi are oriented in the radial direction, i.e. perpendicular to the lamellae. After inspection of all 3D confocal image stacks we selected 8 ordinary osteons and 9 osteon-in-osteons without any cracks or other damage. Average structural

parameters of these osteons are compared in table 4.1. Although the osteons in the two groups have very similar sizes, the size of the Haversian canal was larger in ordinary osteons compared to the osteon-in-osteons ($P < 0.001$). Table 4.1 also compares structural LCN parameters such as number of intersecting canaliculi and lacunae per volume, number of canaliculi per volume, node degree (i.e. average number of canaliculi meeting in a node, or the total length of the canaliculi meeting in a node).

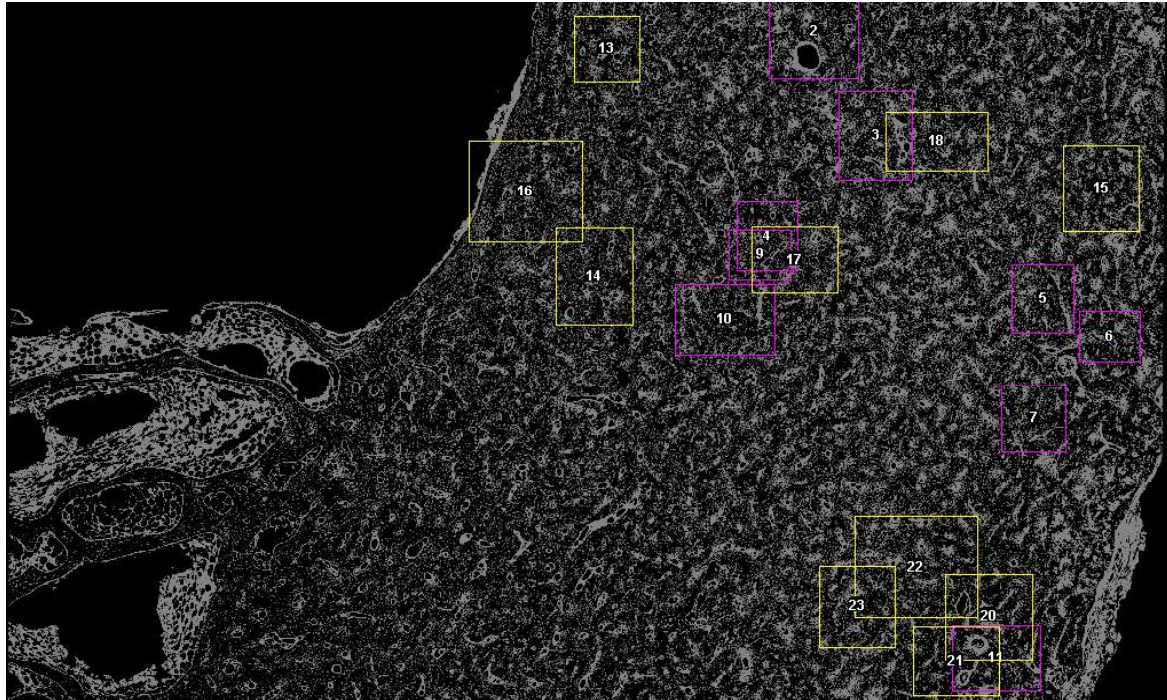


Fig. 4.9. A low resolution 2D overview image of the surface of the cross section of the human femur, imaged by confocal laser scanning microscopy. The pinhole of the confocal microscope was opened as far as possible to maximize the optical section thickness (i.e. to decrease the z-resolution (Wilson 2011)). This image was used to select 12 osteon-in-osteons (purple markers) and 12 ordinary osteons (yellow markers) for further investigation.

These parameters did not show any significant difference between the osteon types. However, the average path length through the LCN was in osteon-in-osteons 80% longer compared to ordinary osteons. This difference in the accessibility of the Haversian canal can be explained by looking at the networks of the two osteon types (two representative examples in Fig. 4.10 A, B). When we color code the nodes of these osteons based on tortuosity (the ratio between distance from the node to the Haversian canal via the network over the direct Euclidian distance to the Haversian canal), we see that the network of the ordinary osteon is well connected and oriented relatively straight to the Haversian canal (Fig. 4.10 C). In osteon-in-osteons the nodes in the outer part have a much higher average tortuosity, due to the detour that has to be taken to reach the Haversian canal (Fig. 4.10 D). This demonstrates how a local drop in network density divides the osteon-in-osteon into two parts, the inner and outer osteon. Only few bridges connect the inner and outer osteon, as indicated by the arrows in Fig. 4.10 B.

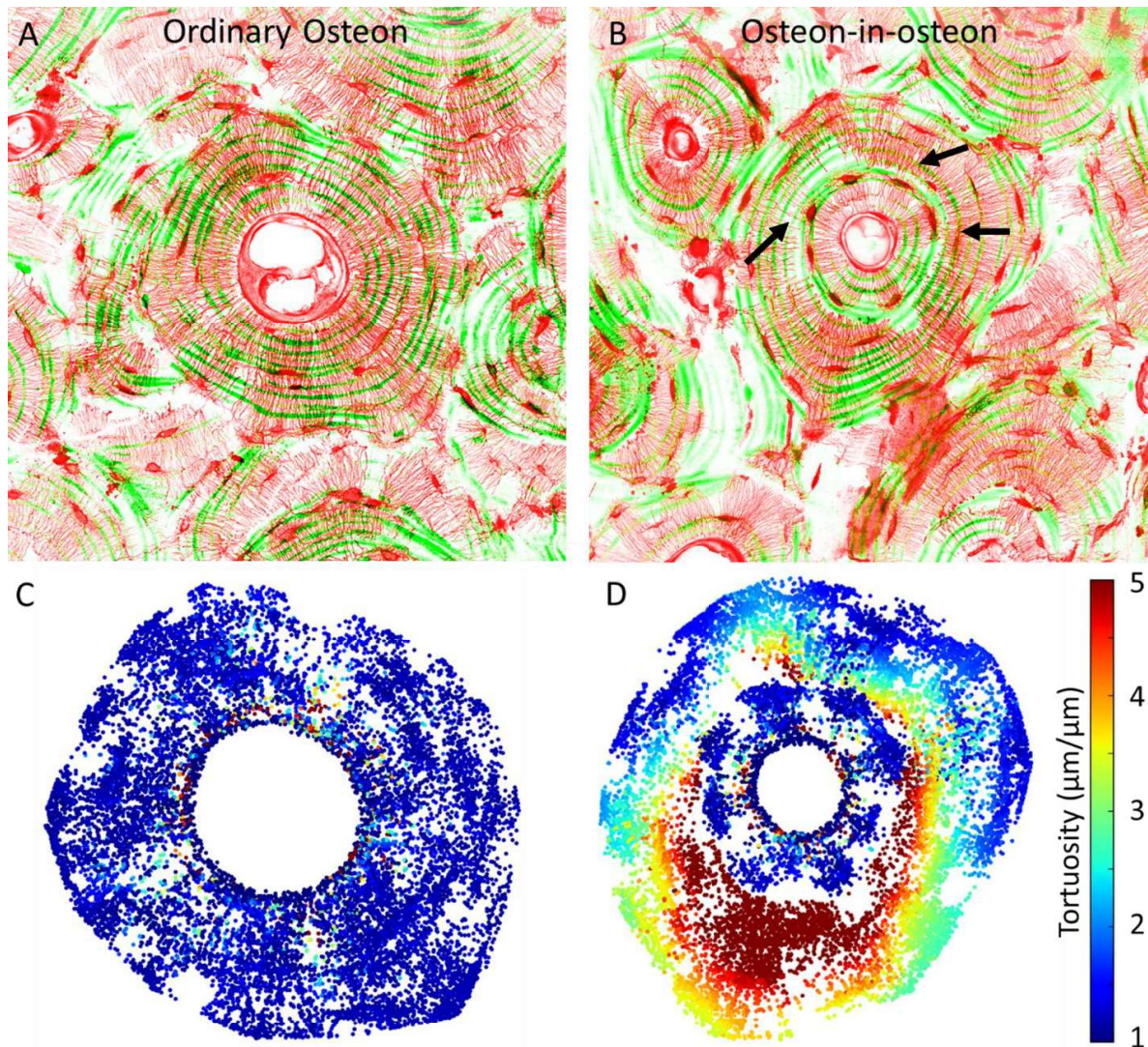


Fig. 4.10. A-B) Confocal microscopy images of human osteons. The fluorescent signal of rhodamine, projected over the whole imaging depth, shows the stained LCN (red). The reflection of the green excitation shows the lamella of the osteon due to a preferred orientation of the collagenous matrix within the image plane (the concentric green rings). The canaliculi in both osteons are mostly oriented in the radial direction, perpendicular to the lamella. Both osteons have regions which are free of any stained network. The canaliculi in the ordinary osteon (A) are mostly well connected from cement line to Haversian canal, while the osteon-in-osteons (B) is characterized by a ring of strongly reduced LCN connectivity. The Haversian canal of osteon-in-osteons is smaller. C-D) The tortuosity shows the path length through the LCN, normalized by the distance directly to the Haversian canal. C) The tortuosity in the ordinary osteon is generally between 1 and 2, which is due to the relatively straight and well connected canaliculi as seen in (A). Only few nodes have a high tortuosity in the ordinary osteon due to small free of network regions. D) The tortuosity in the osteon-in-osteon is much higher, due to the detour that has to be taken from certain parts of the outer osteon to the Haversian canal. This is especially true for regions far away from bridging canaliculi between the inner and outer osteon.

Table 4.1. Structural parameters for each osteon type group.

	Ordinary osteons	Osteon-in-osteons
osteon parameters:		
On.Rd	$104 \pm 22 \mu\text{m}$	$103 \pm 13 \mu\text{m}$
HCa.Rd	$36 \pm 6 \mu\text{m}$	$22 \pm 5 \mu\text{m}$
evaluated.BV	$1.2 \cdot 10^6 \pm 5.6 \cdot 10^5 \mu\text{m}^3$	$1.3 \cdot 10^6 \pm 3.0 \cdot 10^5 \mu\text{m}^3$
LCN parameters:		
number density of nodes	$0.015 \pm 0.002 \text{ 1}/\mu\text{m}^3$	$0.014 \pm 0.003 \text{ 1}/\mu\text{m}^3$
number density of canaliculi	$0.021 \pm 0.003 \text{ 1}/\mu\text{m}^3$	$0.019 \pm 0.004 \text{ 1}/\mu\text{m}^3$
length density of canaliculi	$0.081 \pm 0.008 \mu\text{m}/\mu\text{m}^3$	$0.072 \pm 0.009 \mu\text{m}/\mu\text{m}^3$
node degree	3.62 ± 0.08	3.65 ± 0.04
weighted node degree	$11.9 \pm 0.76 \mu\text{m}$	$11.3 \pm 0.90 \mu\text{m}$
average shortest path length	$50.0 \pm 11.5 \mu\text{m}$	$92.8 \pm 32.3 \mu\text{m}$

4.2.2. Load Induced Fluid Flow in Human Osteons

With this knowledge of the LCN architecture we can now predict what impact the LCN architecture of the different types of human osteons has on the mechanoresponse. The two representative osteons (Fig. 4.12) are therefore used to demonstrate how simulated load-induced fluid flow pattern differs between the two osteons in Fig. 4.11.

The ordinary osteons show generally a higher fluid flow velocity near the Haversian canal, while in most canaliculi at the cement line (i.e. the sealed part of the osteon) the flow velocity is very low. The fluid flow velocity in the radial canaliculi is generally higher in the radial canaliculi, which form the most direct path to the Haversian canal (i.e. to the low pressure reservoir), compared to lateral canaliculi (i.e., canaliculi perpendicular to the radial direction). Note that the color code in Fig. 4.11 is logarithmic, and that the fluid flow pattern shows a strong heterogeneity. The velocity in the canaliculi connecting to the Haversian canal varies roughly over an order of magnitude. The heterogeneity in osteon-in-osteons is even stronger (Fig. 4.11 B). The fluid displacement forces the fluid flow in osteon-in-osteons to be concentrated on paths to the bridges between the inner and outer osteon. Therefore, the fluid flows via the tangential canaliculi in large

parts of the outer osteon. As a result of the very few bridges in this osteon-in-osteon the fluid flow of the outer osteon is almost exclusively flowing via the upper half of the inner osteon, resulting in a fluid flow velocity which is roughly two orders of magnitude higher compared to the fluid flow in the lower half of the inner osteon.

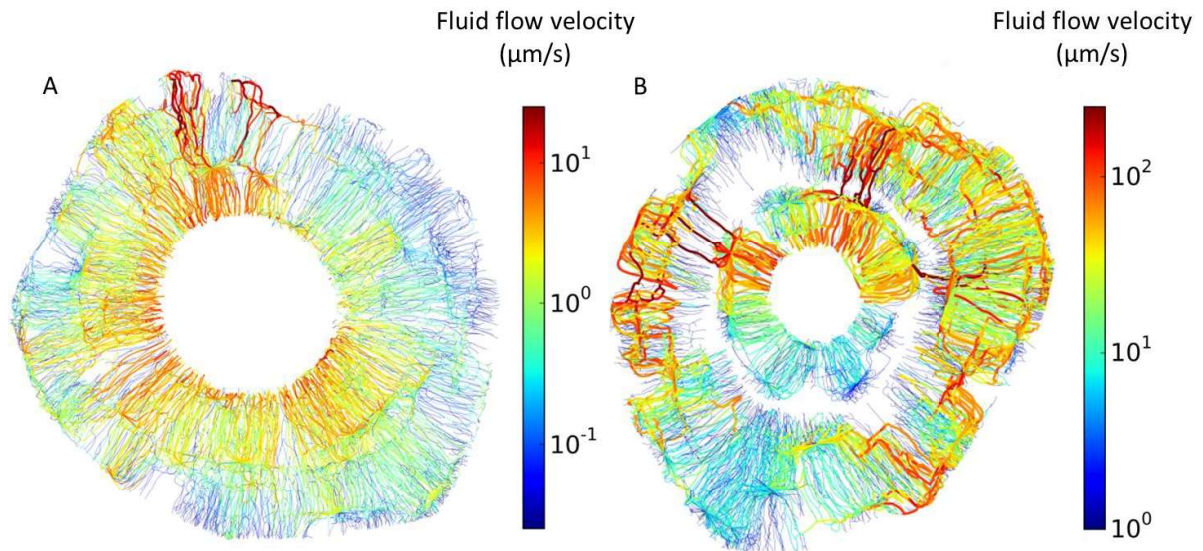


Fig. 4.11. In the model fluid flow was forced out of the ordinary osteon (A) and osteon-in-osteon (B) as water is squeezed out of a steadily compressed sponge (i.e. strain rate is constant). A and B show the fluid flow patterns resulting in an ordinary osteon and an osteon-in-osteon, respectively. The fluid flow patterns in the lacunar-canalicular network are projections of the network in the style of a road map, where in addition to the color code edges with higher fluid flow velocity are rendered thicker.

Quantitative analysis (Fig. 4.12 A) shows that average fluid velocities are higher close to the Haversian canal compared to close to the cement line, independent of osteon type. The mean path length to the Haversian canal, the structural network parameter that differs mostly between osteon types, correlates directly with the average fluid velocity (Fig. 4.12 B). As a result of the longer path lengths in the osteon-in-osteons fluid flow velocity is 2.3 times higher in this osteon type compared to the ordinary osteons ($p < 0.01$) (Fig. 4.12 A, right).

4.2. Results of the Human Osteonal Bone Study

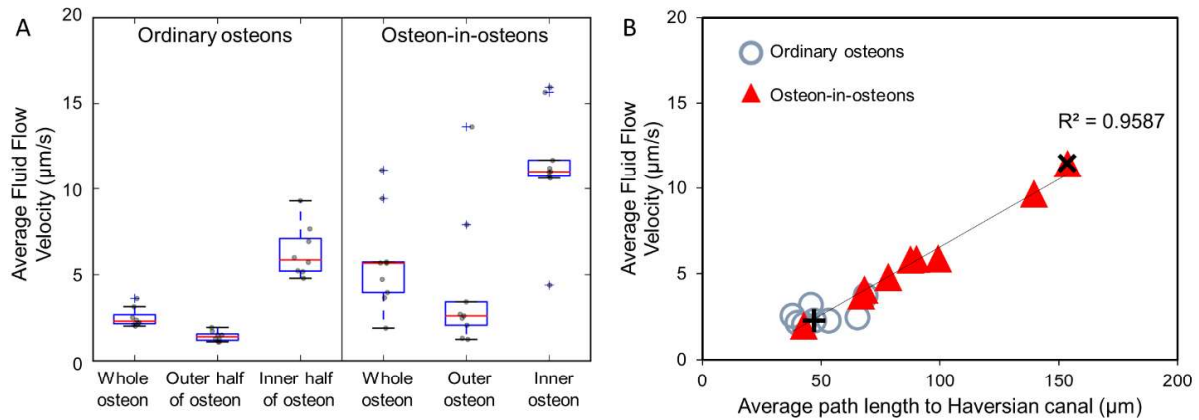


Fig. 4.12. A) The average fluid flow velocity of different parts of the 8 ordinary osteons and 9 osteon-in-osteons. The halves of the ordinary osteons are divided at half the distance from Haversian canal to the cement line. The box extends from the first to third quartile, the red line shows the median and the whiskers extend from the box to show the full range of the data. B) The average fluid flow velocity shows a strong correlation with a purely structural network parameter, the average path length from each node of the network to the Haversian canal. The representative ordinary osteon (+) and the osteon-in-osteon (x) are marked.

The fluid flow hypothesis and experiments on single ‘osteocyte-like’ cells suggest that osteocytes are particularly sensitive to shear forces on their cell processes (Bonewald 2011). Therefore, the shear forces were calculated from the fluid flow velocities (Eq. 1.2). Cumulative probability distributions of fluid shear stresses (Fig. 4.13) reveal which fractions of cell processes are exposed to shear forces larger than the value plotted on the x-axis. For comparison the shear forces above 0.4 Pa, which was demonstrated in in vitro experiments to trigger osteogenic responses in osteocyte-like cells (Klein-Nulend, Vanderplas et al. 1995, Bakker, Soejima et al. 2001, Bacabac, Smit et al. 2004, Jacobs, Temiyasathit et al. 2010) has a shaded gray background. The cumulative probability distributions for ordinary osteons and osteon-in-osteons intersect at a shear stress of 0.8 Pa and a probability of 45%. This means that more canaliculi above this value of 0.8 Pa can be found in osteon-in-osteons. Decreasing the strain rate from 0.015 s^{-1} to 0.0015 s^{-1} (i.e. simulation of walking instead of running), shifts the intersection to 0.08 Pa. Here the percentage of canaliculi which are stimulated with a shear stress larger than 0.8 Pa are 6.6-times more numerous in osteon-in-osteons than in ordinary osteons (9.3% and 1.4%, respectively).

The flow pattern includes very high fluid velocities and a strong spatial heterogeneity. Following only canaliculi with high fluid velocity (red canaliculi in Fig. 4.11 B) paths can be found that connect the cement line with the Haversian canal. However, these paths are not straight, but rather lengthy due to the requirement that they have to pass via the few bridges connecting outer and inner osteon. A longer chain of lacunae and canaliculi contain a larger amount of fluid. Therefore, a longer pathlength is also a larger source of fluid flow, which has to be transported through the network. This feature of acting as a source of fluid, which has to be drained via the network, causes

these high velocities of the interstitial bone fluid of longer paths. This interpretation of the high fluid velocities found in osteon-in-osteons explains the good correlations of the mean fluid velocity with a structural parameter of the network: the average shortest path length. The source-character of the LCN porosity relates longer paths with more fluid that has to be drained to the Haversian canal. This can happen only by speeding up the fluid flow and, therefore, the average fluid flow velocity shows a direct proportionality with the average shortest path length.

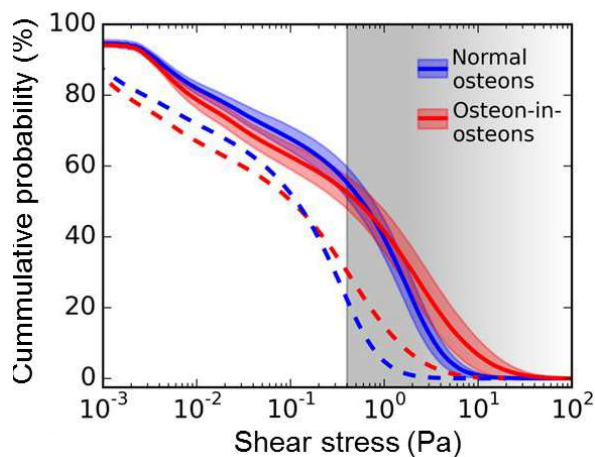


Fig. 4.13. The cumulative probability distributions of fluid shear stresses at the cell process surfaces in the canaliculi are plotted for ordinary osteons (blue) and osteon-in-osteons (red) for the case of strenuous exercise (solid lines) and normal daily activities (dashed lines). All lines show the mean percentage of canaliculi with a shear stress larger than the value on the x-axis. The 99% confidence intervals of the mean are shown in the faintly colored bands around the lines. The shaded area above 0.4 Pa illustrates the range of shear stresses where osteocytes showed osteogenic responses to fluid shear stress in in vitro experiments (Klein-Nulend, Vanderplas et al. 1995, Bakker, Soejima et al. 2001, Bacabac, Smit et al. 2004, Jacobs, Temiyasathit et al. 2010).

4.2.3. Fluid Pressure in Human Osteons

The load-induced pore pressure patterns of two representative osteons of different type are shown in Fig. 4.14. The two different ranges of the pressure observed in osteon-in-osteons, low pressure in the inner and high pressure in the outer osteon, are due to the few bridges connecting the inner and outer parts. The pressure encountered on a radial path from the cement line to the Haversian canal depends strongly on the starting point on the cement line. Using as an example the osteon of Fig. 4.14 A, the pressure gradient is maximal at a direction corresponding to 12 o'clock while rather nearby at around 2 o'clock the pressure gradient is much lower. This heterogeneity of the pressure pattern is more pronounced for the osteon-in-osteons. To quantify the angular dependency of the pressure pattern, the roughly circular osteon was subdivided into 36 sectors with an opening angle of 10 degrees and the average pressure was calculated over all the nodes in each sector together with the relative standard deviation of these 36 mean values. While the relative standard deviation was only 12% for both ordinary osteons and osteon-in-osteons, it was 44% for ordinary osteons and 53% for osteon-in-osteons.

By comparing all studied osteons, we observed a high variability in the pressure pattern between osteons, particularly in osteon-in-osteons. As shown in Fig. 4.15 A, the pressure profiles are non-linear and very different, especially in osteon-in-osteons. For example, the pressure at the cement line – which is not fixed in our modeling approach – varies by more than a factor of three, between 7 kPa and 25 kPa. This high variability is even stronger for osteon-in-osteons (Fig. 4.15 B). In osteon-in-osteons one smooth line per osteon (LOWESS fit) provides only a poor rendering of the pressure profile from the Haversian canal to the cement line, due to the much stronger angular dependency of the pressure pattern. The pressure values which are found in osteon-in-osteons are much higher than in ordinary osteons. The average pressure in the osteon-in-osteons is 12 times higher than the average pressure of ordinary osteons.

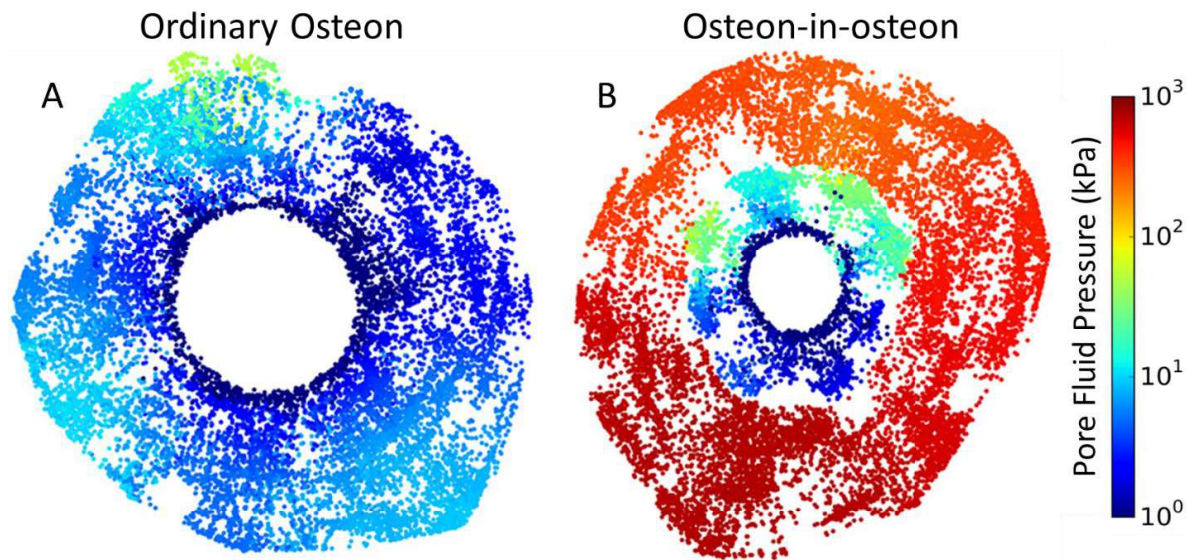


Fig. 4.14. In our model of load-induced fluid flow, the fluid is forced out of the ordinary osteon (A) and osteon-in-osteon (B), similarly to how water is squeezed out of a steadily compressed sponge (i.e. constant strain rate). Pressure pattern images were made by plotting color coded spheres at the location of each node of the network for a representative ordinary osteon (A) and osteon-in-osteon (B). The difference in pressure patterns between the two osteon types is a direct result of a difference in LCN topology. The much higher pressure in the osteon-in-osteon is caused by a combination of the higher fluid flow velocity and the much lower intrinsic permeability of this osteon-in-osteon.

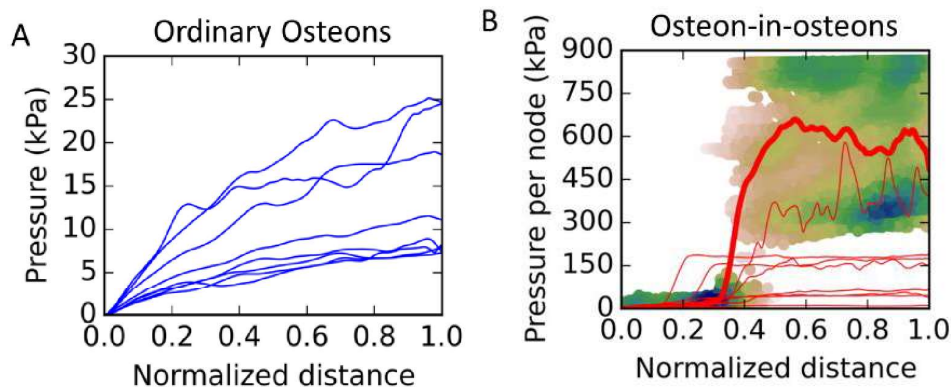


Fig. 4.15. Pressure profiles plotted as a function of the normalized distance (Haversian canal = 0, cement line = 1). First, the profiles were obtained by presenting for each node the values of its position (i.e. normalized distance) and its pressure. Secondly, the data of all nodes in this scatter plot (plot not shown) were transformed in the shown profiles by using a local regression algorithm (locally weighted scatterplot smoothing, LOWESS). A) The pressure profile for all 8 ordinary osteons; B) shows pressure profiles for all 9 osteon-in-osteons. The color code in the background indicates the density of data points of the scatter plot for the osteon-in-osteons of Fig. 14 B. The corresponding LOWESS fit is shown by the thicker red line. This kind of representation was chosen to highlight the spatial heterogeneity of the pressure distribution in this case, which can be only poorly rendered by a LOWESS fit.

4.2.4. Discussion of the Human Osteonal Bone Study

The aim of the second project in my PhD work was to predict the mechanoresponsiveness of different osteon types based on differences in calculated load induced fluid flow patterns (van Tol, Roschger et al. 2020). At older age mechanoresponsiveness is impaired as observed in earlier studies by Razi, Birkhold et al. (2015) and is one of the biggest challenges in medicine. Changes in the responsiveness of bone are often addressed on the cellular and subcellular level by elucidating signaling pathways from the cell membrane to the nucleus and back (Chen, Liu et al. 2010, Jacobs, Temiyasathit et al. 2010). However, a general characteristic of mechanosensing is the integration of the multiple length scales to amplify the stimulus signal and to improve its fidelity. As we have concluded in the mouse tibia project of my PhD work, it is important to not focus entirely on the biology of osteocytes and the interaction with each other, but also to consider the flow of the interstitial fluid through the LCN. It is known that osteon-in-osteons are one of the products of remodeling, where the inner zone is newly formed bone (Tomes and De Morgan 1853, Ericksen 1991, Arhatari, Cooper et al. 2011, Maggiano, Maggiano et al. 2016, Andreasen, Delaisse et al. 2018, Raguin and Streeter 2018). Therefore, osteon-in-osteons are more common at older age and we assume that their altered LCN architecture plays an important role in aging of human bone.

Several studies have explored the effect of an idealized LCN network topology on fluid flow in bone. Not only the topology of single canaliculi (e.g. tortuosity) has been taken into account

4.2. Results of the Human Osteonal Bone Study

(Lemaire, Lemonnier et al. 2012), but also the influence of an idealized network connectivity has been studied (Steck and Tate 2005, Anderson, Kreuzer et al. 2008). New developments in the field of confocal microscopy and image analysis make it possible to image the topology of LCN networks in macroscopic bone volumes reliably (Repp, Kollmannsberger et al. 2017). The use of network data obtained in this way allowed us to study the fluid flow through realistic canalicular networks of full cross sections of human osteons.

For the mechanobiological interpretation of our results Fig. 4.13 is the key. It shows which percentage of the canaliculi in the different types of osteons is stimulated by the fluid shear stress. For the range of shear forces that were reported to elicit osteogenic responses in osteocyte-like cells in *in vitro* studies (Smalt, Mitchell et al. 1997, Bakker, Soejima et al. 2001), the cumulative probability distributions are very similar for ordinary osteons and osteon-in-osteons. However, the conclusion that osteon type does not matter for mechanosensation is premature for several reasons. (i) Simulated fluid flow velocities in the osteon-in-osteons are considerably higher than the fluid flow velocities we found in the mouse tibia study. It is therefore unclear from our results whether osteocytes could be “overstimulated”, i.e. their mechanosensitivity would again decrease for increasing shear forces. *In vitro* experiments have been often performed in an artificial setting with cells adhering to plane surfaces. Progress has been made by performing such experiments with osteocyte-like cells (Lu, Huo et al. 2012). Using a genetically encoded fluorescent calcium indicator, recently it was shown that specific bending strains and frequencies elicited calcium spikes in mouse osteocytes. However, the intensity of the cellular response did not change when the load was further increased (Lewis, Frikha-Benayed et al. 2017). (ii) Important for the interpretation of Fig. 4.11 is how the signals of individual osteocytes are integrated to an effective signal controlling osteoblast and osteoclast action on the cortical bone surfaces, millimeters away from the osteons (Mullender, Huiskes et al. 1994, Huiskes 2000). From the mouse study we can argue that osteocytes closer to the bone surface should contribute more to the integral signal. However, there are often significant differences between the biology of mouse and human cells. An alternative hypothesis to this is that individual osteocytes which experience the highest stimuli play a dominant role in the mechanoreponse (Hartmann, Dunlop et al. 2011). (iii) Like in most mechanobiological models, some of the input parameters (listed in table 3.1) are very challenging to measure and therefore, are not sufficiently well characterized. As an example, the structure of the fibrous matrix in the pericellular space is not sufficiently known and, as a consequence, the value of the permeability of the pericellular space described by the parameter $k_{p,eff}$ has some uncertainty (Sansalone, Kaiser et al. 2013). As $k_{p,eff}$ occurs as a proportionality factor between the pressure difference and the average velocity in the canaliculus, effects are linear, i.e. a 10% increase in $k_{p,eff}$ would cause a 10% decrease in the fluid pressure. (iv) Most important, the shear stresses for the two osteon types are only very similar for the chosen strain rate of $\dot{\epsilon} = 0.015 \text{ s}^{-1}$, which corresponds to vigorous exercise like running. For more everyday physical activities like walking the corresponding strain rate is about a factor of five lower (Lanyon, Hampson et al. 1975, Milgrom, Finestone et al. 2002, Al Nazer, Lanovaz et al. 2012). For comparison, the dashed line

in Fig. 4.13 represents the cumulative probability distributions for this more moderate loading on bone. In case of walking and other physical activities of even lower loads the large majority of osteocytic cell processes in ordinary osteons would not receive sufficient stimulation to elicit an osteogenic response. In osteon-in-osteons the fluid flow through roughly 31% of the canaliculi is still fast enough to overcome the stimulation threshold for osteocytic mechanotransduction. For moderate loading the strain amplification mechanism via load-induced fluid flow is more efficient in osteon-in-osteons. Considering that the frequency of osteon-in-osteons increases with age (Eriksen 1991, Yoshino, Imaizumi et al. 1994), it can be speculated that this formation of more osteon-in-osteons is a potential mechanism to compensate for a general debilitation of the mechanosensing mechanisms.

The opaqueness of the human bone limits the imaging depth to about 35 μm . This limitation in the dimensions of the imaging volume should have only minor consequences on the results of our study, since the LCN shows only a reduced structural heterogeneity in the direction perpendicular to the imaging plane compared to the much more pronounced heterogeneity within the imaging plane, particularly, in the radial direction towards the Haversian canal. We paid attention that the axial directions of the imaged osteons were perpendicular to the imaging plane by only selecting osteons where the Haversian canals appeared circular and straight along the z-axis. Additionally, the selected osteons were not close to Volkmann's canals and other structural features, which could influence the network topology in the direction perpendicular to the imaging plane. Previous studies could not show substantial differences in LCN structures between individuals (Repp, Kollmannsberger et al. 2017, Weinkamer, Kollmannsberger et al. 2019). Therefore, the limitation of using one human specimen for all the analysis should have no major impact on the main conclusions of our work.

A limitation of the human osteon study is that we abstain from an intricate biomechanical description of the loading, but again assume a homogeneous strain rate, as it is often found to be a main determinant of fluid flow velocity in the LCN. To assume a homogeneous strain is reasonable, due to the limited impact of the low porosity ($\sim 1\%$) of the osteon (Yoon and Cowin 2008). In the presented data we neglected the difference in the compressibility of the solid and fluid phases, which could limit the values of the pore pressure (Cowin 1999). To investigate this influence, we therefore extended the model to include a saturation pressure. This allowed us to test the robustness of our results regarding the assumption that the pericellular fluid is incompressible.

To study the robustness of our modeling approach, the volumetric fluid flow sources (f in methods, eq. 3.8) in the osteons were limited by utilizing non-ideal Norton's equivalent current sources (Johnson 2003). In these sources the fluid output is limited as the fluid pressure reaches a defined saturation pressure to take into consideration the compressibility of the interstitial bone fluid under high pressures. Limiting conductors with conductivity C_{lim} were introduced in parallel with the

4.2. Results of the Human Osteonal Bone Study

ideal volumetric flow sources f_i in each node i . As a result, the limited volumetric flow f_{lim} goes to zero when the pressure p approaches the saturation pressure p_{max} ,

$$C_{lim,i} = f_i/p_{max} \quad (4.1)$$

and, therefore,

$$f_{lim,i} = f_i - p_i \cdot C_{lim,i} = f_i \left(1 - \frac{p_i}{p_{max}}\right). \quad (4.2)$$

Thus, the maximum possible pressure in the osteon is equal to the saturation pressure. Due to the already lower values of the occurring pore pressures in the ordinary osteon, the choice of the saturation pressure has hardly any effect on the average fluid velocity when chosen above 1000 kPa (Fig. 4.16 A). The maximum possible pressure in human osteons is estimated to be 12% to 18% of the applied stress (Weinbaum, Cowin et al. 1994, Zhang, Weinbaum et al. 1998). Under stresses during exercise the saturation pressure is, therefore, likely to be above 5000 kPa (Jonkers, Sauwen et al. 2008, Al Nazer, Lanovaz et al. 2012). For a saturation pressure of 5000 kPa this would result in a reduction of the average fluid flow velocity by 11% for osteon-in-osteons. Taking for comparison the osteon-in-osteon with the largest values of the pore pressure, the fluid flow and pressure patterns are still qualitatively very similar. The resulting pressure pattern obtained for a saturation pressure of 5000 kPa is indistinguishable from the one shown in Fig. 4.14 D when the same scale is used.

This saturation pressure had no significant influence on the outcomes, even when applied to the osteon-in-osteon which showed the highest fluid pressure. Also, poroelastic models of osteons showed that a limitation of the pressure only has a limited effect on the fluid flow velocity (Remond, Naili et al. 2008, Yoon and Cowin 2008).

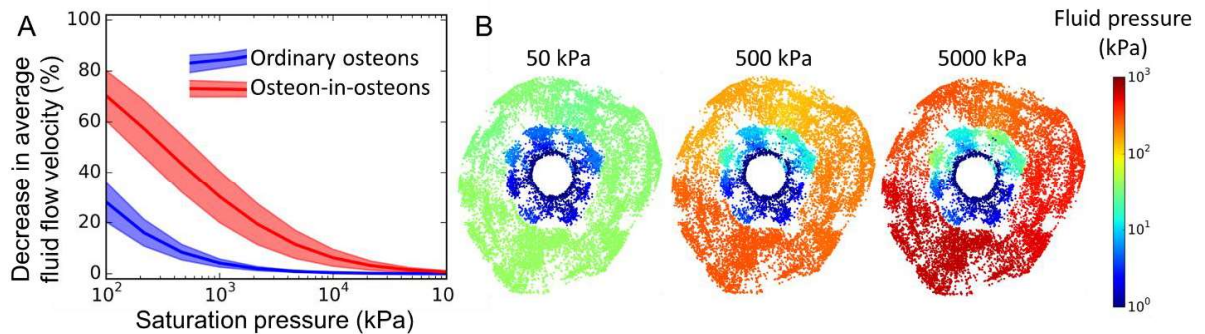


Fig. 4.16. The effect of a pressure limitation on the average fluid flow velocity in ordinary osteons (blue) and osteon-in-osteons (red). A) The relative reduction of the average fluid flow velocity is plotted as

function of the saturation pressure. The shaded region denotes the standard deviation. B) The pressure pattern with saturation pressures of 50 kPa, 500 kPa and 5000 kPa, respectively.

In our study we modeled the cement line as an impermeable boundary. Based on reports on canaliculi crossing the cement line (Curtis, Ashrafi et al. 1985), particularly in younger individuals (Milovanovic, Zimmermann et al. 2013), the influence of a “leaking” cement line was systematically studied.

To study the sensitivity of the model for a leaking cement line, a total leakage flow was added to the volumetric fluid flow sources f of only the cement line nodes:

$$f_i = f_i + \frac{\text{total cement line leakage}}{\text{number of cement line nodes}} \quad (\text{eq 4.3})$$

Since the direction of the flow at the cement line is unknown, we simulated both possibilities, i.e. leakage into and out of the osteon (positive and negative leakage, respectively). The volumetric leakage flow was defined as a percentage of the total volumetric flow into the Haversian canal of the osteon. For example, with a leakage of 5% and a total volumetric flow into the Haversian canal of $100 \mu\text{m}^3/\text{s}$, the ‘total cement line leakage’ would be $5 \mu\text{m}^3/\text{s}$. Both osteon types keep their characteristic pressure patterns in these simulations, as demonstrated by the pressure plots in Fig. 1.17 A. An approximately linear effect was detected between the amount of fluid leaking through the cement line and the average pressure and fluid flow (Fig. 1.17 B), while the characteristic pressure and flow patterns of the osteons types were maintained (Fig. 1.17 A). Moreover, since realistic values of leakage are likely below 1%, the consideration of a leaking cement line does not change our conclusions concerning the difference between ordinary osteons and osteon-in-osteons.

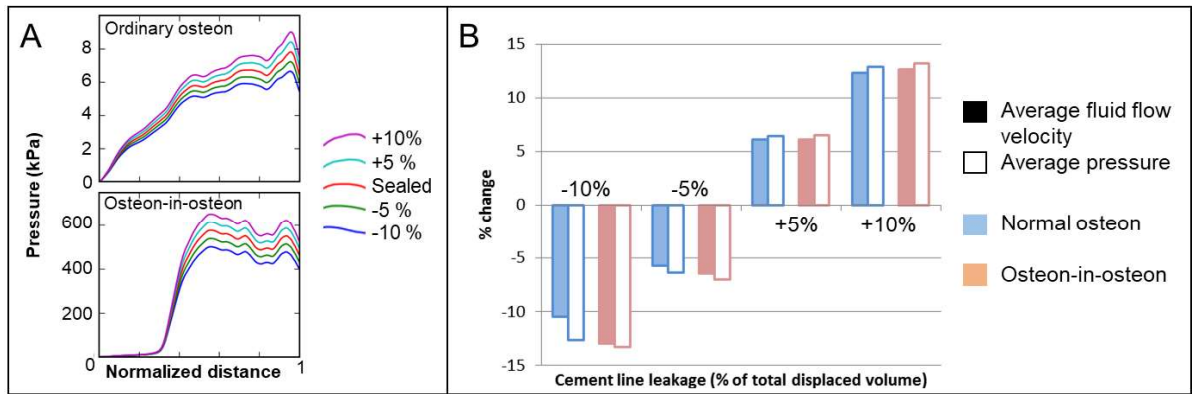


Fig. 4.17. Consideration of a leaking cement line in the model A) Pressure profiles plotted as function of the normalized distance. As in Fig. 4.15 the distance is normalized so that Haversian canal = 0, cement line = 1. Four different cases of cement line leakage (all severe cases of leakage) were compared to the impermeable cement line (red line). B) The relative impact of the four leakage scenarios on average fluid flow velocity and pressure in the two representative osteons from Fig. 4.10, quantified as %change from the reference case of an impermeable cement line.

4.2. Results of the Human Osteonal Bone Study

5. CONCLUSION AND OUTLOOK

The fluid flow hypothesis states that load-induced fluid flow through the lacunocanalicular network (LCN) is the most important stimulus for osteocytes, as the deformations of the stiff bone are too small to be sensed directly. The objective of this PhD thesis was to test the hypothesis that the architecture of the LCN is a strong contributor to the load-induced fluid flow pattern, and therefore important for the mechanoresponsiveness of bone. We approach the LCN as the hardware, which is responsible for amplification of the mechanical signals, while the biochemical processes in the cells is the software that decides how the bone should be adapted. The ‘decision’ is then signaled to the surfaces of bones, in order to recruit the cells that do the bone formation and resorption work.

By measuring the network architecture, the properties of millions of the LCN components at the microscale were experimentally obtained, while computational techniques were applied to estimate the load-induced fluid flow. A strong heterogeneity was observed in all fluid flow patterns, which stresses the importance of taking the LCN architecture into account. Since we obtained fluid flow patterns in such fine detail, the quality of the images was found to be essential for obtaining adequate fluid flow patterns. Cracks, which very easily form during sample preparation, as well as movement artefacts in the microscopic images, lead to artefacts in the fluid flow patterns. A big advantage of performing both the imaging and the computational analysis of the network by myself is that I could detect this difficulty early. With the observed problems in mind I could repeat the imaging experiments of the LCN to create the three high quality datasets.

Based on the comparison with measured mechanoresponses in mice, we concluded that the fluid flow was a better predictor of the bone mechanoresponse than strain, especially at the periosteal surface. The calculated load-induced fluid flow velocities could more accurately predict where formation and resorption occurred, and we could even predict the thickness of the newly formed bone. Additionally, the mouse with the lowest fluid flow velocity had a thinner layer of newly formed bone compared to the other mice. In contrast, we did not observe most of the bone formation near the surfaces of highest strain. Moreover, the strain patterns in the three mice were very similar, and therefore, could not explain the differences in mechanoresponse between mice.

Due to the extensive characterization of the LCN we could qualitatively explain how the fluid flow was differently influenced by local differences in network architecture and what the role of individual blood vessels was. Fluid flow likes to take the path of least resistance. When vascular canals are connected to part of the LCN, which has a poor connection to the bone surface, then the path of least resistance leads to the vascular canals. This shields this surface of the bone from the fluid flow and therefore, is less mechanoresponsive. In contrast, fluid could be accelerated if a tree-like network funnels the flow in fewer canaliculi. These tree-like networks were more

pronounced near more mechanosensitive surfaces. This stresses that for a full understanding of bone mechanoresponse of bone, the LCN architecture cannot be neglected.

The LCN architecture of mouse and human bone are fundamentally different. Human cortical bone contains secondary osteons of two types: (i) ordinary osteons, with a continuous network architecture, and (ii) osteon-in-osteons. Fluid flow patterns indicated that the osteon-in-osteons are the more mechanosensitive of the two. We also can observe here the role of the network architecture, as average fluid flow velocity shows direct proportionality with the average shortest path length. We concluded that longer paths have a larger pore volume (i.e. contain more fluid) that must be drained into the Haversian canal, which leads to higher velocities in longer paths.

The research strategy that was successfully applied in this thesis for mouse bone and human healthy bone, has high potential for future research. As most promising future research projects, the following list comes to mind:

- Pathological LCN architectures

This PhD thesis focused on the mechanoresponse in healthy tissues, since there was almost no basic knowledge of the impact of the LCN architecture on the mechanoresponse of bone. Genetically altered mice are commonly used to study diseases. We are currently investigating mice presenting premature aging, which do not show a mechanoresponse. As an altered LCN architecture was observed, we collaborate to investigate the link between this abnormal LCN architecture and the compromised mechanoresponse.

- Different Skeletal sites

It would also be interesting to investigate what the roles of different network architectures are in different types of bone. Can we for example explain what the role of the osteocyte network is in bones with a different mechanoresponsiveness, such as the skull? It is mostly just speculated how changes in the LCN architecture influence the functionality of the osteocyte network in cases of diseases. Investigations into the connectome will help to lead into new insights.

- model refinement - compressibility of fluid

In the used model approach, I assumed that a steady fluid flow velocity is reached, which is directly proportional to the strain rate. However, this assumption is not realistic in cases of very high pressure or for high loading frequencies. For small deformations, it is often assumed that the relationships between stress and strain are linear. Introducing effective stiffness of the pore (E) allows us to use a linear equation to relate with pore fluid pressure (P) and change in pore volume (ΔV).

$$P(t) = -E \cdot \Delta V(t) . \quad (5.1)$$

The effective stiffness E can be determined via different models. One could go into detail and use a FEM model to calculate it for each individual lacuna, or one could for example adapt the simplified poroelastic model by Cowin et al.

Due to the direct linear relationships this can be modeled in a similar way as a capacitor, representing the effective stiffness (Fig. 5.1). The pore volume changes due to strain can also here be modeled as an ideal volumetric flow source, similarly to what I did in my PhD study:

$$\frac{dV}{dt} = -\dot{\epsilon}(t) \cdot V_0 . \quad (5.2)$$

Here V_0 is the volume at rest (i.e. zero pressure and zero strain). The volume change due to compression of the fluid is then represented by the volume change in the capacitor, while the volume change due to fluid displacement would flow through the two connection points in the right (Fig. 5.1). This circuit behaves like a low pass filter, where the output flow is attenuated at higher frequencies and the phase of the output flow lags behind that of the volume change.

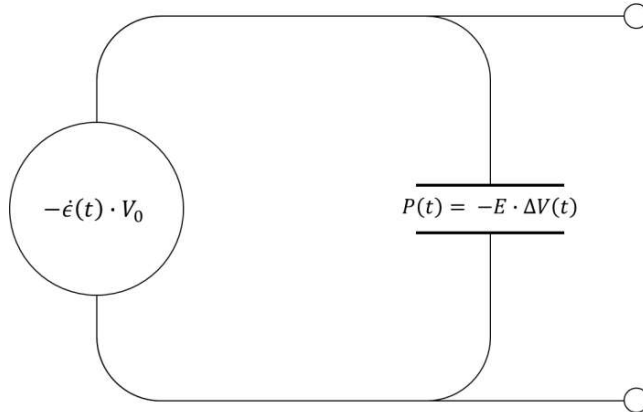


Fig. 5.1. A model of a network pore which takes the compressibility of fluid into account by introducing a capacitor which is placed parallel to the earlier used ideal fluid flow source.

To solve a network with these fluid flow sources one can make use of the Laplace transformation, which is commonly used to solve alternating currents and voltages in electrical networks of resistors, capacitors and inductors. This inertia of the fluid could be modeled as an inductor. In this analogy the phase angle of the flow that lags behind the pressure models the pressure gradient which slowly accelerates the fluid due to its mass. In short, this results in a set of linear equations with complex numbers, where the magnitude is the fluid flow velocity and the argument represents the phase angle between strain rate and flow. This improved model can be used to explore how bone reacts to different frequencies, as well as how energy is dissipated in the system. When flow is going through a ‘capacitor’ it is stored as mechanical energy, which is released when the flow reverses. However, when the flow is flowing through ‘resistors’ the energy is lost.

- Diffusion and convection

Tracer experiments are often mentioned as proof of fluid flow through the LCN. However, very simple models are used to calculate the fluid flow velocity from measured tracer concentrations. Transport of tracers happens spontaneously via diffusion (see for example our rhodamine staining) and load-induced fluid flow increases the velocity of the tracer. Therefore, including diffusion of molecules in network models would also contribute to the biological field. In Fig. 5.2 I show a proof of concept, where Markov chains were used to calculate how a substance diffuses from the Haversian canal into the different osteons. A discrete time Markov chain is a commonly used stochastic model describing a sequence of possible events, for example, the possibility for a substance to move from node to node via the canaliculi. In this example the Markov chain models a random walk by defining the possibility of a substance to make a random step through the LCN in the transition matrix \mathbf{P} . The probability P_{ij} to step from node i to node j depends on the connectivity of the LCN (if i and j are connected) as well as the length of canaliculi. The initial state of the model, for example the concentration in the nodes, is defined by a state matrix \mathbf{S}_0 . After each step the state is multiplied to reach the next state. The state \mathbf{S}_N after N steps is defined as

$$\mathbf{S}_N = \mathbf{S}_0 \cdot \mathbf{P}^N. \quad (5.3)$$

Note that the probability to step from node i to node j can be different than to step from node j to node i , which can be used to introduce a bias to simulate for example convection.

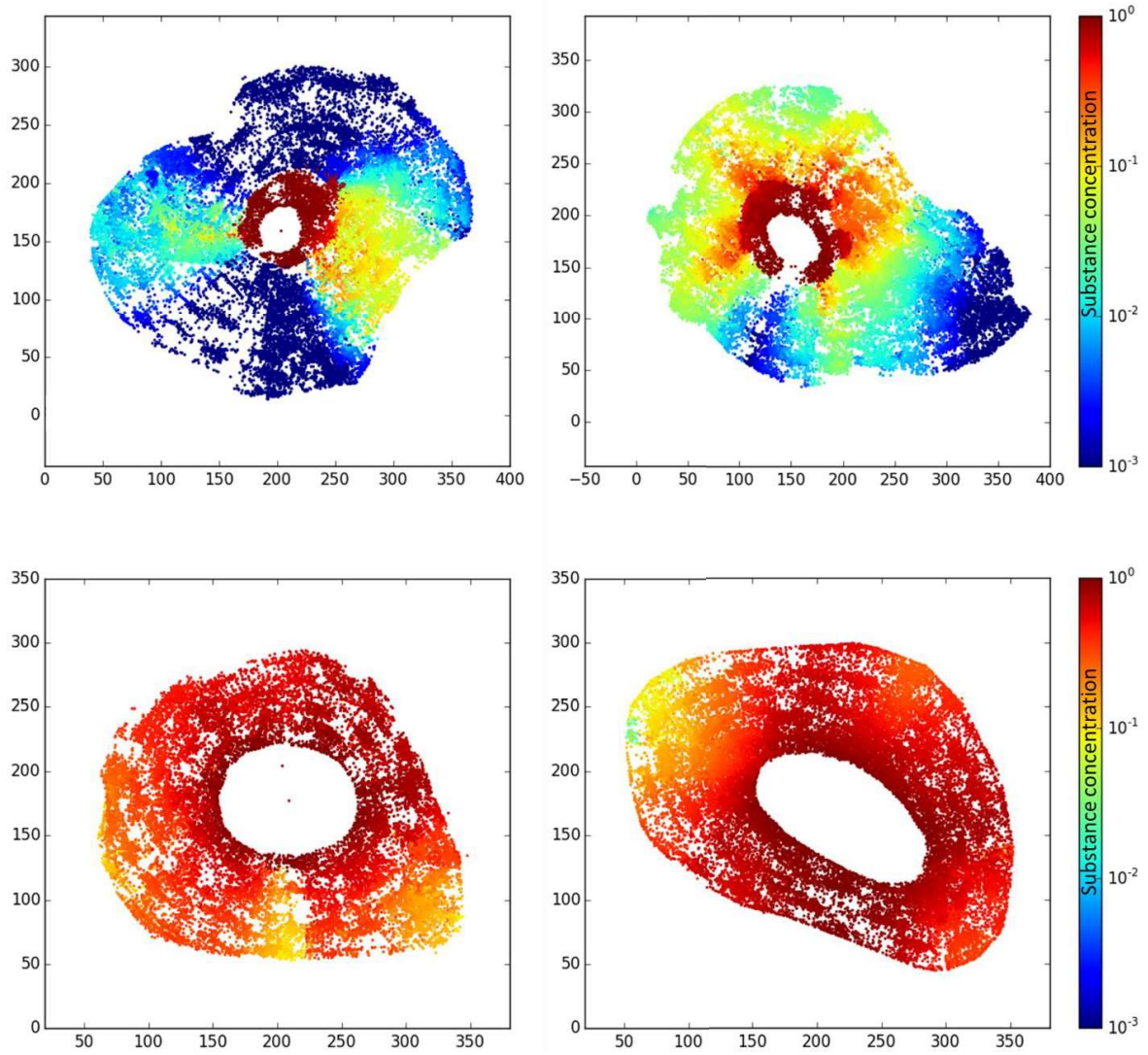


Fig. 5.2. Proof of concept of the Markov chain approach to model diffusion through the LCN of osteon-in-osteons (top) and ordinary osteons (bottom). The color indicates the concentration of the imaginary substance in the nodes after 650 time steps. The x and y axis indicate the position in μm . The dots in the Haversian canal of the left figures are special nodes, which connects all canaliculi which enter the Haversian canal. In other plots these nodes are hidden.

5.1. Additional Projects During my PhD Time

During my PhD study I was involved in several other projects in the bone-related research. This section is a short summary of these projects highlighting my contributions.

Mineral homeostasis is important for the health of most of our organs. Due to the density of the LCN 80% of the bone mineral is within 2 μm of the canaliculi. This, in combination with the excellent connectivity of the LCN, would make the LCN wall a good candidate for a vast mineral reservoir. Therefore, we spatially correlated the LCN architecture with the local bone mineral density. We observed a positive correlation between the local canalicular density and local mineral density, i.e. an accumulation of mineral has occurred at dense network regions (Roschger, Roschger et al. 2019). Note that if mineralization was independent of the LCN, we would have observed an inverse correlation due to the increased porosity. The spatial correlation therefore suggests a direct impact of the osteocytes to the mineralization process of newly formed bone.

The mice I work on are used in the project of a PhD student (Victoria Schemenz) in the group of Wolfgang Wagermaier. There have been several studies that related the osteocyte LCN to material properties of the bone near the canaliculi, but it was not yet done in a full cross section of the mouse bone. One of the measurements I did not cover in my thesis, second harmonic imaging of the collagen in our mouse tibiae, gives an indication of the collagen orientation (Repp, Kollmannsberger et al. 2017). This data will be covered by the PhD thesis of Victoria in the part where the properties of the network, the collagen orientation and properties of mineral crystals will be correlated. The mineral crystal dimensions and orientation were measured using synchrotron SAX and WAX diffraction studies. We measured the diffraction in the PETRA III beamline in DESY, Hamburg. From this data she could identify different types of bone (i.e. new, lamellar and woven) as well as some mineralized cartilage.

Halfway in my PhD study, our institute got a new state-of-the-art imaging instrument, a scanning electron microscope (SEM) equipped with a focused ion beam (FIB) to mill the surface specimen with high precision. This allows for nanometer resolution imaging in 3D. We suggested several projects which would benefit from this instrument. The nanometer resolution would for example be well suited to image the diameter of canaliculi. How wide are the bridging canaliculi for example? Moreover, the SEM shows a strong contrast between mineralized bone and organic extracellular matrix. Therefore, this is an excellent tool to study the effect of canaliculi on mineralization. PhD student Mahdi Ayoubi measured the mineralization zone in a large number of newly forming human osteons at 4 nm resolution and segmented the canalicular network in these datasets. I supported the image analysis by writing a python script to perform spatial correlation between the canaliculi and the degree of mineralization. When Mahdi performed the correlation, he observed that newly formed bone tends to mineralize significantly slower in the vicinity of canaliculi. 'Far' away from canaliculi (in the micrometer scale) the mineralization seems independent of the canaliculi. This indicates that canaliculi are locally actively preventing mineralization in very young bone.

We collaborate with PhD student Chloé Lerebours and Dr. Pascal Buenzli to study the interplay between bone fatigue, remodeling and mineralization in a model of trabecular bone. The model was developed during a research stay at Monash University, Melbourne, in January/February 2017. The hypothesis in this study is that fatigue stimulates the resorption of bone, and therefore influences the remodeling rate. Changes in remodeling can be detected from changes in the bone mineral density distribution (BMDD). Therefore, we calibrate the model with measured BMDDs. Although work is still in progress, we observed that it is possible that bone fatigue regulates the remodeling rate, based on the resulting BMDD. We can also simulate why after sudden extreme exercise the bone volume first decreases, before the bone adapts to the increased load by increasing the amount of bone.

The difference in canalicular density between mouse and human bone is strong. Therefore, it seems possible to distinguish between these two types of bone. This observation was used by the group of Dr. Amaia Cipitria. In a study on so called ‘humanized mice’ (Science Advances, submitted) I helped to obtain the canalicular density and lacunar volume to distinguish between human and mouse bone. By comparing these parameters with immunological staining, we concluded that the LCN can indeed be used to identify human bone tissue within a mouse. Also in a second study by this group I helped with the quantification of the LCN parameters (Ziouti, Soares et al. 2020).

In a collaboration with Uwe Kornak, Charité University Hospital, Berlin we work on the disease geroderma osteodysplastica. It is characterized by early-onset osteoporosis due to early aging. When *GORAB*, the responsible disease gene, is knocked out in mice they show strong changes in their LCN. The canalicular density decreases and the vascular porosity increases. Based on the conclusions of my thesis we can hypothesize that these changes in the lead to a decreased mechanoresponsiveness.

5. Conclusion and Outlook

6. REFERENCES

- Al Nazer, R., J. Lanovaz, C. Kawalilak, J. D. Johnston and S. Kontulainen (2012). "Direct in vivo strain measurements in human bone-A systematic literature review." Journal of Biomechanics **45**(1): 27-40.
- Anderson, E. J., S. Kaliyamoorthy, J. I. D. Alexander and M. L. K. Tate (2005). "Nano-microscale models of periosteocytic flow show differences in stresses imparted to cell body and processes." Annals of Biomedical Engineering **33**(1): 52-62.
- Anderson, E. J., S. M. Kreuzer, O. Small and M. L. K. Tate (2008). "Pairing computational and scaled physical models to determine permeability as a measure of cellular communication in micro- and nano-scale pericellular spaces." Microfluidics and Nanofluidics **4**(3): 193-204.
- Anderson, E. J. and M. L. K. Tate (2008). "Idealization of pericellular fluid space geometry and dimension results in a profound underprediction of nano-microscale stresses imparted by fluid drag on osteocytes." Journal of Biomechanics **41**(8): 1736-1746.
- Andreasen, C. M., J. M. Delaisse, B. C. J. van der Eerden, J. P. T. M. van Leeuwen, M. Ding and T. L. Andersen (2018). "Understanding Age-Induced Cortical Porosity in Women: The Accumulation and Coalescence of Eroded Cavities Upon Existing Intracortical Canals Is the Main Contributor." Journal of Bone and Mineral Research **33**(4): 606-620.
- Arhatari, B. D., D. M. L. Cooper, C. D. L. Thomas, J. G. Clement and A. G. Peele (2011). "Imaging the 3D structure of secondary osteons in human cortical bone using phase-retrieval tomography." Physics in Medicine and Biology **56**(16).
- Bacabac, R. G., T. H. Smit, M. G. Mullender, S. J. Dijcks, J. J. W. A. Van Loon and J. Klein-Nulend (2004). "Nitric oxide production by bone cells is fluid shear stress rate dependent." Biochemical and Biophysical Research Communications **315**(4): 823-829.
- Bakker, A. D., K. Soejima, J. Klein-Nulend and E. H. Burger (2001). "The production of nitric oxide and prostaglandin E-2 by primary bone cells is shear stress dependent." Journal of Biomechanics **34**(5): 671-677.
- Beno, T., Y. J. Yoon, S. C. Cowin and S. P. Fritton (2006). "Estimation of bone permeability using accurate microstructural measurements." Journal of Biomechanics **39**(13): 2378-2387.
- Birkhold, A. I., H. Razi, G. N. Duda, R. Weinkamer, S. Checa and B. M. Willie (2014). "Mineralizing surface is the main target of mechanical stimulation independent of age: 3D dynamic in vivo morphometry." Bone **66**: 15-25.
- Birkhold, A. I., H. Razi, R. Weinkamer, G. N. Duda, S. Checa and B. M. Willie (2015). "Monitoring in vivo (re)modeling: A computational approach using 4D microCT data to quantify bone surface movements." Bone **75**: 210-221.
- Bonewald, L. F. (2011). "The Amazing Osteocyte." Journal of Bone and Mineral Research **26**(2): 229-238.
- Buenzli, P. R. (2015). "Osteocytes as a record of bone formation dynamics: A mathematical model of osteocyte generation in bone matrix." Journal of Theoretical Biology **364**: 418-427.
- Buenzli, P. R. and N. A. Sims (2015). "Quantifying the osteocyte network in the human skeleton." Bone **75**: 144-150.
- Burger, E. H., J. Klein-Nulend and T. H. Smit (2003). "Strain-derived canalicular fluid flow regulates osteoclast activity in a remodelling osteon - a proposal." Journal of Biomechanics **36**(10): 1453-1459.
- Burr, D. B., R. B. Martin, M. B. Schaffler and E. L. Radin (1985). "Bone Remodeling in Response to In vivo Fatigue Microdamage." Journal of Biomechanics **18**(3): 189-200.
- Cabahug-Zuckerman, P., R. F. Stout, R. J. Majeska, M. M. Thi, D. C. Spray, S. Weinbaum and M. B. Schaffler (2018). "Potential role for a specialized (3) integrin-based structure on osteocyte processes in bone mechanosensation." Journal of Orthopaedic Research **36**(2): 642-652.
- Cardoso, L., S. P. Fritton, G. Gailani, M. Benalla and S. C. Cowin (2013). "Advances in assessment of bone porosity, permeability and interstitial fluid flow." Journal of Biomechanics **46**(2): 253-265.

6. References

- Carriero, A., A. F. Pereira, A. J. Wilson, S. Castagno, B. Javaheri, A. A. Pitsillides, M. Marenzana and S. J. Shefelbine (2018). "Spatial relationship between bone formation and mechanical stimulus within cortical bone: Combining 3D fluorochrome mapping and poroelastic finite element modelling." Bone Reports **8**: 72-80.
- Carter, Y., C. D. L. Thomas, J. G. Clement and D. M. L. Cooper (2013). "Femoral osteocyte lacunar density, volume and morphology in women across the lifespan." Journal of Structural Biology **183**(3): 519-526.
- Chen, J. H., C. Liu, L. D. You and C. A. Simmons (2010). "Boning up on Wolff's Law: Mechanical regulation of the cells that make and maintain bone." Journal of Biomechanics **43**(1): 108-118.
- Cowin, S. C. (1999). "Bone poroelasticity." Journal of Biomechanics **32**(3): 217-238.
- Cowin, S. C. and L. Cardoso (2015). "Blood and interstitial flow in the hierarchical pore space architecture of bone tissue." Journal of Biomechanics **48**(5): 842-854.
- Curtis, T. A., S. H. Ashrafi and D. F. Weber (1985). "Canalicular Communication in the Cortices of Human Long Bones." Anatomical Record **212**(4): 336-344.
- Cuthill, E. and J. McKee (1969). "Reducing the bandwidth of sparse symmetric matrices." Proceedings of the 1969 24th national conference: 157-172.
- Dallas, S. L., M. Prideaux and L. F. Bonewald (2013). "The Osteocyte: An Endocrine Cell . . . and More." Endocrine Reviews **34**(5): 658-690.
- Dong, P., S. Hauptert, B. Hesse, M. Langer, P. J. Gouttenoire, V. Bousson and F. Peyrin (2014). "3D osteocyte lacunar morphometric properties and distributions in human femoral cortical bone using synchrotron radiation micro-CT images." Bone **60**: 172-185.
- Ericksen, M. F. (1991). "Histologic Estimation of Age at Death Using the Anterior Cortex of the Femur." American Journal of Physical Anthropology **84**(2): 171-179.
- Fratzl, P., H. S. Gupta, E. P. Paschalis and P. Roschger (2004). "Structure and mechanical quality of the collagen-mineral nano-composite in bone." Journal of Materials Chemistry **14**(14): 2115-2123.
- Fratzl, P. and R. Weinkamer (2007). "Hierarchical Structure and Repair of Bone: Deformation, Remodelling, Healing." Self Healing Materials: An Alternative Approach to 20 Centuries of Materials Science **100**: 323-335.
- Frost, H. M. (1987). "Bone Mass and the Mechanostat - a Proposal." Anatomical Record **219**(1): 1-9.
- Frost, H. M. (2003). "Bone's mechanostat: A 2003 update." Anatomical Record Part a-Discoveries in Molecular Cellular and Evolutionary Biology **275a**(2): 1081-1101.
- Gatti, V., E. M. Azoulay and S. P. Fritton (2018). "Microstructural changes associated with osteoporosis negatively affect loading-induced fluid flow around osteocytes in cortical bone." Journal of Biomechanics **66**: 127-136.
- Genthial, R., M. Gerbaix, D. Farlay, L. Vico, E. Beaupaire, D. Debarre and A. Gourrier (2019). "Third harmonic generation imaging and analysis of the effect of low gravity on the lacuno-canalicular network of mouse bone." Plos One **14**(1): e0209079.
- Geoghegan, I. P., D. A. Hoey and L. M. McNamara (2019). "Integrins in Osteocyte Biology and Mechanotransduction." Current Osteoporosis Reports **17**(4): 195-206.
- Goulet, G. C., D. Coombe, R. J. Martinuzzi and R. F. Zernicke (2009). "Poroelastic Evaluation of Fluid Movement Through the Lacunocanalicular System." Annals of Biomedical Engineering **37**(7): 1390-1402.
- Grady, L. J. and J. R. Polimeni (2010). Discrete calculus: Applied analysis on graphs for computational science, Springer Science & Business Media.
- Guo, D. and L. F. Bonewald (2009). "Advancing our understanding of osteocyte cell biology." Therapeutic advances in musculoskeletal disease **1**(2): 87-96.
- Gururaja, S., H. J. Kim, C. C. Swan, R. A. Brand and R. S. Lakes (2005). "Modeling deformation-induced fluid flow in cortical bone's canalicular-lacunar system." Annals of Biomedical Engineering **33**(1): 7-25.

- Hartmann, M. A., J. W. C. Dunlop, Y. J. M. Brechet, P. Fratzl and R. Weinkamer (2011). "Trabecular bone remodelling simulated by a stochastic exchange of discrete bone packets from the surface." Journal of the Mechanical Behavior of Biomedical Materials **4**(6): 879-887.
- Hemmatian, H., A. D. Bakker, J. Klein-Nulend and G. H. van Lenthe (2017). "Aging, Osteocytes, and Mechanotransduction." Current Osteoporosis Reports **15**(5): 401-411.
- Hernandez, C., R. Majeska and M. Schaffler (2004). "Osteocyte density in woven bone." Bone **35**(5): 1095-1099.
- Herskovits, M., I. Singh and H. Sandhu (1990). "Innervation of bone." Bone **3**: 165-186.
- Heyeraas, K. and E. Berggreen (1999). "Interstitial fluid pressure in normal and inflamed pulp." Critical Reviews in Oral Biology & Medicine **10**(3): 328-336.
- Hörl, D., F. R. Rusak, F. Preusser, P. Tillberg, N. Randel, R. K. Chhetri, A. Cardona, P. J. Keller, H. Harz and H. Leonhardt (2018). "BigStitcher: Reconstructing high-resolution image datasets of cleared and expanded samples." bioRxiv: 343954.
- Huiskes, R. (2000). "If bone is the answer, then what is the question?" Journal of Anatomy **197**: 145-156.
- Ip, V., Z. Toth, J. Chibnall and S. McBride-Gagyi (2016). "Remnant Woven Bone and Calcified Cartilage in Mouse Bone: Differences between Ages/Sex and Effects on Bone Strength." Plos One **11**(11).
- Iwaniec, U. T. and R. T. Turner (2016). "Influence of body weight on bone mass, architecture and turnover." Journal of Endocrinology **230**(3): R115-R130.
- Jacobs, C. R., S. Temiyasathit and A. B. Castillo (2010). "Osteocyte Mechanobiology and Pericellular Mechanics." Annual Review of Biomedical Engineering, Vol **12** **12**: 369-400.
- Jager, I. and P. Fratzl (2000). "Mineralized collagen fibrils: A mechanical model with a staggered arrangement of mineral particles." Biophysical Journal **79**(4): 1737-1746.
- Javaheri, B., H. Razi, S. Gohin, S. Wylie, Y. M. Chang, P. Salmon, P. D. Lee and A. A. Pitsillides (2020). "Lasting organ-level bone mechanoadaptation is unrelated to local strain." Science Advances **6**(10): eaax8301.
- Johnson, D. H. (2003). "Origins of the equivalent circuit concept: The current-source equivalent." Proceedings of the IEEE **91**(5): 817-821.
- Jonkers, I., N. Sauwen, G. Lenaerts, M. Mulier, G. Van der Perre and S. Jaecques (2008). "Relation between subject-specific hip joint loading, stress distribution in the proximal femur and bone mineral density changes after total hip replacement." Journal of Biomechanics **41**(16): 3405-3413.
- Kameo, Y., T. Adachi and M. Hojo (2008). "Transient response of fluid pressure in a poroelastic material under uniaxial cyclic loading." Journal of the Mechanics and Physics of Solids **56**(5): 1794-1805.
- Kameo, Y., T. Adachi and M. Hojo (2009). "Fluid pressure response in poroelastic materials subjected to cyclic loading." Journal of the Mechanics and Physics of Solids **57**(11): 1815-1827.
- Kamioka, H., Y. Kameo, Y. Imai, A. D. Bakker, R. G. Bacabac, N. Yamada, A. Takaoka, T. Yamashiro, T. Adachi and J. Klein-Nulend (2012). "Microscale fluid flow analysis in a human osteocyte canaliculus using a realistic high-resolution image-based three-dimensional model." Integrative Biology **4**(10): 1198-1206.
- Katz, L. C. and C. J. Shatz (1996). "Synaptic activity and the construction of cortical circuits." Science **274**(5290): 1133-1138.
- Kerschnitzki, M., P. Kollmannsberger, M. Burghammer, G. N. Duda, R. Weinkamer, W. Wagermaier and P. Fratzl (2013). "Architecture of the osteocyte network correlates with bone material quality." Journal of Bone and Mineral Research **28**(8): 1837-1845.
- Kerschnitzki, M., W. Wagermaier, Y. F. Liu, P. Roschger, G. N. Duda and P. Fratzl (2011). "Poorly Ordered Bone as an Endogenous Scaffold for the Deposition of Highly Oriented Lamellar Tissue in Rapidly Growing Ovine Bone." Cells Tissues Organs **194**(2-4): 119-123.
- Kerschnitzki, M., W. Wagermaier, P. Roschger, J. Seto, R. Shahar, G. N. Duda, S. Mundlos and P. Fratzl (2011). "The organization of the osteocyte network mirrors the extracellular matrix orientation in bone." Journal of Structural Biology **173**(2): 303-311.

6. References

- Klein-Nulend, J. and L. F. Bonewald (2020). The osteocyte. Principles of Bone Biology, Academic Press: 133-162.
- Klein-Nulend, J., A. Vanderplas, C. M. Semeins, N. E. Ajubi, J. A. Frangos, P. J. Nijweide and E. H. Burger (1995). "Sensitivity of osteocytes to biomechanical stress in vitro." Faseb Journal **9**(5): 441-445.
- Kogawa, M., A. R. Wijenayaka, R. T. Ormsby, G. P. Thomas, P. H. Anderson, L. F. Bonewald, D. M. Findlay and G. J. Atkins (2013). "Sclerostin Regulates Release of Bone Mineral by Osteocytes by Induction of Carbonic Anhydrase 2." Journal of Bone and Mineral Research **28**(12): 2436-2448.
- Kollmannsberger, P., M. Kerschnitzki, F. Repp, W. Wagermaier, R. Weinkamer and P. Fratzl (2017). "The small world of osteocytes: connectomics of the lacuno-canalicular network in bone." New Journal of Physics **19**.
- Kumar, R., A. K. Tiwari, D. Tripathi, N. V. Shrivastava and F. Nizam (2019). "Canalicular fluid flow induced by loading waveforms: A comparative analysis." J Theor Biol **471**: 59-73.
- Lanyon, L. E., W. G. Hampson, A. E. Goodship and J. S. Shah (1975). "Bone deformation recorded in vivo from strain gauges attached to the human tibial shaft." Acta Orthop Scand **46**(2): 256-268.
- Leeuwenhoeck, A. (1677). "Microscopical observations of the structure of teeth and other bones: made and communicated, in a letter by Mr. Anthony Leeuwenhoeck." Philosophical Transactions of the Royal Society of London Series I **12**: 1002-1003.
- Lemaire, T., S. Lemonnier and S. Naili (2012). "On the paradoxical determinations of the lacuno-canalicular permeability of bone." Biomechanics and Modeling in Mechanobiology **11**(7): 933-946.
- Lemaire, T., S. Naili and A. Remond (2008). "Study of the influence of fibrous pericellular matrix in the cortical interstitial fluid movement with hydroelectrochemical effects." J Biomech Eng **130**(1): 011001.
- Lewis, K. J., D. Frikha-Benayed, J. Louie, S. Stephen, D. C. Spray, M. M. Thi, Z. Seref-Ferlengez, R. J. Majeska, S. Weinbaum and M. B. Schaffler (2017). "Osteocyte calcium signals encode strain magnitude and loading frequency in vivo." Proceedings of the National Academy of Sciences of the United States of America **114**(44): 11775-11780.
- Lin, Y. and S. Xu (2011). "AFM analysis of the lacunar-canalicular network in demineralized compact bone." Journal of Microscopy **241**(3): 291-302.
- Lu, X. L., B. Huo, M. Park and X. E. Guo (2012). "Calcium response in osteocytic networks under steady and oscillatory fluid flow." Bone **51**(3): 466-473.
- Maggiano, I. S., C. M. Maggiano, J. G. Clement, C. D. L. Thomas, Y. Carter and D. M. L. Cooper (2016). "Three-dimensional reconstruction of Haversian systems in human cortical bone using synchrotron radiation-based micro-CT: morphology and quantification of branching and transverse connections across age." Journal of Anatomy **228**(5): 719-732.
- Main, R. P., M. E. Lynch and M. C. H. van der Meulen (2010). "In vivo tibial stiffness is maintained by whole bone morphology and cross-sectional geometry in growing female mice." Journal of Biomechanics **43**(14): 2689-2694.
- Main, R. P., S. J. Shefelbine, L. B. Meakin, M. J. Silva, M. C. H. van der Meulen and B. M. Willie (2020). "Murine Axial Compression Tibial Loading Model to Study Bone Mechanobiology: Implementing the Model and Reporting Results." Journal of Orthopaedic Research **38**(2): 233-252.
- Marotti, G., M. Ferretti, F. Remaggi and C. Palumbo (1995). "Quantitative-Evaluation on Osteocyte Canalicular Density in Human Secondary Osteons." Bone **16**(1): 125-128.
- McKibbin, B. (1978). "The biology of fracture healing in long bones." The Journal of bone and joint surgery. British volume **60**(2): 150-162.
- Milgrom, C., A. Finestone, N. Sharkey, A. Hamel, V. Mandes, D. Burr, A. Arndt and I. Ekenman (2002). "Metatarsal strains are sufficient to cause fatigue fracture during cyclic overloading." Foot & Ankle International **23**(3): 230-235.

- Milovanovic, P. and B. Busse (2019). "Inter-site Variability of the Human Osteocyte Lacunar Network: Implications for Bone Quality." Current Osteoporosis Reports **17**(3): 105-115.
- Milovanovic, P., E. A. Zimmermann, M. Hahn, D. Djonic, K. Puschel, M. Djuric, M. Amling and B. Busse (2013). "Osteocytic Canalicular Networks: Morphological Implications for Altered Mechanosensitivity." Acs Nano **7**(9): 7542-7551.
- Mosekilde, L., E. N. Ebbesen, L. Tornvig and J. S. Thomsen (2000). "Trabecular bone structure and strength-remodelling and repair." J Musculoskelet Neuronal Interact **1**(1): 25-30.
- Mullender, M. G. and R. Huiskes (1995). "Proposal for the regulatory mechanism of Wolff's law." Journal of Orthopaedic Research **13**(4): 503-512.
- Mullender, M. G., R. Huiskes and H. Weinans (1994). "A Physiological Approach to the Simulation of Bone Remodeling as a Self-Organizational Control Process." Journal of Biomechanics **27**(11): 1389-1394.
- né Betts, D. C. T., E. Wehrle, G. R. Paul, G. A. Kuhn, P. Christen, S. Hofmann and R. Müller (2020). "The association between mineralised tissue formation and the mechanical local in vivo environment: Time-lapsed quantification of a mouse defect healing model." Scientific Reports **10**(1): 1-10.
- Newman, M. (2010). Networks: an introduction, Oxford university press.
- Nguyen, V. H., T. Lemaire and S. Naili (2010). "Poroelastic behaviour of cortical bone under harmonic axial loading: A finite element study at the osteonal scale." Medical Engineering & Physics **32**(4): 384-390.
- Noble, B. S. and J. Reeve (2000). "Osteocyte function, osteocyte death and bone fracture resistance." Molecular and Cellular Endocrinology **159**(1-2): 7-13.
- Ormsby, R. T., M. Cantley, M. Kogawa, L. B. Solomon, D. R. Haynes, D. M. Findlay and G. J. Atkins (2016). "Evidence that osteocyte perilacunar remodelling contributes to polyethylene wear particle induced osteolysis." Acta Biomaterialia **33**: 242-251.
- Pollack, S. R., N. Petrov, R. Salzstein, G. Brankov and R. Blagoeva (1984). "An Anatomical Model for Streaming Potentials in Osteons." Journal of Biomechanics **17**(8): 627-636.
- Prasad, J. and A. Goyal (2019). "An Invertible Mathematical Model of Cortical Bone's Adaptation to Mechanical Loading." Scientific Reports **9**(1): 5890.
- Price, C., X. Z. Zhou, W. Li and L. Y. Wang (2011). "Real-Time Measurement of Solute Transport Within the Lacunar-Canalicular System of Mechanically Loaded Bone: Direct Evidence for Load-Induced Fluid Flow." Journal of Bone and Mineral Research **26**(2): 277-285.
- Qin, Y. X., W. Lin and C. Rubin (2002). "The pathway of bone fluid flow as defined by in vivo intramedullary pressure and streaming potential measurements." Annals of Biomedical Engineering **30**(5): 693-702.
- Qing, H., L. Ardehripour, P. D. Pajevic, V. Dusevich, K. Jahn, S. Kato, J. Wysolmerski and L. F. Bonewald (2012). "Demonstration of osteocytic perilacunar/canalicular remodeling in mice during lactation." Journal of Bone and Mineral Research **27**(5): 1018-1029.
- Qiu, S., D. Rao, S. Palnitkar and A. Parfitt (2002). "Relationships between osteocyte density and bone formation rate in human cancellous bone." Bone **31**(6): 709-711.
- Raguin, E. and M. A. Streeter (2018). "Brief communication: Test of a method to identify double-zonal osteon in polarized light microscopy." American Journal of Physical Anthropology **167**(2): 407-415.
- Rayfield, E. J. (2019). "What Does Musculoskeletal Mechanics Tell Us About Evolution of Form and Function in Vertebrates?" Feeding in Vertebrates: Evolution, Morphology, Behavior, Biomechanics: 45-70.
- Razi, H., A. I. Birkhold, R. Weinkamer, G. N. Duda, B. M. Willie and S. Checa (2015). "Aging Leads to a Dysregulation in Mechanically Driven Bone Formation and Resorption." Journal of Bone and Mineral Research **30**(10): 1864-1873.
- Razi, H., A. I. Birkhold, P. Zaslansky, R. Weinkamer, G. N. Duda, B. M. Willie and S. Checa (2015). "Skeletal maturity leads to a reduction in the strain magnitudes induced within the bone: A murine tibia study." Acta Biomaterialia **13**: 301-310.

6. References

- Remond, A., S. Naili and T. Lemaire (2008). "Interstitial fluid flow in the osteon with spatial gradients of mechanical properties: a finite element study." Biomechanics and Modeling in Mechanobiology **7**(6): 487-495.
- Repp, F., P. Kollmannsberger, A. Roschger, A. Berzlanovich, G. M. Gruber, P. Roschger, W. Wagermaier and R. Weinkamer (2017). "Coalignment of osteocyte canaliculi and collagen fibers in human osteonal bone." Journal of Structural Biology **199**(3): 177-186.
- Repp, F., P. Kollmannsberger, A. Roschger, M. Kerschnitzki, A. Berzlanovich, G. M. Gruber, P. Roschger, W. Wagermaier and R. Weinkamer (2017). "Spatial heterogeneity in the canalicular density of the osteocyte network in human osteons." Bone Rep **6**: 101-108.
- Robling, A. G., A. B. Castillo and C. H. Turner (2006). "Biomechanical and molecular regulation of bone remodeling." Annual Review of Biomedical Engineering **8**: 455-498.
- Roschger, A., P. Roschger, W. Wagermaier, J. Chen, A. F. van Tol, F. Repp, S. Blouin, A. Berzlanovich, G. M. Gruber, K. Klaushofer, P. Fratzl and R. Weinkamer (2019). "The contribution of the pericanalicular matrix to mineral content in human osteonal bone." Bone **123**: 76-85.
- Rubin, C. T. and L. E. Lanyon (1984). "Dynamic Strain Similarity in Vertebrates - an Alternative to Allometric Limb Bone Scaling." Journal of Theoretical Biology **107**(2): 321-327.
- Ruff, C. B. and W. C. Hayes (1988). "Sex-Differences in Age-Related Remodeling of the Femur and Tibia." Journal of Orthopaedic Research **6**(6): 886-896.
- Ruffoni, D., P. Fratzl, P. Roschger, K. Klaushofer and R. Weinkamer (2007). "The bone mineralization density distribution as a fingerprint of the mineralization process." Bone **40**(5): 1308-1319.
- Sansalone, V., J. Kaiser, S. Naili and T. Lemaire (2013). "Interstitial fluid flow within bone canaliculi and electro-chemo-mechanical features of the canalicular milieu." Biomechanics and Modeling in Mechanobiology **12**(3): 533-553.
- Schult, D. A. and P. Swart (2008). Exploring network structure, dynamics, and function using NetworkX. Proceedings of the 7th Python in Science Conferences (SciPy 2008).
- Shapiro, F. and J. Y. Wu (2019). "Woven Bone Overview: Structural Classification Based on Its Integral Role in Developmental, Repair and Pathological Bone Formation Throughout Vertebrate Groups." European Cells & Materials **38**: 137-167.
- Sims, N. A. and C. Vrahnas (2014). "Regulation of cortical and trabecular bone mass by communication between osteoblasts, osteocytes and osteoclasts." Arch Biochem Biophys **561**: 22-28.
- Skerry, T. (2006). "One mechanostat or many? Modifications of the site-specific response of bone to mechanical loading by nature and nurture." Journal of Musculoskeletal and Neuronal Interactions **6**(2): 122.
- Smalt, R., F. T. Mitchell, R. L. Howard and T. J. Chambers (1997). "Induction of NO and prostaglandin E2 in osteoblasts by wall-shear stress but not mechanical strain." American Journal of Physiology-Endocrinology and Metabolism **273**(4): E751-E758.
- Smit, T. H., E. H. Burger and J. M. Huyghe (2002). "A case for strain-induced fluid flow as a regulator of BMU-coupling and osteonal alignment." Journal of Bone and Mineral Research **17**(11): 2021-2029.
- Smit, T. H., J. M. Huyghe and S. C. Cowin (2002). "Estimation of the poroelastic parameters of cortical bone." Journal of Biomechanics **35**(6): 829-835.
- Srinivasan, S. and T. S. Gross (2000). "Canalicular fluid flow induced by bending of a long bone." Medical Engineering & Physics **22**(2): 127-133.
- Starkebaum, W., S. R. Pollack and E. Korostoff (1979). "Microelectrode studies of stress-generated potentials in four-point bending of bone." J Biomed Mater Res **13**(5): 729-751.
- Steck, R., P. Niederer and M. L. K. Tate (2000). "A finite difference model of load-induced fluid displacements within bone under mechanical loading." Medical Engineering & Physics **22**(2): 117-125.

- Steck, R. and M. L. K. Tate (2005). "In silico stochastic network models that emulate the molecular sieving characteristics of bone." Annals of Biomedical Engineering **33**(1): 87-94.
- Sztefek, P., M. Vanleene, R. Olsson, R. Collinson, A. A. Pitsillides and S. Shefelbine (2010). "Using digital image correlation to determine bone surface strains during loading and after adaptation of the mouse tibia." Journal of Biomechanics **43**(4): 599-605.
- Taddei, F., E. Schileo, B. Helgason, L. Cristofolini and M. Viceconti (2007). "The material mapping strategy influences the accuracy of CT-based finite element models of bones: An evaluation against experimental measurements." Medical Engineering & Physics **29**(9): 973-979.
- Tami, A., P. Nasser, O. Verborgt, M. Schaffler and M. K. Tate (2002). "The role of interstitial fluid flow in the remodeling response to fatigue loading." Journal of Bone and Mineral Research **17**(11): 2030-2037.
- Tate, M. K., P. Niederer and M. Forwood (1997). "In vivo observation of load-induced fluid displacements using procion red and microperoxidase tracers in the rat." Journal of Bone and Mineral Research **12**: F461-F461.
- Tate, M. L. K., P. Niederer and U. Knothe (1998). "In vivo tracer transport through the lacunocanalicular system of rat bone in an environment devoid of mechanical loading." Bone **22**(2): 107-117.
- Tate, M. L. K., R. Steck, A. Tami, H. J. Sidler, E. J. Anderson and P. Niederer (2010). "Computational Modeling of Extravascular Flow in Bone." Computational Modeling in Biomechanics: 307-328.
- Teoh, S. H., B. T. Goh and J. Lim (2019). "Three-Dimensional Printed Polycaprolactone Scaffolds for Bone Regeneration Success and Future Perspective." Tissue Engineering Part A **25**(13-14): 931-935.
- Teti, A. and A. Zallone (2009). "Do osteocytes contribute to bone mineral homeostasis? Osteocytic osteolysis revisited." Bone **44**(1): 11-16.
- Thompson, W. R., S. Modla, B. J. Grindel, K. J. Czymmek, C. B. Kirn-Safran, L. Y. Wang, R. L. Duncan and M. C. Farach-Carson (2011). "Perlecan/Hspg2 Deficiency Alters the Pericellular Space of the Lacunocanalicular System Surrounding Osteocytic Processes in Cortical Bone." Journal of Bone and Mineral Research **26**(3): 618-629.
- Tiede-Lewis, L. M. and S. L. Dallas (2019). "Changes in the osteocyte lacunocanalicular network with aging." Bone **122**: 101-113.
- Tiwari, A. K. and N. Kumar (2018). "Establishing the relationship between loading parameters and bone adaptation." Medical Engineering & Physics **56**: 16-26.
- Tiwari, A. K., R. Kumar, D. Tripathi and S. Badhyal (2018). "In silico modeling of bone adaptation to rest-inserted loading: Strain energy density versus fluid flow as stimulus." Journal of Theoretical Biology **446**: 110-127.
- Tiwari, A. K. and J. Prasad (2017). "Computer modelling of bone's adaptation: the role of normal strain, shear strain and fluid flow." Biomechanics and Modeling in Mechanobiology **16**(2): 395-410.
- Tiwari, A. K. and J. Prasad (2018). "Finding the difference between periosteal and endocortical bone adaptation by using Artificial Neural Networks." bioRxiv: 357871.
- Tomes, J. and C. De Morgan (1853). "Observations on the structure and development of bone." Philosophical Transactions of the Royal Society of London **143**: 109-139.
- Tsay, R. Y. and S. Weinbaum (1991). "Viscous-Flow in a Channel with Periodic Cross-Bridging Fibers - Exact-Solutions and Brinkman Approximation." Journal of Fluid Mechanics **226**: 125-148.
- Vaananen, H. K. (1993). "Mechanism of Bone Turnover." Annals of Medicine **25**(4): 353-359.
- van Tol, A. F., A. Roschger, F. Repp, J. Chen, P. Roschger, A. Berzlanovich, G. M. Gruber, P. Fratzl and R. Weinkamer (2020). "Network architecture strongly influences the fluid flow pattern through the lacunocanalicular network in human osteons." Biomechanics and modeling in mechanobiology **19**(3): 823-840.
- Varga, P., B. Hesse, M. Langer, S. Schrof, N. Mannicke, H. Suhonen, A. Pacureanu, D. Pahr, F. Peyrin and K. Raum (2015). "Synchrotron X-ray phase nano-tomography-based analysis of the lacunar-canalicular

6. References

- network morphology and its relation to the strains experienced by osteocytes in situ as predicted by case-specific finite element analysis." Biomechanics and Modeling in Mechanobiology **14**(2): 267-282.
- Vaughan, T. J., C. A. Mullen, S. W. Verbruggen and L. M. McNamara (2015). "Bone cell mechanosensation of fluid flow stimulation: a fluid-structure interaction model characterising the role integrin attachments and primary cilia." Biomechanics and Modeling in Mechanobiology **14**(4): 703-718.
- Verborgt, O., G. J. Gibson and M. B. Schaffler (2000). "Loss of osteocyte integrity in association with microdamage and bone remodeling after fatigue in vivo." Journal of Bone and Mineral Research **15**(1): 60-67.
- Verbruggen, S. W. (2018). Mechanobiology in Health and Disease, Academic Press.
- Verbruggen, S. W., T. J. Vaughan and L. M. McNamara (2012). "Strain amplification in bone mechanobiology: a computational investigation of the in vivo mechanics of osteocytes." Journal of the Royal Society Interface **9**(75): 2735-2744.
- Verbruggen, S. W., T. J. Vaughan and L. M. McNamara (2014). "Fluid flow in the osteocyte mechanical environment: a fluid-structure interaction approach." Biomechanics and Modeling in Mechanobiology **13**(1): 85-97.
- Wang, B., X. Z. Zhou, C. Price, W. Li, J. Pan and L. Y. Wang (2013). "Quantifying load-induced solute transport and solute-matrix interaction within the osteocyte lacunar-canalicular system." Journal of Bone and Mineral Research **28**(5): 1075-1086.
- Wang, L. Y. (2018). "Solute Transport in the Bone Lacunar-Canalicular System (LCS)." Current Osteoporosis Reports **16**(1): 32-41.
- Wang, L. Y., C. Ciani, S. B. Doty and S. P. Fritton (2004). "Delineating bone's interstitial fluid pathway in vivo." Bone **34**(3): 499-509.
- Wang, L. Y., S. C. Cowin, S. Weinbaum and S. P. Fritton (2000). "Modeling tracer transport in an Osteon under cyclic loading." Annals of Biomedical Engineering **28**(10): 1200-1209.
- Wang, L. Y., S. P. Fritton, S. C. Cowin and S. Weinbaum (1999). "Fluid pressure relaxation depends upon osteonal microstructure: modeling an oscillatory bending experiment." Journal of Biomechanics **32**(7): 663-672.
- Wang, L. Y., Y. L. Wang, Y. F. Han, S. C. Henderson, R. J. Majeska, S. Weinbaum and M. B. Schaffler (2005). "In situ measurement of solute transport in the bone lacunar-canalicular system." Proceedings of the National Academy of Sciences of the United States of America **102**(33): 11911-11916.
- Wang, Y. L., L. M. McNamara, M. B. Schaffler and S. Weinbaum (2007). "A model for the role of integrins in flow induced mechanotransduction in osteocytes." Proceedings of the National Academy of Sciences of the United States of America **104**(40): 15941-15946.
- Weinbaum, S., S. C. Cowin and Y. Zeng (1994). "A Model for the Excitation of Osteocytes by Mechanical Loading-Induced Bone Fluid Shear Stresses." Journal of Biomechanics **27**(3): 339-360.
- Weinkamer, R., C. Eberl and P. Fratzl (2019). "Mechanoregulation of Bone Remodeling and Healing as Inspiration for Self-Repair in Materials." Biomimetics **4**(3).
- Weinkamer, R., P. Kollmannsberger and P. Fratzl (2019). "Towards a Connectomic Description of the Osteocyte Lacunocanalicular Network in Bone." Curr Osteoporosis Rep **17**(4): 186-194.
- Wijeratne, S. S., J. R. Martinez, B. J. Grindel, E. W. Frey, J. Q. Li, L. Y. Wang, M. C. Farach-Carson and C. H. Kiang (2016). "Single molecule force measurements of perlecan/HSPG2: A key component of the osteocyte pericellular matrix." Matrix Biology **50**: 27-38.
- Willie, B., G. N. Duda and R. Weinkamer (2013). Bone Structural Adaptation and Wolff's Law, RCS Publishing.
- Willie, B. M., A. I. Birkhold, H. Razi, T. Thiele, M. Aido, B. Kruck, A. Schill, S. Checa, R. P. Main and G. N. Duda (2013). "Diminished response to in vivo mechanical loading in trabecular and not cortical bone in

- adulthood of female C57Bl/6 mice coincides with a reduction in deformation to load." Bone **55**(2): 335-346.
- Wilson, T. (2011). "Resolution and optical sectioning in the confocal microscope." Journal of microscopy **244**(2): 113-121.
- Winkler, D. G., M. K. Sutherland, J. C. Geoghegan, C. Yu, T. Hayes, J. E. Skonier, D. Shpektor, M. Jonas, B. R. Kovacevich, K. Staehling-Hampton, M. Appleby, M. E. Brunkow and J. A. Latham (2003). "Osteocyte control of bone formation via sclerostin, a novel BMP antagonist." EMBO J **22**(23): 6267-6276.
- Wittig, N. K., M. Laugesen, M. E. Birkebæk, F. L. Bach-Gansmo, A. Pacureanu, S. Bruns, M. H. Wendelboe, A. Brüel, H. O. Sørensen and J. S. Thomsen (2019). "Canalicular Junctions in the Osteocyte Lacuno-Canalicular Network of Cortical Bone." ACS nano.
- Wu, X. G. and W. Y. Chen (2013). "A hollow osteon model for examining its poroelastic behaviors: Mathematically modeling an osteon with different boundary cases." European Journal of Mechanics a-Solids **40**: 34-49.
- Wu, X. G., N. N. Wang, Z. W. Wang, W. L. Yu, Y. Q. Wang, Y. Guo and W. Y. Chen (2016). "Mathematically modeling fluid flow and fluid shear stress in the canaliculi of a loaded osteon." Biomedical Engineering Online **15**.
- Wu, X. G., Y. Q. Wang, X. H. Wu, H. P. Cen, Y. Guo and W. Y. Chen (2014). "Effects of microcracks on the poroelastic behaviors of a single osteon." Science China-Physics Mechanics & Astronomy **57**(11): 2161-2167.
- Xie, Y., L. Zhang, Q. Xiong, Y. Gao, W. Ge and P. Tang (2019). "Bench-to bedside strategies for osteoporotic fracture: From osteoimmunology to mechanosensation." Bone research **7**(1): 1-13.
- Yoon, Y. J. and S. C. Cowin (2008). "An estimate of anisotropic poroelastic constants of an osteon." Biomechanics and Modeling in Mechanobiology **7**(1): 13-26.
- Yoshino, M., K. Imaizumi, S. Miyasaka and S. Seta (1994). "Histological Estimation of Age at Death Using Microradiographs of Humeral Compact-Bone." Forensic Science International **64**(2-3): 191-198.
- You, L. D., S. C. Cowin, M. B. Schaffler and S. Weinbaum (2001). "A model for strain amplification in the actin cytoskeleton of osteocytes due to fluid drag on pericellular matrix." Journal of Biomechanics **34**(11): 1375-1386.
- You, L. D., S. Weinbaum, S. C. Cowin and M. B. Schaffler (2004). "Ultrastructure of the osteocyte process and its pericellular matrix." Anatomical Record Part a-Discoveries in Molecular Cellular and Evolutionary Biology **278a**(2): 505-513.
- Yu, W., X. Wu, H. Cen, Y. Guo, C. Li, Y. Wang, Y. Qin and W. Chen (2019). "Study on the biomechanical responses of the loaded bone in macroscale and mesoscale by multiscale poroelastic FE analysis." BioMedical Engineering OnLine **18**(1): 122.
- Zeng, Y., S. C. Cowin and S. Weinbaum (1994). "A Fiber-Matrix Model for Fluid-Flow and Streaming Potentials in the Canaliculi of an Osteon." Annals of Biomedical Engineering **22**(3): 280-292.
- Zhang, D., S. Weinbaum and S. C. Cowin (1998). "Estimates of the peak pressures in bone pore water." Journal of Biomechanical Engineering-Transactions of the Asme **120**(6): 697-703.
- Zhang, D. J., S. Weinbaum and S. C. Cowin (1998). "On the calculation of bone pore water pressure due to mechanical loading." International Journal of Solids and Structures **35**(34-35): 4981-4997.
- Zhou, X. Z., J. E. Novotny and L. Y. Wang (2008). "Modeling Fluorescence Recovery After Photobleaching in Loaded Bone: Potential Applications in Measuring Fluid and Solute Transport in the Osteocytic Lacunar-Canalicular System." Annals of Biomedical Engineering **36**(12): 1961-1977.
- Zhou, X. Z., J. E. Novotny and L. Y. Wang (2009). "Anatomic variations of the lacunar-canalicular system influence solute transport in bone." Bone **45**(4): 704-710.

6. References

Ziouti, F., A. P. Soares, I. Moreno-Jiménez, A. Rack, B. Bogen, A. Cipitria, P. Zaslansky and F. Jundt (2020). "An Early Myeloma Bone Disease Model in Skeletally Mature Mice as a Platform for Biomaterial Characterization of the Extracellular Matrix." Journal of Oncology **2020**.

7. DEDICATION

I would like to dedicate this thesis to my wife, Ruiting Zhao, who continuously supported and encouraged me like no other during my whole PhD study.

8. ACKNOWLEDGEMENTS

Firstly I would like to thank my supervisor, Prof. Peter Fratzl, director of the Biomaterials department, for the given opportunity to be part of his department. The nice atmosphere in his department helped me to collaborate with great people, which definitely contributed to the work.

I would like to thank Dr. Richard Weinkamer, my group leader at the Biomaterials department of the Max Planck Institute of Colloids and Interfaces in Golm. I am thankful for his support during the whole study. I benefitted from his interesting views during the discussions and from the freedom he gave me during the PhD project.

I also thank my colleagues Dr. Andreas Roschger, Victoria Schemenz and Dr. Junning Chen and group leader Dr. Wolfgang Wagermaier. When I had a question, wanted a discussion, or needed something else they were there for me without any hesitation.

The technical support from different groups in his department and the nice discussions with people from different disciplines were very informative. Not less important was the social activities with many members of the department. Therefore I also want to acknowledge everyone from the Biomaterials department. I particularly thank Birgit Schonert, Gabriele Wiensköl, Friedrich Reppe and Dr. Michaela Eder for technical assistance in carrying out my sample preparation. Without them I could not have reached the sample quality, which was important for my study.

I would like to thank Bettina Willie PhD, Associate Professor at the department of Pediatric Surgery, Faculty of Medicine, McGill University and Shriners Hospital for Children in Montreal, Canada. We had a very nice collaboration with her, and her students Isabela Vitienes and Dr. Maximilian Rummeler. Moreover, she provided us with the mouse tibia, which were very valuable for my PhD project.

I also thank Petra Keplinger, Sonja Lueger, Phaedra Messmer and Daniela Gabriel from the Ludwig Boltzmann Institute of Osteology, Vienna, Austria for providing us with the human bone samples. I also want to thank Dr. Paul Roschger and his team from the Ludwig Boltzmann Institute, for giving me access to their lab and the discussions.

I want to thank the Berlin-Brandenburg School for Regenerative Therapies (BSRT) and in particular Dr. Sabine Bartosch. Especially the soft-skill courses provided by the BSRT helped me to develop as a PhD student.

The research presented in my PhD thesis was supported by a grant from the German Research Foundation (DFG, Grant no. WE 4341/1-1), the Research Funds of the AUVA (Austrian Workers Compensation Board, Austria) and the WGKK (Viennese Sickness Insurance Funds, Austria).

9. SELBSTSTÄNDIGKEITSERKLÄRUNG

Hiermit versichere ich, dass ich meine Dissertation mit dem Titel “Function of the Osteocyte Lacunocanalicular Network in Bone Mechanoresponsiveness” selbstständig angefertigt und keine anderen, als die von mir angegebenen Hilfsmittel und Quellen verwendet habe. Ich versichere, dass ich bisher an keiner Universität, weder im In- noch im Ausland, einen Promotionsversuch unternommen habe.

Die Promotionsordnung der Mathematisch-Naturwissenschaftlichen Fakultät, veröffentlicht im Amtlichen Mitteilungsblatt der Humboldt-Universität zu Berlin Nr. 42 am 11. Juli 2018, habe ich zur Kenntnis genommen.

Potsdam, July 2020

Alexander Franciscus van Tol